UNIVERSITÀ DI PARMA

UNIVERSITÀ DEGLI STUDI DI PARMA

DOTTORATO DI RICERCA IN
"TECNOLOGIE DELL'INFORMAZIONE"

CICLO XXXIII

Multi-Carrier Modulations Over Sparse Channels: Communication, Channel Estimation, and Radar Sensing

Coordinatore:
Chiar.mo Prof. Marco Locatelli

Tutore:
Chiar.mo Prof. Giulio Colavolpe
Chiar.mo Prof. Giuseppe Caire

Dottorando: Lorenzo Gaudio

Anni 2017/2020

a chi crede in me

Contents

List of Figures

List of acronyms

OTFS	orthogonal time frequency space
ISFFT	inverse symplectic finite Fourier transform
SFFT	symplectic finite Fourier transform
ICI	inter carrier interference
ISI	inter symbol interference
CRLB	Crameŕ-Rao lower bound
CP	cyclic prefix
MSE	mean square error
ML	maximum likelihood
SNR	signal-to-noise ratio
MP	message passing
OFDM	orthogonal frequency-division multiplexing
RMSE	root mean square error
CSI	channel state information
LLR	log-likelihood ratio
BPSK	binary phase shift keying
UB	upper bound
AWGN	additive white Gaussian noise
CAF	cross-ambiguity function
Tx	transmitter
Rx	receiver
LoS	line of sight

CIR	channel impulse response
RMSE	root MSE
FG	factor graph
LMMSE	linear minimum mean square error
SPA	sum-product algorithm
i.i.d.	independent and identically distributed
pdf	probability density function
LDPC	low-density parity check
SINR	signal-to-interference noise ratio
QAM	quadrature amplitude modulation
GI	guard interval
LASSO	least-absolute shrinkage and selection operator
RSS	residual sum of squares
PC	pragmatic capacity
CS	compressed sensing
IBI	inter-block interference
QPSK	quadrature phase-shift keying
MIMO	multiple-input multiple-output
DFT	discrete Fourier transform
IDFT	inverse discrete Fourier transform
IFFT	inverse fast Fourier transform
DSP	digital signal processing
FMCW	frequency modulated continuous wave
FFT	fast Fourier transform
BER	bit error rate
MMSE	minimum mean square error
mmWave	millimeter wave
V2X	vehicle-to-everything
HPBW	half-power beamwidth
ULA	uniform linear array
RF	radio frequency

BF	beamforming
AoA	angle of arrival
TDD	time division duplex
SIC	successive interference cancellation
PD	probability of detection
HDA	hybrid digital-analog
PSD	power spectral density
w.r.t.	with respect to

Introduction

Every year, in every field, the research introduces many novelties to contribute to the improvement of the state-of-the-art technologies. Under this context, the upgrade in terms of hardware capabilities and functionalities necessitates a constantly updated definition of the software, to be able to exploit all the possibilities owned by each single equipment. By mostly focusing on communication, i.e., the capability to send useful information from a source to a destination, the research looks forward to the definition of new communication standards, to break the limits imposed by outdated mechanisms and rules. Under this context, the upcoming technology for wireless and digital communications is the 5G standard, which brings improvements in both hardware equipment and software definition. Differently from its predecessor, i.e., the LTE (4G) standard, many new use cases and scenarios will be introduced. For instance, the improvements move towards the maximization of the data rate, to support the growing and massive amount of traffic data (especially from mobile users), the minimization of the latency, to enable new delay-intolerant services, and to optimize the energy consumption of any device, together with its cost.

From a more technical point of view and of relevant interest for this dissertation, new vehicular communication (V2V, V2X) scenarios are going to be studied, by mostly focusing on millimeter wave frequency bands, strictly linked to the definition of massive MIMO antenna systems exploiting huge antenna gains through beamforming, necessary to contrast the high propagation loss typical of that frequencies. Under this context, against common and well known radar systems, able to efficiently detect and locate a target within the range-velocity plane, new joint radar and communications techniques are taking part of the current literature. These system are mainly focused on the transmission of useful information towards the targets, which are, thus, not only "passively" detected, and a single equipment is able to perform both operational modes, avoiding to split the functionalities between two distinct subsystems (with increased cost and complexity). Hence, there are mainly two approaches to solve the aforementioned problem. The first one considers the application of common radar waveforms, adapted to carry useful information with them. The second one, which is the one explored in this dissertation, takes into account typical communication waveforms (single- or multi-carrier), and, while communication tasks come naturally, the radar processing is performed with novel methods exploiting the knowledge of the transmitted information (known by both transmitter and receiver, if physically colocated), thus differs from a more direct, or "radar-like", threshold analysis of the backscattered power from the target. The choice of the communication waveform is subject to a non trivial tradeoff. On one hand, the system aims the maximization of the communication achievable rate, i.e., the amount of information sent in a time-frequency window. On the other hand, radar tasks have to be performed with as much precision as possible, in order to correctly localize a target in all dimensions, i.e., range, velocity, and space (angular) location. Typically, pure radar tasks are performed with chirp-like pulses, i.e., short single-carrier impulses with large bandwidth, such that the total energy delivered towards the targets is compensated by the band occupation of the signal. Thus, the joint definition of a short pulse, together with large bandwidth, leads to a very precise localization of the target over the three aforementioned domains. However, the amount of (possible) useful information, impressed on top of such chirp, is poor. A solution to improve the communication rate is the use of multi-carrier digital waveforms, modulating information symbols not only in time domain (as single-carrier) but also in the frequency band, split in many subcarriers each occupied by a different modulation symbol. However, limitations are linked to the definition of the symbol time and the subcarrier spacing, which are in a one-to-one relation, and a good localization is not only challenging, for instance, in terms of signal processing algorithms, but also definitely sub-optimal with respect to single-carrier solutions, but this is the cost to pay in order to bring communication features together with radar tasks. In conclusion, the current literature is moving towards the definition of new multi-carrier schemes able to break the limits, in terms on communication rate, imposed by classical radar waveforms, and the optimization of the tradeoff between the two different tasks is an open problem, whose optimal solutions have not been defined yet.

The choice of the multi-carrier modulation for joint radar and communication falls into two distinct waveforms, i.e., orthogonal frequency-division multiplexing (OFDM) modulation and orthogonal time frequency space (OTFS) modulation. OFDM is the most popular multi-carrier modulation of recent years, widely studied and standardized in most of the current communication standards, including 5G. The motivation of this choice is simple: thanks to the application of a cyclic prefix between symbols, i.e., a guard interval to prevent inter-symbol interference, and under the assumption of absence of inter-carrier interference, which holds under reasonable amount of the Doppler effect and subcarrier spacing, the communication channel can be diagonalized and symbol-by-symbol detection performed. Clearly, the appealing simplicity of detection makes OFDM the best choice for modern digital communications. On the other hand, OTFS is a modulation waveform with two big differences with respect to its direct competitor. First, it does not necessitate the insertion of the cyclic prefix, achieving a better communications rate, i.e., more information is sent over a time-frequency window, but at the cost of a more complex detection approach, working blockwise and not symbol-by-symbol. Second, OTFS is not sensitive to delay and Doppler shifts, meaning that its performance is kept constant whatever the distance and the speed between transmitter and (target) receiver. This feature is very appealing for joint radar and communication tasks, being the scenario very dynamical, with possible remarkable Doppler shifts and delays, increased by considering the round-trip time between radar transmitter and target. Based on the aforementioned analysis, in this dissertation we take care of a fair comparison between the two digital modulation formats, from the point of view of radar, parameter estimation, achievable communication rate, channel estimation, and more other tasks, to determine their positive and negative aspects, such that a system designer is able to choose the most suitable waveform for a given scenario or application.

State of the Art

By extending the introduction, some details are provided here, with the corresponding references to literature, but some other are left to the introductions of chapters.

The 5G communication standard will bring some novelties to overcome outdated and old techniques [1]. By mostly focusing on multi-carrier modulation formats, in particular OFDM [2, 3] and OTFS [4, 5, 6], this dissertation provides a complete analysis and performance comparison under different scenarios, with the common denominator of the sparse description of the communication channel [7], whose characteristics depend on the surrounding environment. Under this context, typical channels are characterized by few reflectors with their relative line-of-sight and small number of additional multi-path components (ground reflection and some other reflections from, e.g., metal surfaces) [8, 9]. Motivated by emerging vehicular applications (V2X) [10], joint radar and communication systems have been studied, in such a configuration the two functions share the same physical resources [11, 12]. Thus, differently from pure radar tasks, which aim to detect targets with high resolution [12, 13], also an active communication, i.e., the transmission of useful data, is considered, such that both functionalities might work together to jointly improve the performance. Note that this differs from typical beacon-based initial acquisition of communication standards [14, 15, 16, 17, 18], where the alignment between transmitter and receiver is achieved through a sort of handshake, i.e., the two entities talk together to achieve the common task. Given the appealing of joint radar and communication systems for future vehicle-to-everything (V2X) communications, the recent literature provides many different and detailed solutions [19, 20, 21, 11, 22, 23, 24, 25, 26], basically divided into two classes: information-embedded radar waveforms [11, 27, 24] and communication waveforms applied to radar detection and parameter estimation [11, 19, 21, 26, 28, 29]. Moreover, note that the jointly approach could break the limits imposed by separated, or resource sharing, methods [30]. This dissertation, as said before, studies the case of communication waveforms applied to radar, by reviewing some well-known signal processing for OFDM (see [26, 21] and references therein), while exploiting new methods for OTFS, whose baselines are shared by other works in the literature, but in different shapes (see, e.g., [28, 29, 15]). In order to demonstrate that the joint approach is superior (not always but given some system setups) with respect to the physical resources split to one or the other task, the comparison will also take into account typical radar waveforms [13, 20].

When a communication waveform is employed, the problems of radar detection and parameter estimation are based on the knowledge of the information transmitted and backscattered from a target, which results to be known if radar transmitter and receiver are colocated. Note that this is also possible thanks to full-duplex configurations [31, 32, 33], which limits the self-interference of the system, which results, on the other hand, unable to properly work if this condition is not fulfilled. Thus, information symbols are treated as known in the conditioning of probability density functions during digital signal processing operations, as, e.g., in [15], rather than unknown as in typical detection problems [34]. Hence, the joint radar sensing and communication paradigm results similar to classical channel estimation schemes, because the final goal is equivalent, i.e., the characterization of the surrounding channel. Being the channel state information, i.e., the knowledge of the communication channel, required to perform coherent detection in any scenario, the literature treating its estimation is wide [34]. Generally, this information is accessed through symbols, i.e., pilots, known at both transmitter and receiver

[35, 36, 37]. It is straightforward to understand that, by taking into account a full block of symbols backscattered from a target, in a joint radar and communication scheme, all symbols take the role of pilots. Many techniques to solve the channel estimation problem are present in literature. By taking into account the sparse channel representation in the Doppler-delay domain (see, e.g., [7, 5]), for OFDM, these techniques might use concepts from compressed sensing literature, e.g., [38, 39, 40, 41, 42, 35, 43], while OTFS propose a variety of solutions, based on minimum-mean square error estimation, maximum likelihood, compressed sensing, and others [37, 44, 45, 46, 47, 48].

At last, by taking into account the additional spatial dimension, multi antenna systems are studied. The choice of considering multiple-input multiple-output (MIMO) configurations for radar is fundamental [49]. In fact, other than opening to angle of arrival (or, equivalently, space) estimation of the target, it allows, through a careful design of the beam pattern [50], to separately track different objects or targets [51, 52], while improving the power delivered towards a direction, thanks to the additional antenna gain, which is very relevant in V2X radars [20] and opens to transmission over millimeter wave frequency bands [50]. By considering the problem of radar detection, a non trivial tradeoff appears with respect to the angular coverage of the beam pattern. On one hand, a wider angular sector coverage enables to detect potentially more targets simultaneously, if the received backscattered power is high enough. On the other hand, a more directional allocation of the power towards a narrower angular sector, grants a higher received signal-to-noise ratio, at the cost of a time-consuming search (as classical radar successively swapping adjacent regions, see, e.g.,[13]). Different solutions can be found in the literature (see, e.g., [52, 53, 15, 54]). Moreover, this dissertation will treat the problem of mismatch between the number of antennas and the number of radio frequency chains. In fact, by considering MIMO configurations over millimeter wave frequency bands, it is difficult to implement a fully digital beamforming, or, equivalently, to associate one radio frequency chain per antenna (including A/D conversion, modulation, and amplification) in a small form factor and highly integrated technology over a large signal bandwidth. Therefore, for millimeter wave automotive applications, we study hybrid digital-analog beamforming schemes (see, e.g., [55, 56] and references therein), thus, without relying on optimal full-duplex configurations as generally done in literature [49, 52, 54].

More details about the state-of-the-art will be given within the following chapters.

Chapter 1

Multi Carrier Modulations

1.1 The Communication Channel

The communication channel describes how the transmitted signal is modified when traveling through the communication medium (e.g., an optical fiber, the air, a copper line, etc.). Different impairments and effects characterize each different scenario, and the associated channel is completely described by its channel impulse response (CIR). These effects, including, for instance, fading fluctuations, shadowing, delay, frequency shifts, phase noise, etc., are described by mathematical models, exploited during the algorithmic design of detectors, estimators, and any other digital signal processing (DSP) which could be performed by the communication receiver (Rx).

The channel considered in this dissertation is time-frequency varying, i.e., its behavior changes with respect to (w.r.t.) the time instant and the carrier (or subcarrier) frequency considered. In order to simplify its treatment, the channel can be represented in distinct domains, each owning its different (but behaviorally equivalent) description function. In fact, clearly, the channel behavior must remain the same while its representation changes. In order to switch between different domains, a direct or inverse Fourier transform (i.e., $\mathcal{F}$ or $\mathcal{F}^{-1}$, respectively) has to be applied [7]. Fig. 1.1 shows all the domains and

$$\begin{tikzcd}
\gamma(t,\tau) \arrow[r, shift left, "\mathcal{F}"] \arrow[d, shift right, "\mathcal{F}"'] & H(t,f) \arrow[l, shift left, "\mathcal{F}^{-1}"] \arrow[d, shift left, "\mathcal{F}"] \\
h(\nu,\tau) \arrow[u, shift right, "\mathcal{F}^{-1}"'] \arrow[r, shift left, "\mathcal{F}^{-1}"] & \Gamma(\nu,f) \arrow[l, shift left, "\mathcal{F}"] \arrow[u, shift left, "\mathcal{F}^{-1}"]
\end{tikzcd}$$

Figure 1.1: Channel domains.

the relative Fourier transforms. In the top right position of Fig. 1.1 we find the time-frequency domain, with function $H(t,f)$. Considering only direct Fourier transforms, i.e., $\mathcal{F}$, we first move to the Doppler-frequency domain ($\Gamma(\nu,f)$), then to the Doppler-delay domain ($h(\nu,\tau)$), and finally to the time-delay domain ($\gamma(t,\tau)$).

It is interesting to note that the channel description in the Doppler-delay domain relies in its physical representation, or geometry, which simplifies the overall mathematical analysis [4, 5, 7]. In fact, typically, only a small number of reflectors (or propagation paths) takes part of a channel, which is thus sparse and can be modeled with few parameters. Moreover, the geometry of the surrounding environment slowly changes in time (w.r.t. the frame duration), behavior which could be exploited during the algorithmic design. The sparse representation of the channel $h(\nu,\tau)$ can be given as [7]

$$h(\nu,\tau) = \sum_{p=0}^{P-1} h_p \delta(\tau - \tau_p)\, \delta(\nu - \nu_p) \ , \tag{1.1}$$

where P is the number of propagation paths, h_p, τ_p, and ν_p represent the path gain, delay, and Doppler shift associated to the p-th path. The key point is that the channel behavior is discrete in the number of paths. In other words, a single symbol transmitted over the channel is shifted in the delay domain, i.e., is received with a delay of τ_p, and its frequency is shifted of ν_p (Doppler effect).

An extension of the (1.1) taking into account MIMO antenna systems can be found in Chapter 3 and in [7].

1.2 Orthogonal Frequency Division Multiplexing (OFDM) Modulation

Before entering into the details of OFDM signal processing, for radar and communication purposes, we will briefly describe the basics of this modulation technique, to better understand things to come. This pretends to be an overview of mainly aspects which are relevant for our analysis, while a more in-depth description can be found in many different digital communication books (see, e.g., [2, 3]) and works in literature [2, 57, 58].

As the name suggests, OFDM is a multiplexing scheme which modulates data (information symbols) on distinct parallel orthogonal frequencies (see also the pioneering work [58]). In general, OFDM uses a certain number of subcarriers, to equally split the available bandwidth, and some time slots, which, together, identify an OFDM frame. The dimension of such frame depends on the particular application, which could aim at low-latency systems, i.e., smaller frames in time, or necessitates larger dimensions to cope and estimate unknown channel impairments. As a notation, a set of modulation symbols transmitted over different subcarriers at the same time is called OFDM symbol, while more OFDM symbols (in time) form the OFDM frame.

The orthogonality of the frequency division is achieved by choosing a constant subcarrier spacing Δf, generally defined as the inverse of the symbol duration T, i.e., $\Delta f = 1/T$, in order to avoid data loss during filtering operations. Thus, by assuming a rectangular shaping pulse of duration T to modulate constellation symbols at the transmitter (Tx) side, whose expression is given by

$$\mathrm{rect}(t) = \begin{cases} 1 & \text{if } \; |t| \leq T/2 \\ 0 & \text{otherwise} \end{cases} , \tag{1.2}$$

the transmitted pulse, when a generic modulation symbol $x_{n,m}$ is sent, with n and m the time and frequency indexes, respectively, results to be

$$s_{n,m}(t) = \mathrm{rect}(t - nT_o)e^{j2\pi m \Delta f t} x_{n,m} \,, \tag{1.3}$$

where $T_o = T + T_{\mathrm{cp}}$ is the OFDM symbol duration, including the presence of a cyclic prefix (CP), necessary to avoid inter-symbol interference (ISI) as explained afterwords. The orthogonality condition, which remarkably simplifies the OFDM input-output relation, as we will see next, hold both in time, thanks to the insertion of the CP, and in frequency, through the Fourier transform of the rectangular pulse, which is a sinc function with peaks and zeros jointly located (absence of interference). The orthogonality condition, in both domains, can be written as

$$\int_{-\infty}^{\infty} s_{n,m}(t)s^*_{n',m'}(t)dt = \begin{cases} \text{constant} & \text{if } n = n', m = m' \\ 0 & \text{otherwise} \end{cases} . \tag{1.4}$$

Proof. To prove the result for time, assume that $n \neq n'$. Thus, the product $\mathrm{rect}(t - nT_o)\mathrm{rect}(t - n'T_o)$ is always zero, and this simply prove what stated in (1.4). Next, assume $n = n'$ but $m \neq m'$ and solve (1.4), i.e.,

$$\begin{aligned} \int_{-\infty}^{\infty} s_{n,m}(t)s^*_{n',m'}(t)dt &= \int_0^T e^{j2\pi(m-m')\Delta f t} dt \\ &= \frac{1}{2\pi(m - m')\Delta f} \left[e^{j2\pi(m-m')\Delta f t} \right]_0^T \\ &= 0 \,, \end{aligned} \tag{1.5}$$

where the last equality hold since $\Delta f T = 1$. Thus, only for $n = n'$ and $m = m'$, the previous equation becomes

$$\int_0^T e^{j2\pi(m-m')\Delta f t} dt = \int_0^T 1 dt = T \,. \tag{1.6}$$

■

Another key aspect of OFDM modulation is the insertion of a CP, necessary to avoid ISI between OFDM symbols. The CP duration depends on the maximum delay introduced by the channel, and has to be defined *ad hoc* for any particular scenario. Typically, it is chosen to be an integer fraction of the symbol duration, and some common values are, for instance, $T_{\text{cp}} = T/4$ or $T_{\text{cp}} = T/8$. As anticipated before, this increases the total OFDM symbol duration to $T_o = T + T_{\text{cp}}$. However, without this guard interval, any time-dispersive channel (time-frequency varying) would leak energy from one OFDM symbol into the adjacent one(s), causing significant ISI. Thus, the CP prevents the loss of orthogonality between symbols, allowing to perform symbol-by-symbol detection, relying on the diagonal representation of the channel [2, 3]. Generally, the CP results to be a copy of the last T_{cp}/T part of every OFDM symbol (see [2, 3] for more details).

The last two parameters of interest are the sampling rate and the inverse fast Fourier transform (IFFT) length, specifying the bandwidth of the OFDM signal. As a well-known approach, the modulation of an OFDM signal can be efficiently performed by computing an IFFT. For instance, consider the discrete-time representation of the sum of modulation symbols $\{x_{n,m}\}$ for any OFDM symbol at time n and subcarrier m, sampled at time intervals T_s (the sampling time)

$$s(kT_s) = \sum_{n=0}^{N-1} x_{n,m} \text{rect}\left(kT_s\right) e^{j2\pi n\Delta f kT_s} = \sum_{n=0}^{N-1} x_{n,m} e^{j2\pi n\Delta f kT_s} . \tag{1.7}$$

Thus, by setting $T_s = T/N = 1/(\Delta f N)$, we get

$$s(nT_s) = \sum_{k=0}^{N-1} x_{k,i} e^{j2\pi\frac{nk}{N}} , \tag{1.8}$$

which clearly shows that the discrete-time signal for any OFDM symbol is given by the IFFT of the modulation symbols at a sampling rate $f_s = 1/T_s = N\Delta f$.

These are the fundamental ingredients of OFDM modulation, which help understanding the following treatment.

1.2.1 Input Output Relation

Based on the previous discussion, consider a standard OFDM modulation with CP, necessary, as said before, to avoid ISI to admit symbol-by-symbol detection. The resulting OFDM symbol duration is $T_o = T_{\text{cp}} + T$, where T_{cp} and T denote the duration of CP and data symbols, respectively. Provided the maximum delay introduced by the communication channel is τ_{max}, we typically choose $T_{\text{cp}} = \lceil \frac{\tau_{\text{max}}}{T/M} \rceil \cdot \frac{T}{M}$, where $\lceil \cdot \rceil$ is the rounding-up operation, selecting the smallest integer greater than or equal to the function argument. The OFDM frame duration is thus $T_f^{\text{ofdm}} = NT_o$.

Based on the aforementioned analysis (see (1.8)), the continuous-time OFDM transmitted signal with CP is given by

$$s(t) = \sum_{n=0}^{N-1} \sum_{m=0}^{M-1} x_{n,m} \text{rect}(t - nT_o) e^{j2\pi m \Delta f (t - T_{\text{cp}} - nT_o)} \, , \tag{1.9}$$

where $\text{rect}(t)$ is defined in (1.2) and $\{x_{n,m}\}$ are symbols belonging to any constellation format. By ignoring the noise for the sake of simplicity, the signal received after the time-frequency selective channel (1.1) (or any equivalent representation in another domain) is

$$y'(t) = \int \gamma(t, \tau) s(t - \tau) d\tau = \sum_{p=0}^{P-1} h_p s(t - \tau_p) e^{j2\pi \nu_p t} \, . \tag{1.10}$$

By sampling $y'(t)$ every T/M seconds and discarding the CP samples in each OFDM symbol (such that the ISI is completely removed), we obtain

$$\begin{aligned} y'_{n,m} &= y'(t)|_{t = nT_o + T_{\text{cp}} + mT/M} \\ &= \sum_{p=0}^{P-1} h_p e^{j2\pi n T_o \nu_p} \sum_{m'=0}^{M-1} x_{n,m'} e^{j2\pi \frac{m}{M} \left(\frac{\nu_p}{\Delta f} + m' \right)} e^{-j2\pi m' \Delta f \tau_p} \, . \end{aligned} \tag{1.11}$$

As said, the CP duration has to be chosen accordly to the maximum delay introduced by the channel, i.e., $T_{\text{cp}} \geq \tau_{\text{max}}$. Applying the discrete Fourier transform (DFT) and using the orthogonal property, the output is given by

$$\begin{aligned}
y_{n,m} &= \frac{1}{M}\sum_{i=0}^{M-1} y'_{n,i} e^{-j2\pi\frac{mi}{M}} \\
&= \frac{1}{M}\sum_{p=0}^{P-1} h_p e^{j2\pi\nu_p n T_o} \sum_{m'=0}^{M-1} x_{n,m'} e^{-j2\pi m'\Delta f \tau_p} \sum_{i=0}^{M-1} e^{j2\pi\frac{i}{M}\frac{\nu_p}{\Delta f}} e^{j2\pi\frac{i(m'-m)}{M}} \\
&\approx \frac{1}{M}\sum_{p=0}^{P-1} h_p e^{j2\pi n T_o \nu_p} \sum_{m'=0}^{M-1} x_{n,m'} e^{-j2\pi m'\Delta f \tau_p} \sum_{i=0}^{M-1} e^{j2\pi\frac{i(m'-m)}{M}} \\
&\approx \sum_{p=0}^{P-1} h_p e^{j2\pi n T_o \nu_p} e^{-j2\pi m \Delta f \tau_p} x_{n,m} \, , \qquad (1.12)
\end{aligned}$$

where the first approximation follows by letting $\nu_{\max} \ll \Delta f$ and the last step exploits the orthogonality condition.[1] Under the approximated channel input-output relation (1.12), it readily follows that the Doppler shift and the delay are decoupled, which makes simple any possible DSP operation (see, e.g., [26, 19]). Moreover, note that each received sample depends only on the corresponding transmitted symbols, and (1.12) confirms the possibility of performing symbol-by-symbol detection. Thus, at the cost of a CP insertion, whose length and the consequent loss in data rate could be remarkable, and with some limitations on the maximum supportable Doppler shift, OFDM results to be treatable with easy handling.

---

[1] Note that this approximation can be justified in a number of scenarios. For example, consider a scenario inspired by IEEE 802.11p with $f_c = 5.89$ GHz and the subcarrier spacing $\Delta f = 156.25$ KHz. This yields $v_{\max} \ll 14325$ [km/h], which is reasonable even for a relative speed of 400 [km/h]. The same holds for IEEE 802.11ad with $f_c = 60$ GHz and $\Delta f = 5.15625$ MHz [59].

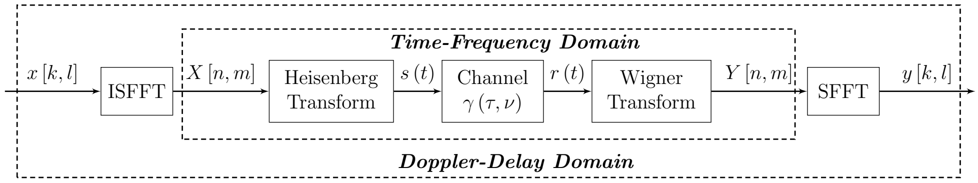

Figure 1.2: OTFS system model

1.3 Orthogonal Time Frequency Space (OTFS) Modulation

The recently proposed OTFS modulation pretends to be a candidate alternative to OFDM [4, 5]. The basic idea behind this new waveform is to exploit the sparse properties of the channel described in the Doppler-delay domain (see Sec. 1.1). By removing the CP and losing the orthogonality condition owned by OFDM, i.e., allowing ISI and inter-carrier interference (ICI), OTFS increases the communication rate by handling such interference, which can be considered time and frequency limited under some constraints. Moreover, OTFS results to be not sensitive to Doppler and delay shifts, opening its application to many different scenarios, as depicted throughout this section.

1.3.1 System Model and Definitions

OTFS modulation is produced by a cascade of a pair of two-dimensional transforms, at both Tx and Rx. The general system model of OTFS is depicted in Fig. 1.2. The modulator, through the application of the inverse symplectic finite Fourier transform (ISFFT), first maps the information symbols $x[k,l]$, for $k = 0, \ldots, N-1$ and $l = 0, \ldots, M-1$, belonging to any complex alphabet and represented in the Doppler-delay domain, to symbols $X[n,m]$ in the time-frequency domain (in line with Sec. 1.1). Next, the Heisenberg transform is applied to symbols $X[n,m]$ to build the time domain signal $s(t)$, successively transmitted over the communication channel. At the Rx, the signal $r(t)$ is mapped to the time-frequency domain through the Wigner transform (the inverse of the Heisenberg transform), and then, applying the symplectic finite Fourier transform (SFFT), to the Doppler-delay domain. In the following, by points, we give some more details.

- The Doppler-delay plane is discretized to a grid

$$\Gamma = \left\{ \left(\frac{k}{NT}, \frac{l}{M\Delta f} \right) \right\} , \tag{1.13}$$

  for $k = 0, \dots N-1$ and $l = 0, \dots M-1$, in which $1/M\Delta f = T/M$ and $1/NT = \Delta f/N$ represent the quantization steps of the delay and of the Doppler axes, respectively, in which T is the symbol time and Δf the subcarrier spacing. We set $T = 1/\Delta f$, as for OFDM, choice better justified when deriving the OTFS input-output relation. This Doppler-delay plane representation is very useful for successive analysis and is a key point for OTFS performance.

- The time-frequency discretization is linked to the Doppler-delay representation, given the duality of the time-frequency and the Doppler-delay domains through the application of the Fourier transform. Thus, the sampling occurs at intervals of T and Δf, which defines a grid

$$\Lambda = \{(nT, m\Delta f)\} , \tag{1.14}$$

  for $n = 0, \dots N-1$ and $m = 0, \dots M-1$.

- The OTFS frame has a total duration $T_f^{\mathrm{OTFS}} = NT$ and occupies a total bandwidth $B = M\Delta f$. Note that, unlike OFDM, it is not necessary to introduce a CP, resulting in a shorter total frame duration and a better communication rate (i.e., the amount of information sent in a given time-frequency window).

- Transmit and receive pulses (used within matched filtering operations) are denoted by $g_{\mathrm{tx}}(t)$ and $g_{\mathrm{rx}}(t)$. For convenience, we define here the cross-ambiguity function (CAF) between the two pulses, useful for successive considerations, i.e.,

$$C_{g_{\mathrm{tx}},g_{\mathrm{rx}}}(t,f) \triangleq \int g^*_{\mathrm{rx}}(t'-t)g_{\mathrm{tx}}(t')e^{-j2\pi f t'}dt' \,. \tag{1.15}$$

We adopted the definition of [13], while other expressions might be found in literature (with no significant changes on the final results and system behavior).

- Consider a time-varying channel where the maximum delay and Doppler shift over all multipath components are given by $\tau_{\max}$ and $\nu_{\max}$, respectively. The parameters T and Δf determine the maximum tolerable delay and Doppler, respectively, such that $\nu_{\max} < \Delta f$ and $\tau_{\max} < T$.

We will now look into a detailed derivation of the OTFS input-output relation, which is the base of any signal processing applied afterwords.

1.3.2 Modulation and Transmission over the Channel

The OTFS Tx first maps symbols $x[k,l]$ to samples $X[n,m]$, from the Doppler-delay domain to the time-frequency domain, according to grids Γ and Λ, using the ISFFT, i.e.,

$$X[n,m] = \frac{1}{\sqrt{NM}}\sum_{k=0}^{N-1}\sum_{l=0}^{M-1} x[k,l]\, e^{j2\pi\left(\frac{nk}{N}-\frac{ml}{M}\right)} \,, \tag{1.16}$$

for $n = 0, \dots N-1, m = 0, \dots M-1$.[2] Eq. (1.16) shows that each information symbol $x[k,l]$, belonging to any complex constellation alphabet, is modulated by a two-dimensional basis function in the time-frequency domain, i.e.,

---

[2] Note that, since the ISFFT is a Fourier transformation between two-dimensional domains, a normalization factor has to be taken into account. The normalization factor $1/(NM)$ could be at both direct and inverse transformation, with a square root, of just at one side, without the square root.

$\exp\left(j2\pi\left(\frac{nk}{N}-\frac{ml}{M}\right)\right)$. Next, the time-frequency modulator converts the samples $X[n,m]$ to a continuous-time waveform $s(t)$, by the use of the transmit (shaping) pulse $g_{\mathrm{tx}}(t)$, i.e.,

$$s(t)=\sum_{n=0}^{N-1}\sum_{m=0}^{M-1}X[n,m]\,g_{\mathrm{tx}}(t-nT)e^{j2\pi m\Delta f(t-nT)}\,. \tag{1.17}$$

Eq. (1.17) can be seen as a discrete Heisenberg transform parameterized by $g_{\mathrm{tx}}(t)$ [5, 4]. The pulse $s(t)$ is the product of the superposition of delay-and-modulate operations on the pulse waveform $g_{\mathrm{tx}}(t)$, shifted in time and in frequency. Note that it is useful to express $s(t)$ through an Heisenberg transform since the cascade of two Heisenberg transforms, one for the modulator and one for the channel, can be expressed as a unique function. Note that the equality $\Delta fT=1$ implies

$$e^{j2\pi m\Delta f(t-nT)}=e^{j2\pi m\Delta ft}\,, \tag{1.18}$$

which simplifies (1.17) leading to the equivalent signal model

$$s(t)=\sum_{n=0}^{N-1}\sum_{m=0}^{M-1}X[n,m]\,g_{\mathrm{tx}}(t-nT)e^{j2\pi m\Delta ft}\,, \tag{1.19}$$

which can be found, e.g., in [26, Page 13, Equation (3.4)].

The signal $s(t)$ is transmitted over the time-frequency varying channel with complex baseband CIR $h(\nu,\tau)$ specified in (1.1). The received signal, neglecting for simplicity the noise, is

$$r(t)=\iint h(\nu,\tau)\,s(t-\tau)e^{j2\pi\nu t}d\tau d\nu\,, \tag{1.20}$$

which is a continuous Heisenberg transform parameterized in $h(\nu,\tau)$. Note that, by substituting (1.1) into (1.20), the double integration is valid only where the two deltas are equal to one, simplifying in a single summation over $p=0,\ldots,P-1$. This substitution is done in subsequent calculus.

1.3.3 Demodulation

At the Rx, a matched filter computes the CAF (see (1.15)) in the following way

$$Y\left(t,f\right) = A_{g_{\mathrm{rx}},r}\left(t,f\right) = \int g_{\mathrm{rx}}^{*}\left(t'-t\right) r\left(t'\right) e^{-j2\pi f t'} dt' \,. \tag{1.21}$$

By substituting (1.20) in (1.21), we obtain

$$Y\left(t,f\right) = \int g_{\mathrm{rx}}^{*}\left(t'-t\right) \left[\iint h\left(\nu,\tau\right) s\left(t'-\tau\right) e^{j2\pi\nu t'} d\tau d\nu\right] e^{-j2\pi f t'} dt' \,, \tag{1.22}$$

and, by using (1.17)

$$\begin{aligned} Y\left(t,f\right) = \int g_{\mathrm{rx}}^{*}\left(t'-t\right) \Bigg[\iint \sum_{n'=0}^{N-1}\sum_{m'=0}^{M-1} h\left(\nu,\tau\right) X\left[n',m'\right] g_{\mathrm{tx}}\left(t'-\tau-n'T\right) \\ e^{j2\pi m'\Delta f\left(t'-\tau-n'T\right)} e^{j2\pi\nu t'} d\tau d\nu\Bigg] e^{-j2\pi f t'} dt' \,, \end{aligned} \tag{1.23}$$

while, by reordering terms

$$\begin{aligned} Y\left(t,f\right) = \sum_{n'=0}^{N-1}\sum_{m'=0}^{M-1} X\left[n',m'\right] \Bigg[\iint h\left(\nu,\tau\right) \Bigg\{\int g_{\mathrm{rx}}^{*}\left(t'-t\right) g_{\mathrm{tx}}\left(t'-\tau-n'T\right) \\ e^{j2\pi m'\Delta f\left(t'-\tau-n'T\right)} e^{j2\pi\nu t'} e^{-j2\pi f t'} dt' \Bigg\} d\tau d\nu\Bigg] \,. \end{aligned} \tag{1.24}$$

The matched filter output is obtained by sampling $Y\left(t,f\right)$ as

$$Y\left[n,m\right] = Y\left(t,f\right)\big|_{t=nT,f=m\Delta f} \,. \tag{1.25}$$

Now, by recalling the function inside the square brackets and sampling, we define

$$\begin{aligned} H_{n,m}\left[n',m'\right] = \iint h\left(\nu,\tau\right) \Bigg[\int g_{\mathrm{rx}}^{*}\left(t'-nT\right) g_{\mathrm{tx}}\left(t'-\tau-n'T\right) \\ e^{j2\pi m'\Delta f\left(t'-\tau-n'T\right)} e^{j2\pi\left(\nu-m\Delta f\right)t'} dt'\Bigg] d\tau d\nu \,. \end{aligned} \tag{1.26}$$

By substituting $t'' = t' - \tau - n'T$, we get

$$\begin{aligned} H_{n,m}\left[n',m'\right] &= \iint h\left(\nu,\tau\right)\left[\int g^{*}_{\mathrm{rx}}\left(t'' - \left(n-n'\right)T + \tau\right) g_{\mathrm{tx}}\left(t''\right)\right. \\ &\quad \left. e^{j2\pi m'\Delta f t''} e^{j2\pi\left(\nu - m\Delta f\right)\left(t'' + n'T + \tau\right)} dt''\right] d\tau d\nu \\ &= \iint \left[\int g^{*}_{\mathrm{rx}}\left(t'' - \left(n-n'\right)T + \tau\right) g_{\mathrm{tx}}\left(t''\right)\right. \\ &\quad \left. e^{-j2\pi\left(\left(m-m'\right)\Delta f - \nu\right)t''} dt''\right] h\left(\nu,\tau\right) e^{j2\pi\left(\nu - m\Delta f\right)\left(n'T+\tau\right)} d\tau d\nu \\ &= \iint h\left(\nu,\tau\right) A_{g_{\mathrm{rx}},g_{\mathrm{tx}}}\left(\left(n-n'\right)T - \tau, \left(m-m'\right)\Delta f - \nu\right) \\ &\quad e^{j2\pi\nu n'T} e^{j2\pi\nu\tau} e^{-j2\pi m\Delta f\tau} d\tau d\nu\,, \end{aligned} \tag{1.27}$$

and, by considering the channel specified in (1.1), it becomes

$$\begin{aligned} H_{n,m}\left[n',m'\right] = \sum_{p=0}^{P-1} & h_p A_{g_{\mathrm{rx}},g_{\mathrm{tx}}}\left(\left(n-n'\right)T - \tau_p, \left(m-m'\right)\Delta f - \nu_p\right) \\ & e^{j2\pi\nu_p n'T} e^{j2\pi\nu_p\tau_p} e^{-j2\pi m\Delta f\tau_p}\,. \end{aligned} \tag{1.28}$$

It is straightforward to obtain the input-output relation of OTFS, given by

$$Y\left[n,m\right] = \sum_{n'=0}^{N-1}\sum_{m'=0}^{M-1} H_{n,m}\left[n',m'\right] X\left[n',m'\right]\,. \tag{1.29}$$

Note that Eq.(1.29) can be split to directly and separately show the parts involved in (Doppler-delay) ISI and ICI, thus

$$\begin{aligned}
Y\left[n,m\right] &= \sum_{n'=0}^{N-1}\sum_{m'=0}^{M-1} H_{n,m}\left[n',m'\right] X\left[n',m'\right] \\
&= H_{n,m}\left[n,m\right] X\left[n,m\right] + \sum_{\substack{m'=0\\ m'\neq m}}^{M-1} H_{n,m}\left[n,m'\right] X\left[n,m'\right] \\
&\quad + \sum_{\substack{n'=0\\ n'\neq n}}^{N-1}\sum_{m'=0}^{M-1} H_{n,m}\left[n',m'\right] X\left[n',m'\right] \,,
\end{aligned} \tag{1.30}$$

in which the first term indicates the current symbol $X\left[n,m\right]$, with the associated channel response, the second term is the ICI, i.e., the total interference at different frequencies $m' \neq m$ but within the same time slot n of the current symbol $X\left[n,m\right]$, and, at last, the third term is the ISI. Note that, at this point, the shape of the pulses is unknown, so there are possibly infinite (past and future) interfering terms.

Proceeding further, starting from (1.30) and exploiting (1.16), we obtain

$$\begin{aligned}
Y\left[n,m\right] &= \sum_{n'=0}^{N-1}\sum_{m'=0}^{M-1} H_{n,m}\left[n',m'\right] X\left[n',m'\right] \\
&= \sum_{n'=0}^{N-1}\sum_{m'=0}^{M-1} H_{n,m}\left[n',m'\right] \left[\sum_{k'=0}^{N-1}\sum_{l'=0}^{M-1} \frac{x\left[k',l'\right]}{\sqrt{NM}} e^{j2\pi\left(\frac{n'k'}{N}-\frac{m'l'}{M}\right)}\right] \,.
\end{aligned} \tag{1.31}$$

By applying the ISFFT (from now on, for the sake of brevity, we remove the summation subscripts and superscripts, which are, however, in accord to the aforementioned treatment)

$$\begin{aligned}
y\left[k,l\right] &= \sum_{n,m}\sum_{n',m'}\sum_{k',l'} H_{n,m}\left[n',m'\right]\frac{x\left[k',l'\right]}{NM} e^{j2\pi\left(\frac{n'k'}{N}-\frac{m'l'}{M}\right)} e^{-j2\pi\left(\frac{nk}{N}-\frac{ml}{M}\right)} \\
&= \sum_{k',l'}\frac{x\left[k',l'\right]}{NM}\left[\sum_{n,m}\sum_{n',m'} H_{n,m}\left[n',m'\right] e^{j2\pi\left(\frac{n'k'}{N}-\frac{m'l'}{M}\right)} e^{-j2\pi\left(\frac{nk}{N}-\frac{ml}{M}\right)}\right] \\
&= \sum_{k'}\sum_{l'}\frac{x\left[k',l'\right]}{NM} h_{k,l}\left[k',l'\right] \ , \qquad (1.32)
\end{aligned}$$

in which, by using the definition in (1.28), including the CIR in (1.1), we get

$$\begin{aligned}
h_{k,l}\left[k',l'\right] = &\sum_{N,M}\sum_{n',M'}\sum_{p=0}^{P-1} h_p A_{g_{\mathrm{rx}},g_{\mathrm{tx}}}\left(\left(n-n'\right)T-\tau_p,\left(m-m'\right)\Delta f-\nu_p\right) \\
&e^{j2\pi\nu_p n' T} e^{j2\pi\nu_p\tau_p} e^{-j2\pi m\Delta f\tau_p} e^{j2\pi\left(\frac{n'k'}{N}-\frac{m'l'}{M}\right)} e^{-j2\pi\left(\frac{nk}{N}-\frac{ml}{M}\right)} . \qquad (1.33)
\end{aligned}$$

Note that

$$\begin{aligned}
&A_{g_{\mathrm{tx}},g_{\mathrm{rx}}}\left(\left(n-n'\right)T-\tau,\left(m-m'\right)\Delta f-\nu\right) = \\
&\qquad \int g_{\mathrm{rx}}^{*}\left(t'-\left(n-n'\right)T+\tau\right) g_{\mathrm{tx}}\left(t'\right) e^{-j2\pi\left[\left(m-m'\right)\Delta f-\nu_p\right]t'} dt' \ , \qquad (1.34)
\end{aligned}$$

and since the received signal $r\left(t\right)$ is sampled at time intervals $t'=1/\left(M\Delta f\right)$ or equivalently $t'=T/M$, we get

$$\begin{aligned}
A_{g_{\mathrm{tx}},g_{\mathrm{rx}}} = &\frac{T}{M}\sum_{i=-\infty}^{i=\infty} g_{\mathrm{rx}}^{*}\left(i\frac{T}{M}-\left(n-n'\right)T+\tau_p\right) g_{\mathrm{tx}}\left(i\frac{T}{M}\right) \\
&e^{-j2\pi\left[\left(m-m'\right)\Delta f-\nu_p\right]\frac{i}{M\Delta f}} . \qquad (1.35)
\end{aligned}$$

So, by reordering terms (note that $\Delta f T = 1$) and defining $h'_i = h_i e^{j2\pi\nu\tau}$

$$\begin{aligned}
h_{k,l}\left[k',l'\right] =& \frac{T}{M}\sum_{p=0}^{P-1} h'_p \Bigg\{ \sum_n e^{-j2\pi\left(\frac{k}{N}\right)n} \Bigg[\sum_{n'} e^{j2\pi\left(\frac{k'+\nu_p NT}{N}\right)n'} \\
& \sum_{i=-\infty}^{i=\infty} g^*_{\mathrm{rx}}\left(i\frac{T}{M} - \left(n-n'\right)T + \tau_p\right) g_{\mathrm{tx}}\left(i\frac{T}{M}\right) \\
& \sum_m e^{j2\pi\left(-\Delta f\left(\frac{i}{M\Delta f}+\tau_p\right)+\frac{l}{M}\right)m} \sum_{m'} e^{-j2\pi\left(\frac{l'}{M}-\frac{i}{M}\right)m'} e^{j2\pi\nu_p\frac{i}{M\Delta f}} \Bigg]\Bigg\} \\
=& \frac{T}{M}\sum_{p=0}^{P-1} h'_p \Bigg\{ \sum_n e^{-j2\pi\left(\frac{k}{N}\right)n} \Bigg[\sum_{n'} e^{j2\pi\left(\frac{k'+\nu_p NT}{N}\right)n'} \\
& \sum_{i=-\infty}^{i=\infty} g^*_{\mathrm{rx}}\left(i\frac{T}{M} - \left(n-n'\right)T + \tau_p\right) g_{\mathrm{tx}}\left(i\frac{T}{M}\right) \\
& \left\{\sum_m e^{j2\pi(-i-M\Delta f\tau_p+l)\frac{m}{M}}\right\} \left\{\sum_{m'} e^{-j2\pi(-i+l')\frac{m'}{M}}\right\} e^{j2\pi\nu_p\frac{i}{M\Delta f}} \Bigg]\Bigg\}.
\end{aligned} \tag{1.36}$$

At this point, it is useful to define the Dirichlet kernel function, that is

$$\begin{aligned}
\mathrm{Dir}\left(\phi, Z\right) \triangleq \sum_{z=0}^{Z-1} e^{j2\pi\phi\frac{z}{Z}} &= \frac{e^{j2\pi\phi}-1}{e^{j2\pi\phi/Z}-1} = \frac{e^{j\pi\phi}\left(e^{j\pi\phi}-e^{-j\pi\phi}\right)}{e^{j\pi\phi/Z}\left(e^{j\pi\phi/Z}-e^{-j\pi\phi/Z}\right)} \\
&= e^{j\pi\phi(Z-1)/Z}\frac{\sin\left(\pi\phi\right)}{\sin\left(\pi\phi/Z\right)}.
\end{aligned} \tag{1.37}$$

A plot of the function is given in Fig. 1.3. The value of the function is equal to Z (or $-Z$ depending if Z is even or odd) when ϕ is a multiple of Z, and is equal to zero for all others integer values of ϕ. Moreover, note that the Dirichlet kernel has the following property

$$\frac{\sin\left(\pi\phi\right)}{\sin\left(\frac{\pi}{Z}\phi\right)} = \frac{\sin\left(\pi\left(\phi+Z\right)\right)}{\sin\left(\frac{\pi}{Z}\left(\phi+Z\right)\right)}. \tag{1.38}$$

which could be useful for successive analysis.

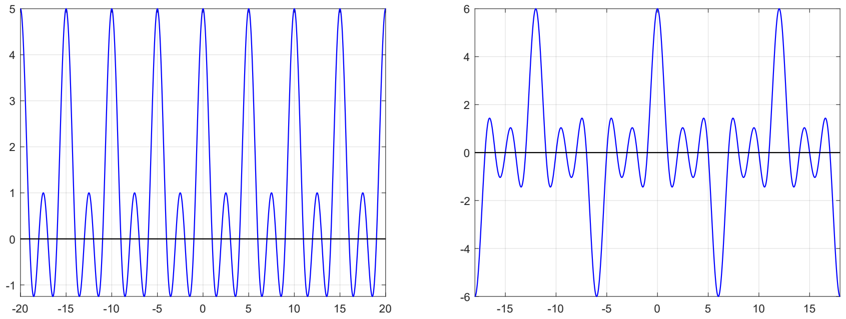

(a) $Z = 5$. (b) $Z = 6$.

Figure 1.3: Example of Dirichlet functions $\text{Dir}\left(\phi, Z\right) = \frac{\sin(\pi\phi)}{\sin(\pi\phi/Z)}$.

Thus, the expression for $y\left[k,l\right]$ becomes

$$\begin{aligned}
y\left[k,l\right] =& \sum_{k',l'} \frac{x\left[k',l'\right]}{NM} \frac{T}{M} \sum_{p=0}^{P-1} h'_p \Bigg\{ \sum_{n} e^{-j2\pi k \frac{n}{N}} \sum_{n'} \Bigg[\sum_{i=-\infty}^{\infty} g_{\text{tx}}\left(i\frac{T}{M}\right) \\
& g^*_{\text{rx}}\left(i\frac{T}{M} - \left(n-n'\right)T + \tau_p\right) \text{Dir}\left(l - i - \tau_p M \Delta f, M\right) \\
& \text{Dir}\left(l' - i, M\right) e^{j2\pi\nu_p \frac{i}{M\Delta f}} \Bigg] e^{j2\pi\left(k' + \nu_p NT\right)\frac{n'}{N}} \Bigg\} \\
=& \sum_{k',l'} \frac{x\left[k',l'\right]}{NM} T \sum_{p=0}^{P-1} h'_p \Bigg\{ \sum_{n} \sum_{n'} g^*_{\text{rx}}\left(l'\frac{T}{M} - \left(n-n'\right)T + \tau_p\right) \\
& g_{\text{tx}}\left(l'\frac{T}{M}\right) \text{Dir}\left(l - l' - \tau_p M \Delta f, M\right) e^{-j2\pi k \frac{n}{N}} e^{j2\pi\nu_p \frac{l'}{M\Delta f}} \\
& e^{j2\pi\left(k' + \nu_p NT\right)\frac{n'}{N}} \Bigg\}. \qquad (1.39)
\end{aligned}$$

1.3.4 Special Case: Rectangular Waveforms

As a practical special case, consider a rectangular waveform of duration T and amplitude $1/\sqrt{T}$, i.e., $g_{\text{tx}}(t) = g_{\text{rx}}(t) = \text{rect}(t)$, as defined in (1.2). If $\tau_{\max} < T$, only the signal of the first preceding slot is involved in the ISI calculation, i.e.,

$n' = n - 1$. In this case

$$g^*_{\text{rx}}\left(p\frac{T}{M} - T + \tau_p\right) g_{\text{tx}}\left(p\frac{T}{M}\right) = \frac{1}{\sqrt{T}}\frac{1}{\sqrt{T}} = \frac{1}{T}\,, \tag{1.40}$$

for the values of p where the product of the two pulses is nonzero. Thus, for rectangular pulses, the sum $\sum_{n'}$ takes into account only two terms, i.e., $n' = n$ and $n' = n - 1$. By using these results, starting from (1.39), we obtain

$$\begin{aligned} y^{\text{rect}}[k,l] = {} & \sum_{k',l'} \frac{x[k',l']}{NM} \sum_{p=0}^{P-1} h'_p \Bigg(\Bigg\{ \sum_n e^{-j2\pi(k-k'-\nu_p NT)\frac{n}{N}} e^{j2\pi\nu_p\frac{l'}{M\Delta f}} \\ & \text{Dir}\left(l - l' - \tau_p M\Delta f, M\right) \Bigg\} + \Bigg\{ \sum_n e^{-j2\pi(k-k'-\nu_p NT)\frac{n}{N}} \\ & \text{Dir}\left(l - l' - \tau_p M\Delta f, M\right) e^{j2\pi\nu_p\frac{l'}{M\Delta f}} e^{-j2\pi\frac{(k'+\nu_p NT)}{N}} \Bigg\} \Bigg) \\ = {} & \sum_{k',l'} \frac{x[k',l']}{NM} \sum_{p=0}^{P-1} h'_p \text{Dir}\left(\nu_p NT - k + k', N\right) e^{j2\pi\nu_p\frac{l'}{M\Delta f}} \\ & \text{Dir}\left(l - l' - \tau_p M\Delta f, M\right) \left(1 + e^{-j2\pi\frac{k'+\nu_p NT}{N}}\right)\,. \end{aligned} \tag{1.41}$$

However, note that, having considered the multiplication between the two rectangular pulses $g_{\text{tx}}(t)$ and $g_{\text{rx}}(t)$, the l' involved in the two terms inside the curly brackets is different, since it considers the pulses overlap within the interval $[0, M-1-\lceil\tau_p/(T/M)\rceil]$ and $[M-1-\lfloor\tau_p/(T/M)\rfloor, M-1]$, where $\lceil\cdot\rceil$ and $\lfloor\cdot\rfloor$ indicates the nearest upper and lower integer, respectively. We finally get

$$\begin{aligned} y[k,l] = {} & \sum_{p=0}^{P-1} h'_p \sum_{k'} \text{Dir}\left(\nu_p NT - k + k', N\right) \sum_{l'} \text{Dir}\left(l - l' - \tau_p M\Delta f, M\right) \\ & e^{j2\pi\nu_p\left(\frac{l'}{M\Delta f}\right)} \frac{x[k',l']}{NM} \times \begin{cases} 1 & \text{if } l' \in l'_{\text{ISI}} \\ e^{-j2\pi\left(\nu_p T + \frac{k'}{N}\right)} & \text{if } l' \in l'_{\text{ICI}} \end{cases}, \end{aligned} \tag{1.42}$$

where we used

$$\begin{cases} l'_{\text{ISI}} \triangleq \left\{0, M-1-\lceil \frac{\tau_p}{T/M} \rceil\right\} \\ l'_{\text{ICI}} \triangleq \left\{M-1-\lfloor \frac{\tau_p}{T/M} \rfloor, M-1\right\} \end{cases}. \tag{1.43}$$

Thus, the channel matrix expression for the p-th path becomes

$$\begin{aligned} \mathbf{\Psi}^p_{k,k'}\left[l,l'\right] = \frac{1}{NM}\text{Dir}\left(\nu_p NT - k + k', N\right)\text{Dir}\left(l - l' - \tau_p M\Delta f, M\right) \\ e^{j2\pi\nu_p\left(\frac{l'}{M\Delta f}\right)} \times \begin{cases} 1 & l' \in l'_{\text{ICI}} \\ e^{-j2\pi\left(\nu_p T + \frac{k'}{N}\right)} & l' \in l'_{\text{ISI}} \end{cases}. \end{aligned} \tag{1.44}$$

The input output relation becomes

$$y\left[k,l\right] = \sum_{k',l'}\sum_{p=0}^{P-1} h'_p \mathbf{\Psi}^p_{k,k'}\left[l,l'\right] x\left[k',l'\right] , \tag{1.45}$$

which can be represented in matrix form as

$$\mathbf{y} = \left(\sum_{p=0}^{P-1} h'_p \mathbf{\Psi}^p\right)\mathbf{x}\,, \tag{1.46}$$

with $\mathbf{y}$ and $\mathbf{x}$ vectors of dimension $NM \times 1$ obtained by stacking the received samples and information symbols, respectively, and $\mathbf{\Psi}^p$ matrix of dimension $MN \times MN$, whose $\{k, k', l, l'\}$ element is defined in (1.44).

1.3.5 Considerations on matrix $\mathbf{\Psi}$

We now consider some special cases of matrix $\mathbf{\Psi}^p$, for any single path p.

- **Zero delay — Zero Doppler**: $\tau_p = \nu_p = 0$.

$$\mathbf{\Psi}^p_{k,k'}\left[l,l'\right] = \begin{cases} 1 & \text{if } (l = l', k = k') \\ 0 & \text{else} \end{cases}. \tag{1.47}$$

When both delay and Doppler are zero, $\mathbf{\Psi}^p$ results to be the identity matrix. The channel does not modify the transmitted symbols, the received signal is simply $\mathbf{y} = \mathbf{x} + \text{noise}$.

- **Non-zero delay — Zero Doppler**: $\tau_p \neq 0, \nu_p = 0$.

$$\boldsymbol{\Psi}^p_{k,k'}\left[l,l'\right] = \frac{1}{M}\mathrm{Dir}\left(l-l'-\tau_p M\Delta f, M\right) \times \begin{cases} 1 & \text{if } (k=k') \\ 0 & \text{else} \end{cases} . \tag{1.48}$$

Let us describe the delay τ_p using its integer and fractional parts, i.e., l_{τ_p} and κ_{τ_p} respectively, such that $\tau_p = l_{\tau_p} + \kappa_{\tau_p}$. Matrix $\boldsymbol{\Psi}^p$ is structured such that there are N^2 equal $M \times M$ delay submatrices, arranged in a $N \times N$ structure describing the Dirichlet function behavior associated to the Doppler shift. The integer part l_{τ_p} of the delay determines the row of the $M \times M$ submatrix whose highest value (in magnitude) is on the first position (first column). On the other hand, the fractional part affects the spreading around the peak value, according to the delay Dirichlet function. For instance, with $M = 4$, by defining

$$\psi^{\tau_p}_{l-l'} \triangleq \frac{1}{M}\mathrm{Dir}\left(l-l'-\tau_p M\Delta f, M\right) , \tag{1.49}$$

the $M \times M$ matrices are (peak coefficients are in bold)

$$l_\tau = 0 : \begin{bmatrix} \boldsymbol{\psi^{\tau_p}_0} & \psi^{\tau_p}_{-1} & \psi^{\tau_p}_{-2} & \psi^{\tau_p}_{-3} \\ \psi^{\tau_p}_1 & \psi^{\tau_p}_0 & \psi^{\tau_p}_{-1} & \psi^{\tau_p}_{-2} \\ \psi^{\tau_p}_2 & \psi^{\tau_p}_1 & \psi^{\tau_p}_0 & \psi^{\tau_p}_{-1} \\ \psi^{\tau_p}_3 & \psi^{\tau_p}_2 & \psi^{\tau_p}_1 & \psi^{\tau_p}_0 \end{bmatrix}$$

$$l_\tau = 1 : \begin{bmatrix} \psi^{\tau_p}_0 & \psi^{\tau_p}_{-1} & \psi^{\tau_p}_{-2} & \psi^{\tau_p}_{-3} \\ \boldsymbol{\psi^{\tau_p}_1} & \psi^{\tau_p}_0 & \psi^{\tau_p}_{-1} & \psi^{\tau_p}_{-2} \\ \psi^{\tau_p}_2 & \psi^{\tau_p}_1 & \psi^{\tau_p}_0 & \psi^{\tau_p}_{-1} \\ \psi^{\tau_p}_3 & \psi^{\tau_p}_2 & \psi^{\tau_p}_1 & \psi^{\tau_p}_0 \end{bmatrix}$$

$$\vdots$$

$$l_\tau = M-1 : \begin{bmatrix} \psi^{\tau_p}_0 & \psi^{\tau_p}_{-1} & \psi^{\tau_p}_{-2} & \psi^{\tau_p}_{-3} \\ \psi^{\tau_p}_1 & \psi^{\tau_p}_0 & \psi^{\tau_p}_{-1} & \psi^{\tau_p}_{-2} \\ \psi^{\tau_p}_2 & \psi^{\tau_p}_1 & \psi^{\tau_p}_0 & \psi^{\tau_p}_{-1} \\ \boldsymbol{\psi^{\tau_p}_3} & \psi^{\tau_p}_2 & \psi^{\tau_p}_1 & \psi^{\tau_p}_0 \end{bmatrix} ,$$

and, by taking into account the modulo operations such that

$$l - l' \to \operatorname{mod}\left(l - l', M\right) \ , \quad k - k' \to \operatorname{mod}\left(k - k', N\right) \ , \tag{1.50}$$

we obtain

$$l_\tau = 0 : \begin{bmatrix} \boldsymbol{\psi_0^{\tau_p}} & \psi_3^{\tau_p} & \psi_2^{\tau_p} & \psi_1^{\tau_p} \\ \psi_1^{\tau_p} & \psi_0^{\tau_p} & \psi_3^{\tau_p} & \psi_2^{\tau_p} \\ \psi_2^{\tau_p} & \psi_1^{\tau_p} & \psi_0^{\tau_p} & \psi_3^{\tau_p} \\ \psi_3^{\tau_p} & \psi_2^{\tau_p} & \psi_1^{\tau_p} & \psi_0^{\tau_p} \end{bmatrix}$$

$$l_\tau = 1 : \begin{bmatrix} \psi_0^{\tau_p} & \psi_3^{\tau_p} & \psi_2^{\tau_p} & \psi_3^{\tau_p} \\ \boldsymbol{\psi_1^{\tau_p}} & \psi_0^{\tau_p} & \psi_3^{\tau_p} & \psi_2^{\tau_p} \\ \psi_2^{\tau_p} & \psi_1^{\tau_p} & \psi_0^{\tau_p} & \psi_1^{\tau_p} \\ \psi_3^{\tau_p} & \psi_2^{\tau_p} & \psi_1^{\tau_p} & \psi_0^{\tau_p} \end{bmatrix}$$

$$\vdots$$

$$l_\tau = M-1 : \begin{bmatrix} \psi_0^{\tau_p} & \psi_3^{\tau_p} & \psi_2^{\tau_p} & \psi_1^{\tau_p} \\ \psi_1^{\tau_p} & \psi_0^{\tau_p} & \psi_3^{\tau_p} & \psi_2^{\tau_p} \\ \psi_2^{\tau_p} & \psi_1^{\tau_p} & \psi_0^{\tau_p} & \psi_3^{\tau_p} \\ \boldsymbol{\psi_3^{\tau_p}} & \psi_2^{\tau_p} & \psi_1^{\tau_p} & \psi_0^{\tau_p} \end{bmatrix} ,$$

where it is clearly visible that each row is a circular shift of the previous one.

- **Zero delay — Non-zero Doppler**: $\tau_p = 0, \nu_p \neq 0$

$$\boldsymbol{\Psi}^i_{k,k'}\left[l, l'\right] = \frac{1}{N}\mathrm{Dir}\left(-\nu_p NT - k + k', N\right) e^{j2\pi\nu_p\left(\frac{l'}{M\Delta f}\right)} \times \begin{cases} 1 & \text{if } l = l' \\ 0 & \text{else} \end{cases} . \tag{1.51}$$

In case of zero delay there is no ISI. Since $\tau_p = 0$, the contribution of the delay Dirichlet function leads to $\psi_{l,l'} = 1$, for $l = l'$, i.e., the coefficients on the main diagonal of the $M \times M$ matrices. However, in this case, there is an additional exponential term, i.e., $e^{j2\pi\nu_p\left(\frac{l'}{M\Delta f}\right)}$, which modifies the ψ coefficients depending on the position l'. Moreover, as said before, the non-zero Dirichlet function related to (k, k', ν) involves duplicates of the reference $M \times M$ matrix for different couples (k, k').

For example, with $M = 2$ and $N = 3$, by defining

$$\lambda_{k-k'}^{\nu_p} \triangleq \mathrm{Dir}\left(-\nu_p NT - k + k', N\right) , \tag{1.52}$$

with

$$\lambda_x \triangleq \lambda_{\mathrm{mod}(x,N)} \, , \forall x \in \mathbb{Z} \, , \tag{1.53}$$

and

$$\psi_{l-l',l'}^{\tau_p} \triangleq \frac{1}{M} \mathrm{Dir}\left(l - l' - \tau_p M \Delta f, M\right) e^{j2\pi\nu_p\left(\frac{l'}{M\Delta f}\right)} = \psi_{0,l}^{\tau_p} \, , \tag{1.54}$$

matrix $\mathbf{\Psi}^p$ is

$$\mathbf{\Psi}^p = \left[\begin{array}{c|c|c} \begin{pmatrix} \psi_{0,0}^{\tau_p} & 0 \\ 0 & \psi_{0,1}^{\tau_p} \end{pmatrix} \lambda_0^{\nu_p} & \begin{pmatrix} \psi_{0,0}^{\tau_p} & 0 \\ 0 & \psi_{0,1}^{\tau_p} \end{pmatrix} \lambda_2^{\nu_p} & \begin{pmatrix} \psi_{0,0}^{\tau_p} & 0 \\ 0 & \psi_{0,1}^{\tau_p} \end{pmatrix} \lambda_1^{\nu_p} \\ \hline \begin{pmatrix} \psi_{0,0}^{\tau_p} & 0 \\ 0 & \psi_{0,1}^{\tau_p} \end{pmatrix} \lambda_1^{\nu_p} & \begin{pmatrix} \psi_{0,0}^{\tau_p} & 0 \\ 0 & \psi_{0,1}^{\tau_p} \end{pmatrix} \lambda_0^{\nu_p} & \begin{pmatrix} \psi_{0,0}^{\tau_p} & 0 \\ 0 & \psi_{0,1}^{\tau_p} \end{pmatrix} \lambda_2^{\nu_p} \\ \hline \begin{pmatrix} \psi_{0,0}^{\tau_p} & 0 \\ 0 & \psi_{0,1}^{\tau_p} \end{pmatrix} \lambda_2^{\nu_p} & \begin{pmatrix} \psi_{0,0}^{\tau_p} & 0 \\ 0 & \psi_{0,1}^{\tau_p} \end{pmatrix} \lambda_1^{\nu_p} & \begin{pmatrix} \psi_{0,0}^{\tau_p} & 0 \\ 0 & \psi_{0,1}^{\tau_p} \end{pmatrix} \lambda_0^{\nu_p} \end{array}\right] .$$

- **Non-zero delay — Non-zero Doppler**: $\tau_p \neq 0, \nu_p \neq 0$

$$\begin{aligned} \mathbf{\Psi}_{k,k'}^p \left[l, l'\right] = & \frac{1}{NM} \mathrm{Dir}\left(-\nu_p NT - k + k', N\right) \mathrm{Dir}\left(l - l' - \tau_p M \Delta f, M\right) \\ & e^{j2\pi\nu_p\left(\frac{l'}{M\Delta f}\right)} \times \begin{cases} 1 & l'_{\mathrm{ICI}} \\ e^{-j2\pi\left(\nu_p T + \frac{k'}{N}\right)} & l'_{\mathrm{ISI}} \end{cases} . \end{aligned} \tag{1.55}$$

This is the most general case, where the channel matrix is described as in (1.44). For instance, for $M = 4$, $N = 3$, and ISI of one symbol (rectangular pulses), every $M \times M$ matrix looks like

$$\left[\begin{pmatrix} \psi_{0,0}^{\tau_p} & \psi_{3,1}^{\tau_p} & \psi_{2,2}^{\tau_p} & \psi_{1,3}^{\prime\tau_p}(k') \\ \psi_{1,0}^{\tau_p} & \psi_{0,1}^{\tau_p} & \psi_{3,2}^{\tau_p} & \psi_{2,3}^{\prime\tau_p}(k') \\ \psi_{2,0}^{\tau_p} & \psi_{1,1}^{\tau_p} & \psi_{0,2}^{\tau_p} & \psi_{3,3}^{\prime\tau_p}(k') \\ \psi_{3,0}^{\tau_p} & \psi_{2,1}^{\tau_p} & \psi_{1,2}^{\tau_p} & \psi_{0,3}^{\prime\tau_p}(k') \end{pmatrix} \lambda_{k-k'}^{\nu_p} \right] , \tag{1.56}$$

in which

$$\psi_{l-l',l'}^{\tau_p} = \mathrm{Dir}\left(l-l'-\tau_p M\Delta f, M\right) e^{j2\pi\nu_p\left(\frac{l'}{M\Delta f}\right)} ,$$

$$\psi_{l-l',l'}^{\prime\tau_p}\left(k'\right) = \mathrm{Dir}\left(l-l', M-\tau_p M\Delta f, M\right) e^{j2\pi\nu_p\left(\frac{l'}{M\Delta f}\right)} e^{-j2\pi\left(\nu_p T+\frac{k'}{N}\right)} ,$$

$$\lambda_{k-k'}^{\nu_p} = \mathrm{Dir}\left(k'-k, N-\nu_p NT, N\right) .$$

Note that the circular shift property is lost, because only a subset of columns depends on k'.

Note: the function involved in the ISI term, i.e., $\psi\left(k'\right)$, takes into account the term

$$e^{-j2\pi\frac{k'}{N}} , \tag{1.57}$$

which is a phasor moving on the unit complex circle. For high enough N, since the complex circle is divided in N equal angular steps, values within a certain range are similar to each other. In fact, by taking a reference k', values of the phasor around k' are just slightly different from the reference point. Hence:

- For large enough N, $e^{-j2\pi\frac{k'}{N}} \approx e^{-j2\pi\frac{k'\pm\varepsilon}{N}}$, for small $\varepsilon \in \mathbb{N}$. Using this approximation, each row can be seen as circular shifts of the previous one. However, each row is a circular shift of the previous one and not of the first one. Circular properties are anyway lost.

Note: to simplify the expression of matrix $\mathbf{\Psi}^p$, the dependency on k' has to be removed. In order to have equal $M \times M$ matrices, i.e., independent of k', the ISI must be canceled, e.g., by inserting a CP, but leading to an OFDM-like scheme.

General Matrix $\mathbf{\Psi}^p$ Example: Suppose to have $M = 6$, $N = 5$, and to consider only off-one peak value (left and right) for both Dirichlet functions. For $l_{\tau_p} = 0$, such maximum value of the delay Dirichlet function is in position

$(0,0)$ and then in successive circular shifts, the $M \times M$ matrix is

$$\boldsymbol{\psi}\left(k,k'\right) = \left[\begin{pmatrix} \psi_0^{\tau_p} & \psi_2^{\tau_p} & 0 & 0 & 0 & \psi_1^{\prime\tau_p}\left(k'\right) \\ \psi_1^{\tau_p} & \psi_0^{\tau_p} & \psi_2^{\tau_p} & 0 & 0 & 0 \\ 0 & \psi_1^{\tau_p} & \psi_0^{\tau_p} & \psi_2^{\prime\tau_p} & 0 & 0 \\ 0 & 0 & \psi_1^{\tau_p} & \psi_0^{\tau_p} & \psi_2^{\prime\tau_p} & 0 \\ 0 & 0 & 0 & \psi_1^{\tau_p} & \psi_0^{\tau_p} & \psi_2^{\prime\tau_p}\left(k'\right) \\ \psi_2^{\tau_p} & 0 & 0 & 0 & \psi_1^{\tau_p} & \psi_0^{\prime\tau_p}\left(k'\right) \end{pmatrix} \lambda_{k-k'}^{\nu_p}\right], \tag{1.58}$$

and matrix $\boldsymbol{\Psi}^p$ is

$$\boldsymbol{\Psi}^p = \left[\begin{array}{c|c|c|c|c} \boldsymbol{\psi}\left(0,0\right) & \boldsymbol{\psi}\left(0,1\right) & \mathbf{0} & \mathbf{0} & \boldsymbol{\psi}\left(0,4\right) \\ \hline \boldsymbol{\psi}\left(1,0\right) & \boldsymbol{\psi}\left(1,1\right) & \boldsymbol{\psi}\left(1,2\right) & \mathbf{0} & \mathbf{0} \\ \hline \mathbf{0} & \boldsymbol{\psi}\left(2,1\right) & \boldsymbol{\psi}\left(2,2\right) & \boldsymbol{\psi}\left(2,3\right) & \mathbf{0} \\ \hline \mathbf{0} & \mathbf{0} & \boldsymbol{\psi}\left(3,2\right) & \boldsymbol{\psi}\left(3,3\right) & \boldsymbol{\psi}\left(3,4\right) \\ \hline \boldsymbol{\psi}\left(4,0\right) & \mathbf{0} & \mathbf{0} & \boldsymbol{\psi}\left(4,3\right) & \boldsymbol{\psi}\left(4,4\right) \end{array}\right]. \tag{1.59}$$

1.3.6 Symbols shift within the Doppler-delay grid

Given the channel representation in the Doppler-delay domain, each symbol $x \in \Gamma$ is shifted both in delay and in Doppler. From the above description of the channel matrix $\boldsymbol{\Psi}$, focus the attention on the multiplication $\boldsymbol{\Psi}\mathbf{x}$: the channel effect on a given symbol x_i, for any i, is completely described by the i-th column of $\boldsymbol{\Psi}$, i.e., the one multiplying x_i. It is easy to see that all subcolumns, i.e., each column belonging to one of the N submatrices of dimension $M \times M$, are equal, and they describe the shift in the delay domain. Moreover, for any shift in the Doppler domain, governed by the coefficient λ for any of the N submatrices, the shift in the delay domain is equal. As a result, each transmitted symbol reflects in a received sample showing one peak value on the Doppler-delay received grid surrounded by interfering terms, in accord with the Dirichlet functions behavior.

A visual example, depicted in Fig. 1.4, is useful. The black square in Fig. 1.4 (a) represents the transmitted symbol magnitude (just one, for simplicity).

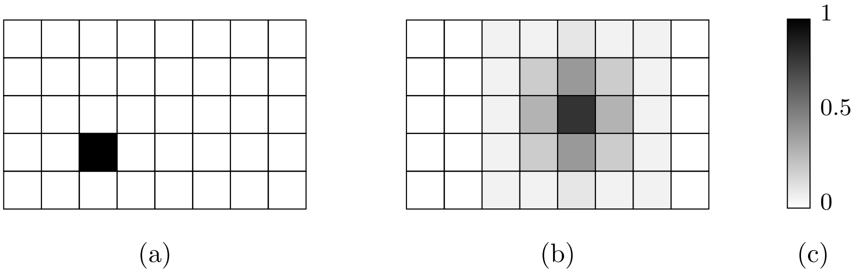

(a) (b) (c)

Figure 1.4: Symbol (magnitude) shift in the Doppler-delay domain. (a) Transmitted symbol. (b) Received samples. (c) Heatmap (magnitude).

The received samples magnitude are shown in Fig. 1.4 (b), such that gray shades exploits the Dirichlet behavior causing ISI and ICI in the Doppler-delay domain. Fig. 1.4 is just a toy example but provides an idea of the Dirichlet functions effect on off-peak points. Moreover, to complete the analysis, Fig. 1.5 depicts another visual example showing the Dirichlet behavior (in magnitude) in two dimensions, which is the accurate description of the qualitative example of Fig. 1.4.

1.3.7 General Waveforms

The choice of pulses $g_{\mathrm{tx}}(t)$ and $g_{\mathrm{rx}}(t)$ implies different behaviors in the time-frequency domain, which are described by the CAF, first appearing in (1.21) and then within the derivation of the OTFS input-output relation. The choice of such waveforms is directly linked to the inter-pulse interference in the time-frequency domain, which implies ISI and ICI.

Consider general pulses with any support, e.g., not limited to $[0, T]$.[3] By keeping the maximum channel delay condition w.r.t. the symbol time as $\tau_{\max} < T$, the number of pulses involved in the ISI clearly depends on the pulse

---

[3] The occupied band in the frequency domain depends only on the definition of the pulse in time domain. To be consistent, we suppose that the support in frequency domain is also not limited.

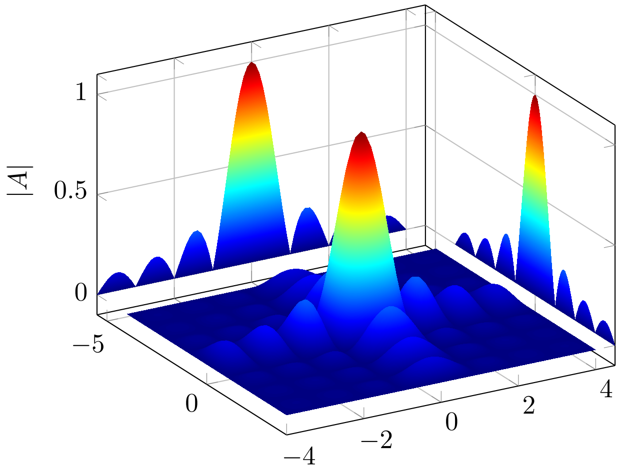

Figure 1.5: Two dimensions visual example of Dirichlet functions in both domains, where $|A|$ is the normalized amplitude value, in accord to the heatmap of Fig. 1.4.

support. By starting from (1.39) and defining $q \triangleq (n - n')$, we get

$$
\begin{aligned}
y\left[k,l\right] = {} & \frac{T}{NM}\sum_{k',l'} x\left[k',l'\right] \sum_{p=0}^{P-1} h'_p \Bigg\{ \sum_{n} e^{-j2\pi k \frac{n}{N}} \sum_{n'} e^{j2\pi\left(k'+\nu_p NT\right)\frac{n'}{N}} e^{j2\pi \nu_p \frac{l'}{M\Delta f}} \\
& g^*_{\mathrm{rx}}\left(l'\frac{T}{M} - \left(n-n'\right)T + \tau_p\right) g_{\mathrm{tx}}\left(l'\frac{T}{M}\right) \mathrm{Dir}\left(l - l' - \tau_p M \Delta f, M\right) \Bigg\} \\
= {} & \sum_{k',l'} \frac{x\left[k',l'\right]T}{NM} \sum_{p=0}^{P-1} h'_p \Bigg\{ \sum_{n} e^{-j2\pi k \frac{n}{N}} \sum_{q=-\infty}^{\infty} e^{j2\pi\left(k'+\nu_p NT\right)\frac{n-q}{N}} e^{j2\pi \nu_p \frac{l'}{M\Delta f}} \\
& g^*_{\mathrm{rx}}\left(l'\frac{T}{M} - qT + \tau_p\right) g_{\mathrm{tx}}\left(l'\frac{T}{M}\right) \mathrm{Dir}\left(l - l' - \tau_p M \Delta f, M\right) \Bigg\} \\
= {} & \frac{x\left[k',l'\right]T}{NM} \sum_{k',l'} \sum_{p=0}^{P-1} h'_p g_{\mathrm{tx}}\left(l'\frac{T}{M}\right) \mathrm{Dir}\left(l - l' - \tau_p M \Delta f, M\right) e^{j2\pi \nu_p \frac{l'}{M\Delta f}} \\
& \left(\sum_{n} e^{j2\pi\left(k'+\nu_p NT - k\right)\frac{n}{N}}\right) \sum_{q=-\infty}^{\infty} e^{-j2\pi\left(k'+\nu_p NT\right)\frac{q}{N}} g^*_{\mathrm{rx}}\left(l'\frac{T}{M} - qT + \tau_p\right).
\end{aligned}
\tag{1.60}
$$

Note that only the term in brackets depends on n, and it is a Dirichlet function

$$\sum_{n} e^{j2\pi(k'+\nu_p NT-k)\frac{n}{N}} \triangleq \mathrm{Dir}\left(\nu_p NT - k + k', N\right) . \tag{1.61}$$

Hence

$$\begin{aligned} y\left[k,l\right] = \sum_{k',l'} \frac{x\left[k',l'\right]T}{NM} \sum_{p=0}^{P-1} & h'_p \mathrm{Dir}\left(l - l' - \tau_p M\Delta f, M\right) \mathrm{Dir}\left(\nu_p NT - k + k', N\right) \\ & g_{\mathrm{tx}}\left(l'\frac{T}{M}\right) \left\{ \sum_{q=-\infty}^{\infty} e^{-j2\pi(k'+\nu_p NT)\frac{q}{N}} g^*_{\mathrm{rx}}\left(l'\frac{T}{M} - qT + \tau_p\right) \right\} \\ & e^{j2\pi\nu_p \frac{l'}{M\Delta f}} . \end{aligned} \tag{1.62}$$

The term under curly brackets takes into account interfering pulses shifted of multiples of T w.r.t. the summation index q. Depending on the support of the pulses, i.e., when the energy is above a certain threshold if the pulse support is infinite, only a fixed number of interferes appears (to left and to right), indicated by I_p. The summation over q can be thus limited to $[-I_p, I_p]$. We finally get

$$\begin{aligned} y\left[k,l\right] = \sum_{k',l'} \frac{x\left[k',l'\right]T}{NM} \sum_{p=0}^{P-1} & h'_p \mathrm{Dir}\left(l - l' - \tau_p M\Delta f, M\right) \mathrm{Dir}\left(\nu_p NT - k + k', N\right) \\ & e^{j2\pi\nu_p \frac{l'}{M\Delta f}} g_{\mathrm{tx}}\left(l'\frac{T}{M}\right) \left\{ \sum_{q=-I_p}^{I_p} e^{-j2\pi(k'+\nu_p NT)\frac{q}{N}} g^*_{\mathrm{rx}}\left(l'\frac{T}{M} - qT + \tau_p\right) \right\} . \end{aligned} \tag{1.63}$$

Note that a pulse not satisfying the Nyquist condition, i.e., flat frequency representation, changes the noise properties. The noise associated to the received samples is not white anymore, and changes within the pulse definition. This fact must be considered in the mathematical and simulation model.

What is the role of the shaping pulses in the construction of the channel matrix $\mathbf{\Psi}$? The structure of $\mathbf{\Psi}$ is dominated by the Dirichlet function values, w.r.t. the integer/fractional delay and Doppler shifts and the indices l, l', k, k'.

The ISI and ICI effects caused by the shaping pulses add to the Dirichlet behavior, but how? One can think that optimized "well-known" pulses having limited CAF in time-frequency domain should be adopted [60], but the effect in the dual Doppler-delay domain remains not clear. In fact, the Doppler-delay ISI and ICI weakly depend on the adopted shaping pulse, and are dominated by the Dirichlet functions, whose expressions appear from the particular transformations performed by modulator and demodulator, and not from the choice of the transmitted and received pulses (see Sec. 1.3.1). For these reasons, once common well-confined time-frequency pulses are adopted [60], it is not guaranteed to achieve good performance also in the Doppler-delay domain. This fact is also confirmed in [61].

The conclusion could be that, whatever the chosen pulse (also different between transmitter and Rx), there are no performance guarantees. For completeness, the next section will present some known pulses and the associated CAFs, together with final considerations on the adopted pulses.

1.3.8 The Cross-Ambiguity Function

In radar scenarios, the CAF is a two-dimensional function of delay and Doppler showing the distortion of a returned pulse at the Rx matched filter due to delay and Doppler shift of the moving target (see, e.g., [13, 60]). The ambiguity function description is only determined by the properties of the transmitted pulse and the matched filter (received pulse). By taking into account the definition of CAF in (1.15) [13], recalled here for convenience

$$C_{g_{\text{tx}},g_{\text{rx}}}(t,f) \triangleq \int g_{\text{rx}}^*(t'-t)g_{\text{tx}}(t')e^{-j2\pi ft'}dt' \,, \tag{1.64}$$

we show its behavior when different pulses $g_{\text{tx}}(t)$ and $g_{\text{tx}}(t)$ are used.

Fig. 1.6 shows that different pulses achieve distinct performance in terms of spreading in time and in frequency of the CAF. For instance, as shown in Fig. 1.6 (a), since rectangular pulses have infinite support in the frequency domain, the projection of the CAF on the frequency plane slowly decays and necessitates some time to reach the zero “floor”, while values near the peak point have remarkable magnitude. A different behavior is shown when two Gaussian pulses are adopted (Fig. 1.6 (b)). In fact, having Gaussian pulses finite support in the frequency domain, they exhibit a rapid decay to zero around peak point. A similar consideration occurs in the time domain, which is confirmed by looking at the projection on the time plane. At last, compare Fig. 1.6 (b) and 1.6 (c) to have an idea on how Gaussian pulses with different variances change the behavior of the projections over the time and frequency planes. The definition of good shaping pulses, with the corresponding CAF, is a problem of primary interest in typical radar systems. For more details, for instance, refer to the analysis carried on in [60], suggesting the use of pulses well localized in the time-frequency domain.

Regarding OTFS, pioneering works [4, 5] are based on the assumption of ideal bi-orthogonal pulses satisfying perfect interference properties, i.e., resulting to be deltas in both time and frequency planes. However, these pulses cannot be created in real electronic circuits, and different solutions must be adopted. Thus, it is possible to find in literature many examples of OTFS modulation based on rectangular pulses [62, 46], whose CAF spreads in frequency, according to Fig. 1.6, but it easier to handle (mathematically speaking) within the derivation of the OTFS input-output relation. An in-depth numerical analysis comparing the performance of OTFS with different pulses (rectangular, root-raised cosine, Gaussian) has been carried on, resulting in similar performance, and thus not shown here for the sake of brevity. This fact has been also confirmed in [61]. Thus, we took advantage of the simplicity in terms of mathematical treating of rectangular pulses, as generally done in literature, by keeping in mind that a different treatment is possible, but does not lead to remarkable performance improvement, at least in the considered scenarios.

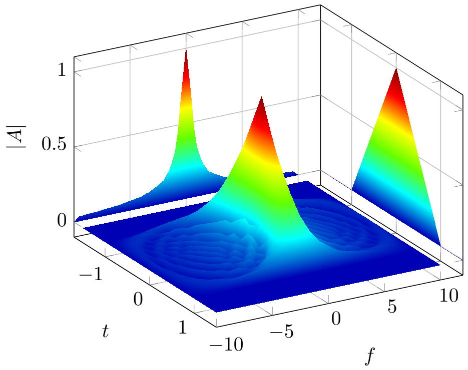

(a) Rectangular pulses, $g_{\mathrm{tx}}(t) = g_{\mathrm{rx}}(t)$.

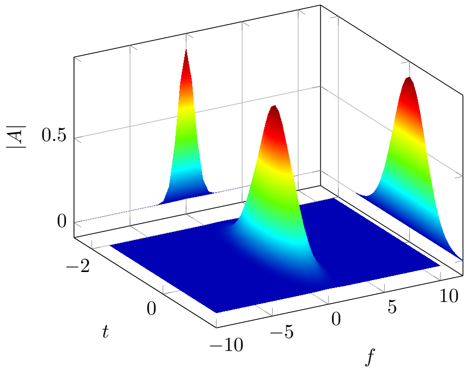

(b) Gaussian pulses, σ_1^2, $g_{\mathrm{tx}}(t) = g_{\mathrm{rx}}(t)$.

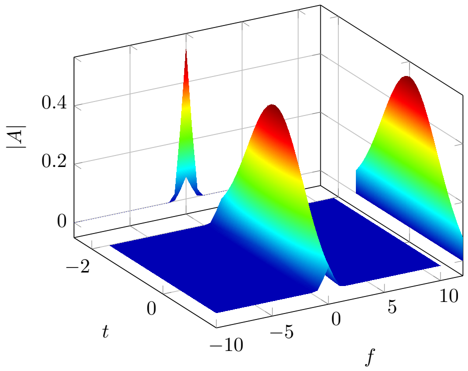

(c) Gaussian pulses, $\sigma_2^2 > \sigma_1^2$, $g_{\mathrm{tx}}(t) \neq g_{\mathrm{rx}}(t)$.

Figure 1.6: Cross-ambiguity function for different pulses.

Chapter 2

ML Methods for Radar Parameter Estimation

2.1 Joint State Sensing and Communication

2.1.1 OFDM

2.1.1.1 Maximum Likelihood Estimator

Starting from the aforementioned analysis, by focusing for simplicity on a single-target case ($P = 1$), we neglect the p-path subscript for the following derivations based on OFDM. Since data symbols are known by the radar Rx (which could be colocated with the Tx (monostatic radar) or not (bistatic radar)), and the noise is i.i.d. Gaussian circularly symmetric, the radar Rx can shift the data symbol phase without changing the noise statistics. Therefore, the radar observation, including the noise and symbol-by-symbol phase rotation, can be written as

$$z_{n,m} = A_{n,m} h e^{j2\pi n T_o \nu} e^{-j2\pi m \Delta f \tau} + w_{n,m} \,, \tag{2.1}$$

where $A_{n,m} = |x_{n,m}|$ denotes the amplitude of the transmitted symbol and $w_{n,m}$ is the additive white Gaussian noise (AWGN) with zero mean and unit variance.

The maximum likelihood (ML) estimator of channel gain, range, and velocity for the observation model in (2.1) is obtained by generalizing the approach in [26, Chapter 3.3.3] to the case of arbitrarily amplitude $\mathbf{A}$ symbols, with $\mathbf{A}$ being the matrix collecting the time-frequency entries $\{A_{n,m}\}$. For the set of parameters $\boldsymbol{\theta} = (h, \nu, \tau)$, we wish to find the estimator minimizing the likelihood function

$$l(\mathbf{z}|\boldsymbol{\theta}, \mathbf{A}) = \sum_n \sum_m \left| z_{n,m} - h A_{n,m} e^{j2\pi(\nu n T_o - m\Delta f \tau)} \right|^2 . \tag{2.2}$$

Assuming that the pair (ν, τ) is known, by letting the derivative of $l(\mathbf{z}|\boldsymbol{\theta}, \mathbf{A})$ w.r.t. h equal to zero, we obtain the estimation $\hat{h}$ of the complex channel gain h, which is

$$\hat{h} = \frac{Z(\nu, \tau)}{\sum_{n,m} A_{n,m}^2} , \tag{2.3}$$

where the DFT/inverse discrete Fourier transform (IDFT) operation is defined as

$$Z(\nu, \tau) \triangleq \sum_{m=0}^{M-1} \sum_{n=0}^{N-1} z_{n,m} A_{n,m} e^{-j2\pi\nu n T_o} e^{j2\pi m \Delta f \tau} , \tag{2.4}$$

which is a two-dimensional periodogram. By plugging (2.3) into (2.2) and following similar steps as [13, Chapter 7.2.2]), the estimator of the remaining unknown parameters in given by

$$(\hat{\nu}, \hat{\tau}) = \arg \max_{(\nu,\tau) \in \Gamma'} |Z(\nu, \tau)|^2 , \tag{2.5}$$

where we considered a discretized set Γ' of delay and Doppler frequency axes with step sizes $1/\left(M'\Delta f\right)$ and $1/\left(N' T_\text{o}\right)$, respectively, with $N' \geq N$ and $M' \geq M$. Note that Γ' is in line with the definition in (1.13), but with greater granularity to achieve an higher accuracy within the estimation process.

In summary, to compute the joint ML estimator of the set of unknown parameters (h, τ, ν) the following steps are done:

1. Compute the DFT/IDFT output $Z(\nu,\tau)$. This step which can be efficiently implemented by using fast Fourier transform (FFT)-based design.
2. Choose $(\hat{\nu},\hat{\tau})$ maximizing $|Z(\nu,\tau)|^2$ over Γ', for some N' and M' (depending to the target accuracy level).
3. Let the channel gain be $\hat{h} = Z(\hat{\nu},\hat{\tau})/\left(\sum_{n,m} A_{n,m}^2\right)$.

Clearly, starting from the delay and Doppler estimations, it is possible to derive the corresponding range and velocity estimations, respectively given by $\hat{r} = \hat{\tau}c/2$ and $\hat{v} = \hat{\nu}c/(2f_c)$.

2.1.1.2 Crameŕ-Rao lower bound (CRLB)

It is well known that the Crameŕ-Rao lower bound (CRLB) provides a theoretical lower bound on the variance of any estimator [3, 34]. The derivation of the CRLB depends on the particular system setting, but it is always based on a common denominator, i.e., the construction of the Fisher information matrix.

Suppose we have only one path, i.e., $P = 1$, to simplify the notation. For the calculation of the CRLB consider a vector of unknown parameters $\boldsymbol{\theta}$ to be estimated. Given $f\left(\mathbf{y}|\boldsymbol{\theta}\right)$, which is the conditional distribution of the channel output $\mathbf{y}$ given the set of unknown parameters $\boldsymbol{\theta}$, if the regularity condition is satisfied

$$\mathbb{E}_{\mathbf{y}}\left[\frac{\partial}{\partial\boldsymbol{\theta}}\ln f\left(\mathbf{y}|\boldsymbol{\theta}\right)\right] = \begin{bmatrix} \mathbb{E}_{\mathbf{y}}\left[\frac{\partial}{\partial h}\ln f\left(\mathbf{y}|\boldsymbol{\theta}\right)\right] \\ \mathbb{E}_{\mathbf{y}}\left[\frac{\partial}{\partial \tau}\ln f\left(\mathbf{y}|\boldsymbol{\theta}\right)\right] \\ \mathbb{E}_{\mathbf{y}}\left[\frac{\partial}{\partial \nu}\ln f\left(\mathbf{y}|\boldsymbol{\theta}\right)\right] \end{bmatrix} = \begin{bmatrix} 0 \\ 0 \\ 0 \end{bmatrix}, \tag{2.6}$$

then, any unbiased estimator providing $\hat{\boldsymbol{\theta}}$ has covariance matrix

$$\boldsymbol{C}_{\hat{\boldsymbol{\theta}}} = \mathbb{E}\left[\left(\hat{\boldsymbol{\theta}} - \mathbb{E}\left[\hat{\boldsymbol{\theta}}\right]\right)\left(\hat{\boldsymbol{\theta}} - \mathbb{E}\left[\hat{\boldsymbol{\theta}}\right]\right)^*\right], \tag{2.7}$$

which satisfies

$$\left(\boldsymbol{C}_{\hat{\boldsymbol{\theta}}} - \mathbf{I}\left(\boldsymbol{\theta}\right)^{-1}\right) \geq 0 \quad \forall\boldsymbol{\theta}\,. \tag{2.8}$$

The matrix $\mathbf{I}(\boldsymbol{\theta})$ is the Fisher information matrix, whose (i,j) element is

$$[\mathbf{I}(\boldsymbol{\theta})]_{i,j} = -\mathbb{E}_{\mathbf{y}}\left[\frac{\partial^2 \ln f(\mathbf{y}|\boldsymbol{\theta})}{\partial\theta_i \partial\theta_j}\right], \tag{2.9}$$

where indexes (i,j) select the unknown parameters within the vector $\boldsymbol{\theta}$. Moreover, (2.8) implies that diagonal elements of $\boldsymbol{C}_{\boldsymbol{\theta}}$ dominates those of $\mathbf{I}(\boldsymbol{\theta})^{-1}$, hence

$$\mathrm{Var}\left[\hat{\theta}_i\right] \geq \left[\mathbf{I}(\boldsymbol{\theta})^{-1}\right]_{ii} \geq \frac{1}{[\mathbf{I}(\boldsymbol{\theta})]_{ii}}. \tag{2.10}$$

Consider the vector of unknown parameters $\boldsymbol{\theta} = (\alpha, \varphi, f, \mathsf{t})$, where $\alpha = |h|$, $\varphi = \angle(h)$, $f = T_o\nu$, and $\mathsf{t} = \Delta f \tau$, from (2.1) we obtain

$$z_{n,m} = A_{n,m}\alpha e^{j\varphi} e^{j2\pi n f} e^{-j2\pi m \mathsf{t}} + w_{n,m}. \tag{2.11}$$

By letting $s_{n,m} = A_{n,m}\alpha e^{j\varphi} e^{j2\pi n f} e^{-j2\pi m \mathsf{t}}$, we derive the 4×4 Fisher information matrix defined as

$$[\mathbf{I}(\boldsymbol{\theta}, \mathbf{A})]_{i,j} = 2P_{\mathrm{avg}}\mathrm{Re}\left\{\sum_{n,m}\left[\frac{\partial s_{n,m}}{\partial\theta_i}\right]^*\left[\frac{\partial s_{n,m}}{\partial\theta_j}\right]\right\}, \tag{2.12}$$

where P_{avg} takes into account any possible power constraint on transmitted symbols. We thus have

$$\frac{\partial s_{n,m}}{\partial\alpha} = A_{n,m}e^{j\varphi}e^{+j2\pi n f}e^{-j2\pi m \mathsf{t}} \tag{2.13a}$$

$$\frac{\partial s_{n,m}}{\partial\varphi} = j\alpha A_{n,m}e^{j\varphi}e^{+j2\pi n f}e^{-j2\pi m \mathsf{t}} \tag{2.13b}$$

$$\frac{\partial s_{n,m}}{\partial f} = (j2\pi n)\alpha A_{n,m}e^{j\varphi}e^{+j2\pi n f}e^{-j2\pi m \mathsf{t}} \tag{2.13c}$$

$$\frac{\partial s_{n,m}}{\partial \mathsf{t}} = (-j2\pi m)\alpha A_{n,m}e^{j\varphi}e^{+j2\pi n f}e^{-j2\pi m \mathsf{t}}. \tag{2.13d}$$

For a model given in (2.11), the MMSE of f and t is lower bounded by

$$\sigma^2_{\hat{\mathrm{f}}} \geq \frac{N_0}{2|h|^2}\frac{e_{\mathrm{f}}(\mathbf{A})}{d(\mathbf{A})} \tag{2.14a}$$

$$\sigma^2_{\hat{\mathsf{t}}} \geq \frac{N_0}{2|h|^2}\frac{e_{\mathsf{t}}(\mathbf{A})}{d(\mathbf{A})}, \tag{2.14b}$$

where $e_{\text{f}}(\mathbf{A}), e_{\text{t}}(\mathbf{A}), d(\mathbf{A})$ are given by

$$e_{\text{f}}(\mathbf{A}) = (2\pi)^2 \left\{ \sum_{n,m} (A^2_{n,m}) \cdot \sum_{n,m} (m^2 A^2_{n,m}) - \Big[\sum_{n,m} m A^2_{n,m} \Big]^2 \right\}, \tag{2.15a}$$

$$e_{\text{t}}(\mathbf{A}) = (2\pi)^2 \left\{ \sum_{n,m} (A^2_{n,m}) \cdot \sum_{n,m} (n^2 A^2_{n,m}) - \Big[\sum_{n,m} n A^2_{n,m} \Big]^2 \right\}, \tag{2.15b}$$

$$\begin{aligned} d(\mathbf{A}) = (2\pi)^4 \Big\{ & \sum_{n,m} (A^2_{n,m}) \Big[\sum_{n,m} n^2 A^2_{n,m} \Big] \Big[\sum_{n,m} m^2 A^2_{n,m} \Big] \\ & + 2 \Big[\sum_{n,m} n A^2_{n,m} \Big] \Big[\sum_{n,m} m A^2_{n,m} \Big] \Big[\sum_{n,m} nm A^2_{n,m} \Big] - \sum_{n,m} (A^2_{n,m}) \Big[\sum_{n,m} nm A^2_{n,m} \Big]^2 \\ & - \Big[\sum_{n,m} n^2 A^2_{n,m} \Big] \Big[\sum_{n,m} m A^2_{n,m} \Big]^2 - \Big[\sum_{n,m} m^2 A^2_{n,m} \Big] \Big[\sum_{n,m} n A^2_{n,m} \Big]^2 \Big\}. \end{aligned} \tag{2.15c}$$

In the regime of large M and N, the CRLB of f and $\mathtt{t}$ are given by

$$\sigma^2_{\hat{\text{f}}} \geq \frac{6}{|h|^2 P_{\text{avg}} (2\pi)^2 MN(N^2-1)}, \tag{2.16a}$$

$$\sigma^2_{\hat{\text{t}}} \geq \frac{6}{|h|^2 P_{\text{avg}} (2\pi)^2 MN(M^2-1)}. \tag{2.16b}$$

For a special case of constant envelope ($A_{n,m} = \sqrt{P_{\text{avg}}}$ for all n, m), the above expressions coincide with those in [26, Section 3.3].

2.1.2 OTFS

2.1.2.1 Maximum Likelihood Estimator

Based of the results of Chapter 1 and Sec. 1.3.1, the vectorized input-output relation is

$$\mathbf{y} = \sum_{p=0}^{P-1} h_p \mathbf{\Psi}^p(\tau_p, \nu_p)\mathbf{x} + \mathbf{w}. \tag{2.17}$$

We wish to estimate the set of unknown parameters $\boldsymbol{\theta} = (\bar{\mathbf{h}}, \bar{\boldsymbol{\tau}}, \bar{\boldsymbol{\nu}})$, with $\bar{\mathbf{h}} = [h_0, \ldots, h_{P-1}]$, $\bar{\boldsymbol{\tau}} = [\tau_0, \ldots, \tau_{P-1}]$, and $\bar{\boldsymbol{\nu}} = [\nu_0, \ldots, \nu_{P-1}]$, where the bar indicates the true channel parameter value.

Let us first focus on the single path case (i.e., getting rid of subscript 0 after the following equation) while deriving the ML solution for parameter estimation; the multiple path case will be discussed afterwords. The likelihood function to maximize w.r.t. $\boldsymbol{\theta}$ is given by

$$l(\mathbf{y}|\theta,\mathbf{x}) = \exp\left(-|\mathbf{y} - h_0\mathbf{\Psi}^0(\tau_0,\nu_0)\mathbf{x}|^2\right) , \tag{2.18}$$

or, equivalently, applying the logarithm, we minimize the following

$$\begin{aligned} l(\mathbf{y}|\theta,\mathbf{x}) &= |\mathbf{y} - h\mathbf{\Psi}(\tau,\nu)\mathbf{x}|^2 = (\mathbf{y} - h\mathbf{\Psi}(\tau,\nu)\mathbf{x})(\mathbf{y} - h\mathbf{\Psi}(\tau,\nu)\mathbf{x})^* \\ &= |\mathbf{y}|^2 - 2\mathrm{Re}\{h\mathbf{y}^{\mathsf{H}}\mathbf{\Psi}(\tau,\nu)\mathbf{x}\} + |h|^2\mathbf{x}^{\mathsf{H}}\mathbf{\Psi}^{\mathsf{H}}\mathbf{\Psi}\mathbf{x} , \end{aligned} \tag{2.19}$$

where symbols $\boldsymbol{x}$ are known at the radar Rx, which could be colocated with the Tx (monostatic radar) or not (bistatic radar), but shares the information about transmitted symbols. Therefore, these symbols are treated as known (in the conditioning of the likelihood function), and not as nuisance as for classical estimators (for timing, frequency, etc.), and the receiver performs coherent processing. Assuming that the pair (τ,ν) is completely known, the aim is to minimize $l(\mathbf{y}|\theta,\mathbf{x})$ w.r.t. the real part h_R of h (and then the imaginary)

$$\frac{\partial l}{\partial h_R} = -\mathbf{\Psi}(\tau,\nu)\mathbf{x}(\mathbf{y} - h\mathbf{\Psi}(\tau,\nu)\mathbf{x})^* - (\mathbf{y} - h\mathbf{\Psi}(\tau,\nu)\mathbf{x})(\mathbf{\Psi}(\tau,\nu)\mathbf{x})^* . \tag{2.20}$$

By letting $\partial l/\partial h_R = 0$, we obtain

$$\hat{h}_R = \frac{\mathrm{Re}\{\mathbf{x}^{\mathsf{H}}\mathbf{\Psi}^{\mathsf{H}}\mathbf{y}\}}{\mathbf{x}^{\mathsf{H}}\mathbf{\Psi}^{\mathsf{H}}\mathbf{\Psi}\mathbf{x}} , \tag{2.21}$$

where the hat $(\hat{\cdot})$ indicates an estimate of the parameter, and, combining with $\partial l/\partial h_I = 0$, we get

$$\hat{h} = \frac{\mathbf{x}^{\mathsf{H}}\mathbf{\Psi}^{\mathsf{H}}\mathbf{y}}{\mathbf{x}^{\mathsf{H}}\mathbf{\Psi}^{\mathsf{H}}\mathbf{\Psi}\mathbf{x}} . \tag{2.22}$$

At this point, by using $\hat{h}$, it is possible to estimate (τ,ν) based on the updated likelihood function

$$\begin{aligned} l(\mathbf{y}|\theta,\mathbf{x}) &= (\mathbf{y}-\hat{h}\boldsymbol{\Psi}(\tau,\nu)\mathbf{x})^{\mathsf{H}}(\mathbf{y}-\hat{h}\boldsymbol{\Psi}(\tau,\nu)\mathbf{x}) \\ &= |\mathbf{y}|^2 - \hat{h}\mathbf{y}^{\mathsf{H}}\boldsymbol{\Psi}(\tau,\nu)\mathbf{x} - \hat{h}^*\mathbf{x}^{\mathsf{H}}\boldsymbol{\Psi}^{\mathsf{H}}\mathbf{y} + |\hat{h}|^2\mathbf{x}^{\mathsf{H}}\boldsymbol{\Psi}^{\mathsf{H}}\boldsymbol{\Psi}\mathbf{x} \\ &= |\mathbf{y}|^2 - |\hat{h}|^2\mathbf{x}^{\mathsf{H}}\boldsymbol{\Psi}^{\mathsf{H}}\boldsymbol{\Psi}\mathbf{x} \\ &= |\mathbf{y}|^2 - \frac{|\mathbf{x}^{\mathsf{H}}\boldsymbol{\Psi}^{\mathsf{H}}\mathbf{y}|^2}{\mathbf{x}^{\mathsf{H}}\boldsymbol{\Psi}^{\mathsf{H}}\boldsymbol{\Psi}\mathbf{x}}\,. \end{aligned} \tag{2.23}$$

By ignoring the first term which is constant and irrelevant in any detection/estimation scheme, it is clear that $l(\mathbf{y}|\theta,\mathbf{x})$ is minimized by maximizing the second term. Namely, we have

$$(\hat{\tau},\hat{\nu}) = \arg\max_{(\tau,\nu)} \frac{|\mathbf{x}^{\mathsf{H}}\boldsymbol{\Psi}^{\mathsf{H}}(\tau,\nu)\mathbf{y}|^2}{\mathbf{x}^{\mathsf{H}}\boldsymbol{\Psi}(\tau,\nu)^{\mathsf{H}}\boldsymbol{\Psi}(\tau,\nu)\mathbf{x}}\,. \tag{2.24}$$

Given the fact that the search for parameter $(\tau,\nu)\in\mathbb{R}\times\mathbb{R}$ maximizing the likelihood function is an extremely complex problem, whose solution might be very difficult to find since there are no constraints on the variables (simply belonging to $\mathbb{R}$), practically, as for OFDM, we consider a discretized set Γ' of delay and Doppler axes, based on Γ in (1.13), i.e.,

$$\Gamma' = \left\{\left(\frac{n}{M'\Delta f}, \frac{m}{N'T}\right)\right\}, \tag{2.25}$$

for $n = 0,\dots,N'-1$ and $m = 0,\dots,M'-1$, where $N' \geq N$ and $M' \geq M$. Thus, the estimation is performed over this set

$$(\hat{\tau},\hat{\nu}) = \arg\max_{(\tau,\nu)\in\Gamma'} \frac{|\mathbf{x}^{\mathsf{H}}\boldsymbol{\Psi}^{\mathsf{H}}(\tau,\nu)\mathbf{y}|^2}{\mathbf{x}^{\mathsf{H}}\boldsymbol{\Psi}(\tau,\nu)^{\mathsf{H}}\boldsymbol{\Psi}(\tau,\nu)\mathbf{x}}\,. \tag{2.26}$$

Clearly, the finer the granularity of the set Γ', the better the estimation performance, at the cost of an increased computational complexity. Moreover, in order to keep the maximization computationally feasible, one can first use a coarse Γ', and then refine the estimation by successively increase the granularity of Γ' and search only around the previously estimated values.

After having found the ML solution for the single path case, we now consider multiple paths. The aim is to find the ML estimator for the set of $3P$

unknown parameters $\boldsymbol{\theta} = (\bar{\mathbf{h}}, \bar{\boldsymbol{\tau}}, \bar{\boldsymbol{\nu}})$. In this case, the log-likelihood function to be minimized is given by

$$l\left(\boldsymbol{y}|\boldsymbol{\theta},\boldsymbol{x}\right) = \left|\boldsymbol{y} - \sum_{p=0}^{P-1} h'_p \boldsymbol{\Psi}_p \boldsymbol{x}\right|^2 , \tag{2.27}$$

for which, as before, symbols $\boldsymbol{x}$ are known at the radar detector. The ML estimator is thus given by

$$\hat{\boldsymbol{\theta}} = \arg \min_{\boldsymbol{\theta}\in\mathbb{C}^P\times\mathbb{R}^P\times\mathbb{R}^P} l\left(\boldsymbol{y}|\boldsymbol{\theta},\boldsymbol{x}\right) . \tag{2.28}$$

A brute-force search for the maximum in a $3P$-dimensional continuous domain is generally unfeasible. Thus, a viable method approximating the ML solution with low complexity is presented in the following.

The log-likelihood function in (2.27) is quadratic in the complex amplitudes (h'_p) for given (τ_p, ν_p). Hence, the minimization of (2.27) w.r.t. (h'_p) for fixed (τ_p, ν_p) is readily given as the solution of the linear system of equations

$$\sum_{q=0}^{P-1} h'_q \boldsymbol{x}^{\mathsf{H}} \boldsymbol{\Psi}_p^{\mathsf{H}} \boldsymbol{\Psi}_q \boldsymbol{x} = \boldsymbol{x}^{\mathsf{H}} \boldsymbol{\Psi}_p^{\mathsf{H}} \boldsymbol{y} \, , \tag{2.29}$$

for $p = 0, \ldots, P-1$. Expanding (2.27) and using the equality (2.29), after some long but relatively simple algebra, mostly including derivatives (as for the single path case), not given explicitly for the sake of brevity, the minimization w.r.t. (τ_p, ν_p) reduces to maximizing the function

$$l_2(\boldsymbol{y}|\boldsymbol{\theta},\boldsymbol{x}) = \sum_{p=0}^{P-1} \left\{ \overbrace{\frac{|\boldsymbol{x}^{\mathsf{H}} \boldsymbol{\Psi}_p^{\mathsf{H}} \boldsymbol{y}|^2}{\boldsymbol{x}^{\mathsf{H}} \boldsymbol{\Psi}_p^{\mathsf{H}} \boldsymbol{\Psi}_p \boldsymbol{x}}}^{S_p(\tau_p,\nu_p)} - \underbrace{\frac{\left(\sum_{q\neq p} h'_q \boldsymbol{x}^{\mathsf{H}} \boldsymbol{\Psi}_p^{\mathsf{H}} \boldsymbol{\Psi}_q \boldsymbol{x}\right) \boldsymbol{y}^{\mathsf{H}} \boldsymbol{\Psi}_p \boldsymbol{x}}{\boldsymbol{x}^{\mathsf{H}} \boldsymbol{\Psi}_p^{\mathsf{H}} \boldsymbol{\Psi}_p \boldsymbol{x}}}_{I_p\left(\{h'_q\}_{q\neq p},\boldsymbol{\tau},\boldsymbol{\nu}\right)} \right\} , \tag{2.30}$$

where $S_p(\tau_p, \nu_p)$ and $I_p\left(\{h'_q\}_{q\neq p}, \boldsymbol{\tau}, \boldsymbol{\nu}\right)$ denote the useful signal and the interference term for path p, respectively. Clearly, since the channel coefficients (h'_p) are unknown, it is impossible to directly maximize $l_2\left(\boldsymbol{y}|\boldsymbol{\theta},\boldsymbol{x}\right)$ w.r.t. (τ_p, ν_p), as the interference term cannot be computed. Furthermore, even for known coefficients (h'_p), the function $l_2\left(\boldsymbol{y}|\boldsymbol{\theta},\boldsymbol{x}\right)$ is not separable in the pairs of parameters (τ_p,ν_p) for different values of p because of the dependency of the interference terms I_p on all (τ_q,ν_q) for $q \neq p$. Nevertheless, this dependency appears through the "cross-term" coefficients of the type $\boldsymbol{x}^{\mathsf{H}}\boldsymbol{\Psi}_p^{\mathsf{H}}\boldsymbol{\Psi}_q\boldsymbol{x}$, which tend to be weak for typically sparse multipath channels. Therefore, we resort to an iterative block-wise estimation method, described in Algorithm 1, that alternates the optimization of each pair (τ_p,ν_p) by keeping fixed the other parameter pairs and the channel complex coefficients and, after a round of updates for the delay and Doppler parameters, it re-evaluates the estimates of the channel coefficients by solving (2.29).

Algorithm 1: *Multipath Parameters Estimation*

```
Result: The set $(\hat{h}'_p, \hat{\tau}_p, \hat{\nu}_p)$, for $p = 0, \dots, P-1$.
It: Let $i = 0, 1, 2, \dots$ be the iteration number;
Initialization: For $i = 0$, initialize $\hat{h}'_p[0] = 0$;
for $i = 1, 2, \dots$ do
    • Delay and Doppler update: For each $p = 1, \dots, |\mathcal{P}|$, find the
      estimates $\hat{\tau}_p[i], \hat{\nu}_p[i]$ by solving the two-dimensional maximization
          $(\hat{\tau}_p[i], \hat{\nu}_p[i]) = \arg\max_{(\tau,\nu)} \left\{ S_p - I_p \right\},$   (2.31)
      with $S_p$ and $I_p$ calculated for $(\hat{h}'_p[i], \tau, \nu, \hat{\phi}_p[i])$;
    • Complex channel coefficients update: Solve the linear
      system (5.34) with channel matrices $\boldsymbol{\Psi}_p$ with parameters
      $(\hat{h}'_p[i], \hat{\tau}_p[i], \hat{\nu}_p[i]$, and let the solution be denoted by $\hat{h}'_p[i]$.
end
```

Algorithm 1 describes the steps and the iterative process necessary to obtain the estimation of all channel parameters. The iteration stops when the values of $(\hat{\tau}_p[n^{\text{it}}], \hat{\nu}_p[n^{\text{it}}])$ do not show a significant change w.r.t. the previous iteration, or if a maximum number of iterations is reached. In practice, we find the maximizer in (2.30) first by searching on the “integer” Doppler-delay grid Γ of (1.13), for which the channel matrices can be pre-computed and stored (drastically reducing the computational complexity), then by searching on a finely discretized grid Γ' on the delay and Doppler domains, around the rough estimated value of the first phase (as described after (2.26)). This multiple-step maximization search allows to reduce the overall computational complexity, allowing to adopt the proposed algorithm even with increasing block dimensions NM (up to a certain limit). Furthermore, in all our simulations we noticed that the algorithm converges in just a few iterations (2 to 5, at most). Note that the case $P = 1$, which corresponds to the presence of the term $S_0(\tau_0, \nu_0)$ only, i.e., with no interfering terms I_p, is a straightforward particular case of Algorithm 1, and results to be the adaptive matched filter introduced in [63].

2.1.2.2 Cramér-Rao Lower Bound (CRLB)

By starting from the general consideration about the CRLB done for OFDM, the derivation of the CRLB for OTFS is based on the channel matrix expression in (1.44). By letting

$$s_p[k,l] = \left|h'_p\right| e^{j\angle h'_p} \sum_{k'=0}^{N-1} \sum_{l'=0}^{M-1} \mathbf{\Psi}^p_{k,k'} \left[l, l'\right] x_{k',l} \,, \tag{2.32}$$

and considering separately the amplitude and the phase of the complex channel coefficients (h'_p), the (i, j) element of the $4P \times 4P$ Fisher information matrix is given by

$$[\mathbf{I}(\boldsymbol{\theta}, \boldsymbol{x})]_{i,j} = \frac{2P_{\text{avg}}}{\sigma_w^2} \text{Re} \left\{ \sum_{n,m} \left[\frac{\partial s_p[n,m]}{\partial \theta_i} \right]^* \frac{\partial s_p[n,m]}{\partial \theta_j} \right\}, \tag{2.33}$$

in which $\boldsymbol{\theta} = \left(\left|\boldsymbol{h}'\right|, \angle \boldsymbol{h}', \boldsymbol{\tau}, \boldsymbol{\nu}\right)$ is the set of $4P$ channel unknown parameters.

The partial derivatives w.r.t. the magnitude and phase of h'_p are straightforward and are omitted for the sake of brevity. The derivatives w.r.t. τ_p and w.r.t. ν_p are more cumbersome and, after some algebra, can be obtained as

$$\begin{aligned} \frac{\partial \boldsymbol{\Psi}_{k,k'}\left[l,l'\right]}{\partial \tau_p} =& \frac{1}{NM}\sum_{n,m} e^{j2\pi(\nu_p NT-k+k')\frac{n}{N}} e^{j2\pi(l-l'-\tau_p M\Delta f)\frac{m}{M}}\left(j2\pi m\Delta f\right) \\ & e^{j2\pi\nu_p\left(\frac{l'}{M\Delta f}\right)} \times \begin{cases} 1 & \text{if } l' \in \mathcal{L}_{\text{ICI}} \\ e^{-j2\pi\left(\frac{k'}{N}+\nu_p T\right)} & \text{if } l' \in \mathcal{L}_{\text{ISI}} \end{cases}, \end{aligned} \tag{2.34}$$

for the delay, and

$$\begin{aligned} \frac{\partial \boldsymbol{\Psi}_{k,k'}\left[l,l'\right]}{\partial \nu_p} =& \frac{j2\pi}{NM}\sum_{m} e^{j2\pi(l-l'-\tau_p M\Delta f)\frac{m}{M}} e^{j2\pi\nu_p\left(\frac{l'}{M\Delta f}\right)} \\ \times & \begin{cases} \sum_n e^{j2\pi(\nu_p NT-k+k')\frac{n}{N}}\frac{l'}{M\Delta f} + \sum_n nTe^{j2\pi(\nu_p NT-k+k')\frac{n}{N}} & \text{if } l' \in \mathcal{L}_{\text{ICI}} \\ e^{-j2\pi\left(\frac{k'}{N}+\nu_p T\right)}\Big[\sum_n e^{j2\pi(\nu_p NT-k+k')\frac{n}{N}}\left(\frac{l'}{M\Delta f}-T\right) & \\ \qquad + \sum_n nTe^{j2\pi(\nu_p NT-k+k')\frac{n}{N}}\Big] & \text{if } l' \in \mathcal{L}_{\text{ISI}} \end{cases}, \end{aligned} \tag{2.35}$$

for the Doppler shift.

The desired CRLB follows by filling the Fisher information matrix in (2.33) with the derivatives computed above, and obtaining the diagonal elements of the inverse Fisher information matrix. In particular, we are interested in the CRLB for the parameters τ_0 and ν_0, related to the target range and velocity.

2.1.2.3 ML Waterfall Analysis for Single Path

It is well-known that ML estimators typically exhibit a threshold effect, i.e., a rapid deterioration of the estimation mean square error (MSE) when the signal-to-noise ratio (SNR) falls below a certain threshold (that generally depends on the problem and on the sample size). In contrast, for high SNR, i.e., larger than such threshold, the ML estimator yields MSE typically very close to the CRLB, i.e., the tightest lower bound for MSE performance. This waterfall behavior is caused by the "outliers" in the search of the maximum in any ML estimator (see, e.g., (2.28) or any aforementioned minimization or maximization based estimator in this dissertation): namely, when the noise dominates the useful signal, the maxima of the likelihood functions tend to be randomly placed anywhere on the search grid.

In the following, we analyze the waterfall effect, or transition, for the single path case $P = 1$, i.e., we search and study the region around the threshold SNR value where the rapid deterioration occurs. Moreover, simulations results show that the provided waterfall prediction for $P = 1$ is also very accurate for the multipath case $P > 1$.[1] This also confirms the evidence that the proposed approximated iterative ML estimation described in Algorithm 1 is effectively very good, and performs very close to the true ML.[2]

Following the reasoning of [64, 65], we define as “outlier” the event that a maximum of the likelihood function is randomly placed on the grid Γ, rather than within the cluster of points surrounding the true value $(\bar{\tau}_0, \bar{\nu}_0)$. Let $\alpha \in \{\tau, \nu\}$ be the unknown parameter to be estimated, i.e., τ or ν indifferently. By the law of total probability over the discretized grid Γ (where we calculate the ML estimator), we can express the estimation MSE as

$$\begin{aligned} \mathrm{MSE} = E\left[(\hat{\alpha} - \bar{\alpha})^2\right] &= \sum_{i \in \Gamma} \Pr\left(\varepsilon\left(i\right)\right) \left(\hat{\alpha}_i - \bar{\alpha}\right)^2 \\ &\le \sum_{i \in \Gamma} \Pr\left(\tilde{\varepsilon}\left(i\right)\right) \left(\hat{\alpha}_i - \bar{\alpha}\right)^2 \,. \end{aligned} \tag{2.36}$$

where $\bar{\alpha}$ is the true value of the parameter, $\hat{\alpha}$ is an estimation of such parameter, and $\Pr\left(\varepsilon\left(i\right)\right)$ denotes the probability of error of choosing α_i rather than $\bar{\alpha}$. While evaluating $\Pr\left(\varepsilon\left(i\right)\right)$ may be extremely difficult, also because the true parameter $\bar{\alpha} \in \mathbb{R}$, we obtain an upper bound by considering pairwise error probabilities, i.e., replacing $\Pr\left(\varepsilon\left(i\right)\right)$ with the probability that the detector chooses α_i rather than $\bar{\alpha}$ when these are the only two alternatives. Since the

---

[1] This is also true because the MSE performance between the single path and the multipath case are very similar.

[2] Obviously, the CRLB for $P = 1$ yields also a lower bound for the case $P > 1$, in the case where we simply add more multipath components with independent statistics, and the presence of more unknown parameters does not generally help the estimation of each single target parameters.

pairwise error event $\tilde{\varepsilon}\,(i)$ contains the true error event $\varepsilon(i)$, it follows that the inequality of (2.36) provides an upper bound.

Thus, the definition of the pairwise error probability is

$$\Pr\left(\tilde{\varepsilon}\,(i)\right) \triangleq \Pr\left\{ l\left(\boldsymbol{y}|\boldsymbol{\theta}_i, \boldsymbol{x}\right) > l\left(\boldsymbol{y}|\bar{\boldsymbol{\theta}}, \boldsymbol{x}\right) \right\}, \tag{2.37}$$

where $l\left(\boldsymbol{y}|\boldsymbol{\theta}_i, \boldsymbol{x}\right)$ and $l\left(\boldsymbol{y}|\bar{\boldsymbol{\theta}}, \boldsymbol{x}\right)$ are the values obtained from the evaluation of the likelihood function at grid point i, with parameter $\boldsymbol{\theta}_i$, and when the set of true parameters $\bar{\boldsymbol{\theta}}$ is taken into account, respectively. At this point, the problem is reduced to the computation of the pairwise error probabilities $\Pr\left(\varepsilon\,(i)\right)$, for $i \in \Gamma$, which can be derived as follows. We notice that, taking into account the useful signal appearing in (2.28)

$$\Pr\left(\tilde{\varepsilon}\,(i)\right) \approx \Pr\left\{ |\boldsymbol{x}^{\mathsf{H}} \boldsymbol{\Psi}_i^{\mathsf{H}} \boldsymbol{y}|^2 > |\boldsymbol{x}^{\mathsf{H}} \bar{\boldsymbol{\Psi}}^{\mathsf{H}} \boldsymbol{y}|^2 \right\} , \tag{2.38}$$

with $\bar{\boldsymbol{\Psi}}$ the channel matrix computed with the true set of parameters, and where we exploit $\boldsymbol{\Psi}_i^{\mathsf{H}} \boldsymbol{\Psi}_i = \boldsymbol{I}$, $\forall i$, for $P = 1$. Defining the jointly conditionally Gaussian random variables

$$\begin{aligned} z_i &\triangleq \boldsymbol{x}^{\mathsf{H}} \boldsymbol{\Psi}_i^{\mathsf{H}} \boldsymbol{y} = \boldsymbol{x}^{\mathsf{H}} \boldsymbol{\Psi}_i^{\mathsf{H}} \bar{\boldsymbol{\Psi}} \boldsymbol{x} + \boldsymbol{x}^{\mathsf{H}} \boldsymbol{\Psi}_i^{\mathsf{H}} \boldsymbol{w}\,, && (2.39)\\ \bar{z} &\triangleq \boldsymbol{x}^{\mathsf{H}} \bar{\boldsymbol{\Psi}}^{\mathsf{H}} \boldsymbol{y} = \boldsymbol{x}^{\mathsf{H}} \boldsymbol{x} + \boldsymbol{x}^{\mathsf{H}} \bar{\boldsymbol{\Psi}}^{\mathsf{H}} \boldsymbol{w}\,, && (2.40) \end{aligned}$$

with first and second order moments

$$\begin{cases} \mathrm{E}\left[\bar{z}\right] = \left\|\boldsymbol{x}\right\|^2, & \mathrm{Var}\left[\bar{z}\right] = \sigma_w^2 \left\|\boldsymbol{x}\right\|^2 \\ \mathrm{E}\left[z_i\right] = \boldsymbol{x}^{\mathsf{H}} \boldsymbol{\Psi}_i^{\mathsf{H}} \bar{\boldsymbol{\Psi}} \boldsymbol{x}, & \mathrm{Var}\left[z_i\right] = \sigma_w^2 \left\|\boldsymbol{x}\right\|^2 \end{cases}, \tag{2.41}$$

and

$$\mathrm{Cov}\left[\bar{z}, z_i\right] = \sigma_w^2 \boldsymbol{x}^{\mathsf{H}} \bar{\boldsymbol{\Psi}}^{\mathsf{H}} \boldsymbol{\Psi}_i \boldsymbol{x}\,, \tag{2.42}$$

a good approximation for $\Pr\left(\tilde{\varepsilon}\,(i)\right)$ is given by [64]

$$\Pr\left(\tilde{\varepsilon}\,(i)\right) \approx \frac{1}{2} \exp\left\{ \frac{-\left\|\boldsymbol{x}\right\|^4}{2\sigma_w^2 N M} \right\} \mathrm{I}_0\left(\frac{\left|\boldsymbol{x}^{\mathsf{H}} \boldsymbol{\Psi}_i^{\mathsf{H}} \bar{\boldsymbol{\Psi}} \boldsymbol{x}\right| \cdot \left\|\boldsymbol{x}\right\|^2}{2\sigma_w^2 N M} \right), \tag{2.43}$$

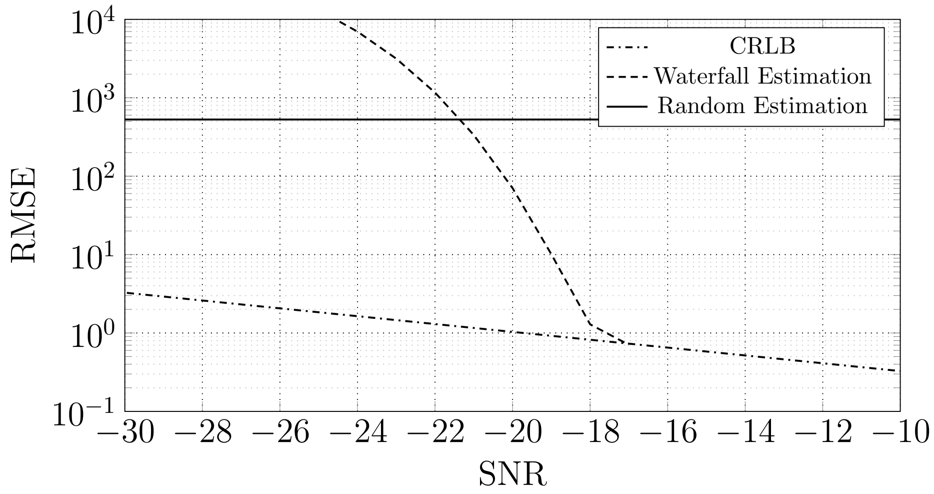

Figure 2.1: Waterfall behavior example w.r.t. other bounds.

where I_0 is the modified Bessel function of the first kind of order 0. The MSE estimation can be thus computed by substituting (2.43) into (2.36), using the above definitions.

The resulting (approximated) upper bound tends to be loose at low SNR, where the outliers are likely to occur and the associated error probabilities are high, but becomes more accurate moving towards the ML waterfall region, thus, when the outlier probability decreases. Furthermore, the MSE strictly depends on the grid resolution and may or may not reach the CRLB for increasing SNR depending on the systematic error incurred by the grid discretization. As a matter of fact, in our numerical results we took care of using a search grid fine enough such that the discretization systematic error is not visible in the explored range of SNRs, and, particularly, when the waterfall falls to the CRLB.

Moreover, to contrast the looseness of the MSE upper bound obtained in (2.36) at low SNR, we define the trivial upper bound

$$\mathrm{MSE} \leq \frac{1}{|\Gamma|} \sum_{i \in \Gamma} (\hat{\alpha}_i - \bar{\alpha})^2 \,, \tag{2.44}$$

that corresponds to estimate by choosing random grid points, i.e., completely disregarding the received signal.

Then, putting together (2.36) (with the pairwise error probability approximation in (2.43)) and the above "random estimation" bound in (2.44), we finally obtain the approximated MSE upper bound as

$$\mathrm{MSE} \lesssim \min \left\{ \sum_{i \in \Gamma} \Pr\left(\tilde{\varepsilon}\left(i\right)\right) \left(\hat{\alpha}_i - \bar{\alpha}\right)^2 , \sum_{i \in \Gamma} \frac{\left(\hat{\alpha}_i - \bar{\alpha}\right)^2}{|\Gamma|} \right\} , \tag{2.45}$$

whose behavior is shown in Fig. 2.1, together with the CRLB introduced hereafter. Thus, the ML performance of the estimator stands on the random estimation straight line for low SNR, follows the CRLB for high SNR, and the transition between these two extremes occurs around the waterfall estimation.

Simulation results show that the aforementioned analysis is able to accurately predict the waterfall behavior of the ML estimator.

2.2 Radar Resolution and Multi-Target Detection

Under the assumption of the point target model [17, 66], until now we have analyzed a single target scenario. Radar operations can be essentially performed with two different approaches. The first one, considers a radar periodically scanning angular sectors, as typical naval or airplane radars. In this context, by making the beam as directive as possible, i.e., assuming a very narrow beam and angular coverage, it is reasonable to assume the presence of just one target in any direction (or multiple targets sharing the same direction and assuming no blockage of the signal propagation). As an alternative, the second approach is based on a wider angular sector coverage. In such a case, since the target location is not *a priori* known, a joint estimation of Doppler, delay, and angle of arrival (AoA) should be performed at the radar Rx. In both approaches, the radar range and velocity resolutions acquire a central role, providing the minimum distance and velocity at which two different targets can be separately detected, i.e., such that they are not seen as a single entity.

Consider the transmitted symbols to be arranged within the Doppler-delay grid in (1.13). The definition of N, M, B (bandwidth), T, and f_c (carrier frequency) is very important. By following the continuous time signal expression in (1.17), symbols are spaced by T (seconds) in time and Δf (Hertz) in frequency. The radar resolutions are computed in the following. Starting from the definition of Doppler shift we get

$$\nu \triangleq \frac{2 v f_c}{c} \Rightarrow v \triangleq \frac{\nu c}{2 f_c}\,, \tag{2.46}$$

and since the minimum Doppler step is $\Delta f / N$, the velocity resolution results to be

$$\nu_{\text{step}} = \frac{\Delta f}{N} \Rightarrow v_{\text{res}} \triangleq \frac{\nu_{\text{step}} c}{2 N f_c} = \frac{\Delta f c}{2 N f_c}\,. \tag{2.47}$$

Equivalently, starting from the definition of delay we get

$$\tau \triangleq \frac{2r}{c} \Rightarrow r \triangleq \frac{\tau c}{2}\,, \tag{2.48}$$

and since the minimum delay step is T/M, the range resolution is

$$\tau_{\text{step}} = \frac{T}{M} \Rightarrow r_{\text{res}} \triangleq \frac{\tau_{\text{step}} c}{2M} = \frac{Tc}{2M}\,. \tag{2.49}$$

If we impose, as generally done in multi-carrier systems, the equality $\Delta f \triangleq 1/T$, together with $B = M \Delta f$, previous formulas become

$$\begin{cases} r_{\text{res}} = Tc/2 = c/(2B) \\ v_{\text{res}} = \Delta f c/(2f) = Bc/(2NMf_c) \end{cases}. \tag{2.50}$$

This analysis provides the limits of a radar system based on a multi-carrier communication waveform. Even if the range resolution strictly depends on the bandwidth B, and this is valid for any radar system, the only way to reduce the velocity resolution, having imposed $\Delta f = 1/T$, is to increase the dimension of the transmitted block of data, through N and M. However, this translates in increasing the total signal duration and decreasing the subcarriers spacing, which could lead to an increase of the computational complexity (if blockwise operations have to be computed), or increased interference effects (for instance for OFDM). This is the cost of the proposed joint radar parameter estimation and communication setup using OFDM and/or OTFS, which allows the simultaneous transmission of useful information and radar sensing without any tradeoff, but requires complex signal processing operations (to contrast the block dimension or the interference).

On the other hand, one can bypass the aforementioned problem by considering the additional spatial dimension, i.e, with a multi antenna system, such that distinct targets can be identified in three different domains: range (delay), velocity (Doppler), and angular position. As we will see, our proposed method is able to correctly detect targets which are separable in at least one domain out of three (delay, Doppler, and angle).

2.3 Simulation Results

2.3.1 Joint State Sensing and Communication

The radar (backscattered) and forward communication SNRs are defined as

$$\mathrm{SNR}_{\mathrm{rad}} = \frac{\lambda^2 \sigma_{\mathrm{rcs}} G^2}{(4\pi)^3 r^4} \frac{P_{\mathrm{avg}}}{\sigma_w^2} , \tag{2.51}$$

$$\mathrm{SNR}_{\mathrm{com}} = \frac{\lambda^2 G^2}{(4\pi)^2 r^2} \frac{P_{\mathrm{avg}}}{\sigma_w^2} , \tag{2.52}$$

respectively, where $\lambda = c/f_c$ is the wavelength, σ_{rcs} is the radar cross-section in m^2, G is the antenna gain, and r is the distance between Tx and Rx. In the case of multipath, we fix $\mathrm{SNR}_{\mathrm{com}}$ to be the SNR of the line of sight (LoS) component, and we add multipath components with progressively lower SNRs, such that the sum SNR of the channel increases with the number of paths P. This corresponds to the physically meaningful case that a richer propagation environment conveys more signal power. Table 2.1 summarizes the relevant simulation parameters inspired by the automotive communication standard

Table 2.1: Simulation parameters

$f_c = 5.89$ GHz	$M = 64$
$B = 10$ MHz	$N = 50$
$\Delta f = B/M = 156.25$ kHz	$T = 1/\Delta f = 6.4\,\mu s$
$\sigma_{\text{rcs}} = 1$ m^2	$G = 100$
$r = 20$ m	$v = 80$ km/h

IEEE 802.11p [21], where r and v denote the target range and velocity taken into account.[3]

By briefly reviewing OFDM modulation, we introduce a widely used radar waveform known as frequency modulated continuous wave (FMCW) [13, Chapter 4.6], in order to understand the gain of the proposed methods against well-known and currently used approaches for radar vehicular applications. For both OFDM and FMCW we consider a symbol length of $T_o = T_{\text{GI}} + T$, i.e., including the possible presence of a guard interval denoted by T_{GI}, generally longer than the maximum path delay $\tau_{\max}$. In OFDM the guard interval results to be the CP, extensively discussed in Sec. 1.2.

In FMCW, the radar transmitter sends a sequence of identical "chirp" pulses of duration T, each followed by a guard interval of length T_{GI} to avoid inter-pulse interference. By denoting with $\phi(t) = (f_c + \frac{B}{2T}t)t$ the phase at time t, the transmit signal is given by

$$s\left(t\right) = \sum_{i=0}^{N-1} e^{j2\pi\phi(t-iT_0)}\text{rect}\left(\frac{t-iT_0}{T}\right), \tag{2.53}$$

where N is the number of consecutive pulses. Transmitting (2.53) over the channel in (1.1), we get the received signal $r(t)$, whose expression, by neglecting

---

[3] Note that, if the conditions $\tau_{\max} < T$ and $\nu_{\max} < \Delta f$ are satisfied, the numerical results are independent of the choice of r and v.

the noise, is given in (1.20), but with the current $s(t)$. After some algebra, it is easy to show that the product of the received and the transmit signals gives

$$y(t) = r(t)s^*(t) = \sum_{p=0}^{P-1} h_p e^{j2\pi\nu_p t} e^{-j2\pi f_c \tau_p} \sum_{i=0}^{N-1} e^{-j2\pi f_{b,p}(t - iT_0 - \tau_p/2)} , \qquad (2.54)$$

where $f_{b,p} = \frac{B}{T}\tau_p$ denotes the so-called beating frequency of path p. The receiver samples $y(t)$ every T/M for each pulse, i.e., for $t = iT_o + l\frac{T}{M}$ where i denotes the pulse index and l denotes the sample index. By letting $L = M + C$ denotes the number of samples per pulse, the sampled received signal can be rewritten as

$$y[i, l] = y\left(iT_0 + \frac{l}{f_s}\right) = \sum_p h_p e^{j2\pi(f_{b,p}+\nu_p)\frac{l}{f_s}} e^{j2\pi\nu_p iT_0} , \qquad (2.55)$$

for $i = 0, \ldots, N-1$ and $l = 0, \ldots, L-1$, where h_p absorbs a constant phase term independent of the indices i, l.

The estimation of the $2P$ unknown parameters $\{\tau_p, \nu_p\}$ is thus obtained by selecting the peak of the range-Doppler map found by applying a two-dimensional DFT to the noisy samples in (2.55) as proposed in [26, 20]. The range and velocity of the target are obtained by the estimates of $\{\tau_0, \nu_0\}$.

2.3.2 Joint Radar and Communication Performance

The first two subfigures of Fig. 2.2 show the velocity and range estimation root MSE (RMSE) versus SNR_{rad} for a pure LoS channel ($P = 1$) and for OTFS, OFDM, and FMCW. We notice that both digital modulation formats provide as accurate radar performance as FMCW, while transmitting useful information to any possible Rx.

In addition, the third subfigure of Fig. 2.2 shows the achievable rate of OFDM and OTFS, for simplicity of derivation, when Gaussian independent and independent and identically distributed (i.i.d.) symbols C_{Gauss} are sent through the channel. This provides an achievable rate in the case of *joint detection and decoding*, with unconstrained complexity, as a function of SNR_{com},

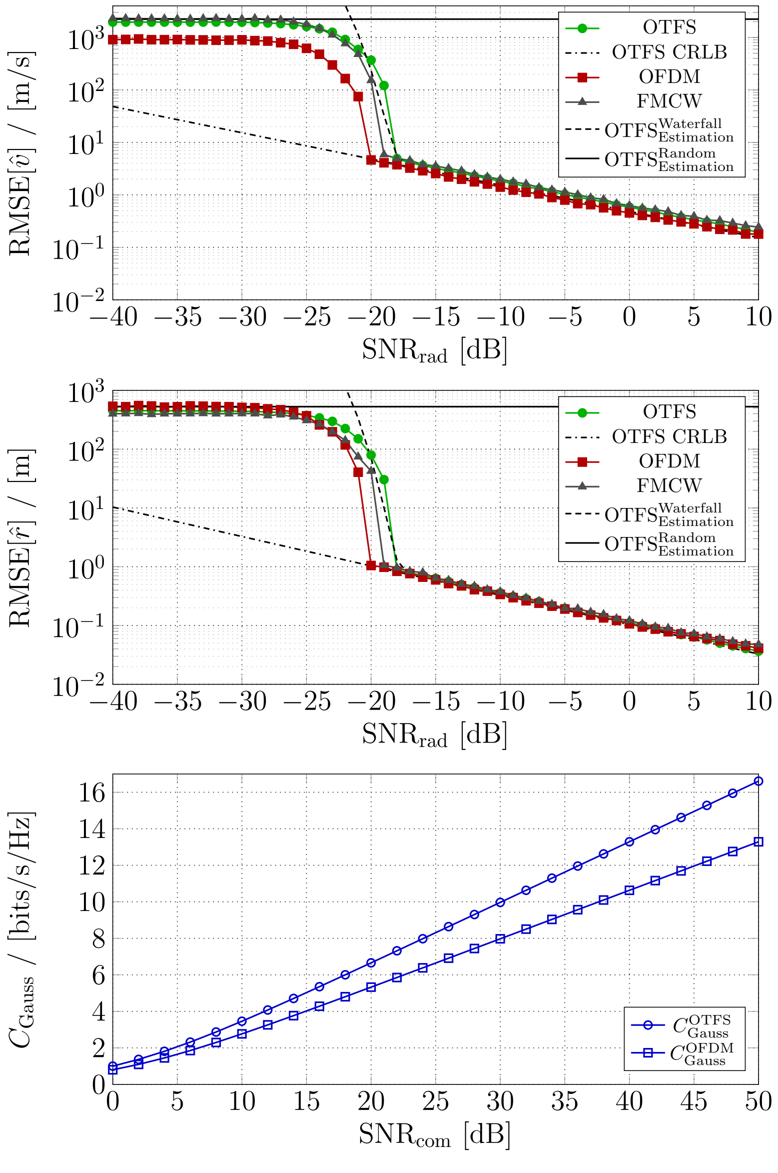

Figure 2.2: From top to bottom: the RMSE of the target velocity estimation $\hat{v}$ vs SNR$_{\text{rad}}$, the RMSE of the target range estimation $\hat{r}$ vs SNR$_{\text{rad}}$, and the Gaussian capacity $\mathcal{C}_{\text{Gauss}}$ vs. SNR$_{\text{com}}$, for the curves indicated in the different legends.

giving a qualitative idea of performance curves. A more accurate model should consider only detection, i.e., separated from decoding, calculating the achievable communication rate in terms of pragmatic capacity, as extensively done in Chapter 4.

Given the fact that we can model the block input-output relation of OTFS as a MIMO channel, the mutual information with Gaussian inputs and perfect channel state information (CSI) at the receiver is given by [67]

$$C_{\text{Gauss}}^{\text{OTFS}} = \frac{NT}{NT + T_{\text{GI}}} \frac{1}{NM} \log_2 \det \left(\boldsymbol{I} + \text{SNR}_{\text{com}} \boldsymbol{\Psi} \boldsymbol{\Psi}^H \right) . \tag{2.56}$$

A similar expression for OFDM, owing to the fact that the channel matrix in OFDM is diagonal, with consequent symbol-by-symbol detection, yields

$$C_{\text{Gauss}}^{\text{OFDM}} = \frac{T}{T + T_{\text{GI}}} \log_2 \left(1 + \text{SNR}_{\text{com}} \right) . \tag{2.57}$$

The factors $NT/(NT + T_{\text{GI}})$ and $T/(T + T_{\text{GI}})$ for OTFS and OFDM, respectively, are introduced in order to take into account the (possible) insertion of a guard interval. In OTFS, a guard interval of duration T_{GI} is inserted at the end of each frame, whose duration is $T_f^{\text{OTFS}} = NT$, comprising N consecutive symbols in the time domain (see Chapter 1). In contrast, in OFDM, the guard interval takes the form of a CP, inserted for each OFDM symbol of duration T. The frame size is thus $T_f^{\text{OFDM}} = NT_o = N(T + T_{\text{cp}})$.

It is clear that for practical values of the OTFS frame length N, the overhead paid by OTFS is much less than the CP overhead paid by OFDM (in these results we used $T_{\text{GI}} = T/4$, which is typical in the IEEE 802.11 family of standards). On the other hand, the larger overhead incurred by OFDM yields a particularly simple receiver structure, allowing symbol-by-symbol detection thanks to the diagonalization of the channel. In contrast, OTFS requires blockwise detection over the whole frame, which can be very computationally intensive, especially for large N and M. This is why the proposed soft-output symbol detector presented in Section 4.2.1 is of particular interest.

Next, we present a second set of results where we consider only OTFS but in the presence of a multipath channels ($P > 1$, up to $P = 4$), showing

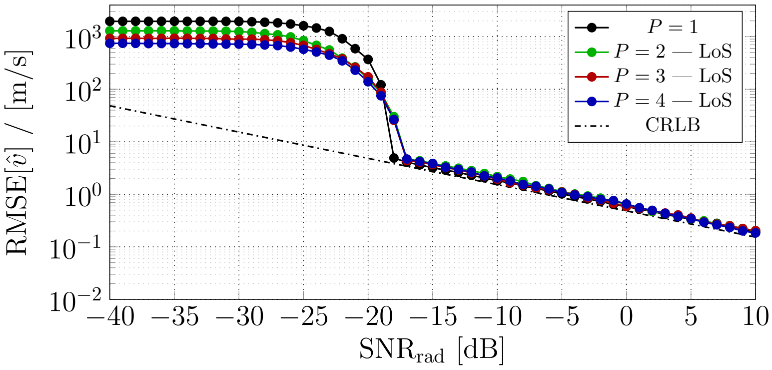

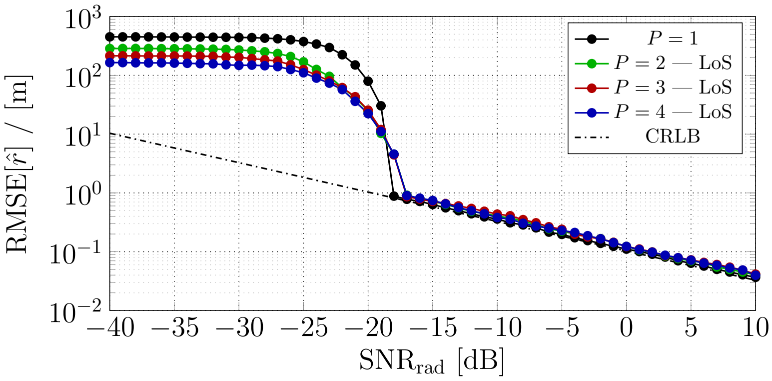

Figure 2.3: RMSE of the target velocity estimation $\hat{v}$ vs SNR$_{\text{rad}}$ and range estimation $\hat{r}$ vs SNR$_{\text{rad}}$ for a multipath channel ($P \in [1, 2, 3, 4]$).

the effectiveness of the proposed approximated ML parameter estimator in Algorithm 1 (with at most 5 iterations), under the assumption that paths are spaced enough in the Doppler-delay grid, i.e., there is no "inter-path interference", meaning that the same symbol is shifted over the received samples grid by distinct quantity (a behavioral idea comes naturally from Fig. 1.4). In our analysis, we suppose that the number of paths is known at the radar receiver, hypothesis that sums up with the knowledge of the target presence within the beam sector analyzed. In Fig. 2.3 we show the range and velocity RMSE in a multipath scenario. As expected, the performance slightly degrades as the number of paths increases, but such degradation is very mild, showing the robustness of the proposed joint parameter estimation method. Notice that the CRLB is plotted for the case $P = 1$ only, being a lower bound for the case of $P > 1$ as already said.

2.3.3 Self-Interference

In a real word scenario, the beam pattern of the antenna is not only composed by a single main lobe, but presents several side lobes, whose strength and number is generally variable. Moreover, if the waveform is continuously transmitted over time, considering a co-located radar Tx and Rx, the transmitted beam acts as interference to the backscattered signal from the target. Since this is a self-caused impairment, it is called self-interference. Typical radar systems makes use of full-duplex operations in order to eliminate, or at least mitigate, the self-interference [31, 32]. However, the cancellation could be not perfect, causing some extra noisy effects or uncertainty at the radar Rx.

By considering a possible (remaining) self-interference and a single path $P = 1$ scenario, the signal model becomes

$$\mathbf{y} = \boldsymbol{\Psi}\mathbf{x} + \mathbf{w} + \sqrt{\alpha_{\mathrm{si}}}\mathbf{x}e^{j2\pi\phi}\,, \tag{2.58}$$

where ϕ is a random unknown phase, α_{si} is the self-interference power, and $\mathbf{x}$ are the transmitted symbols. Since $\tau_{\max} < T$, each symbol acts as interference for the corresponding received sample. Figure 2.4 shows the OTFS estimation

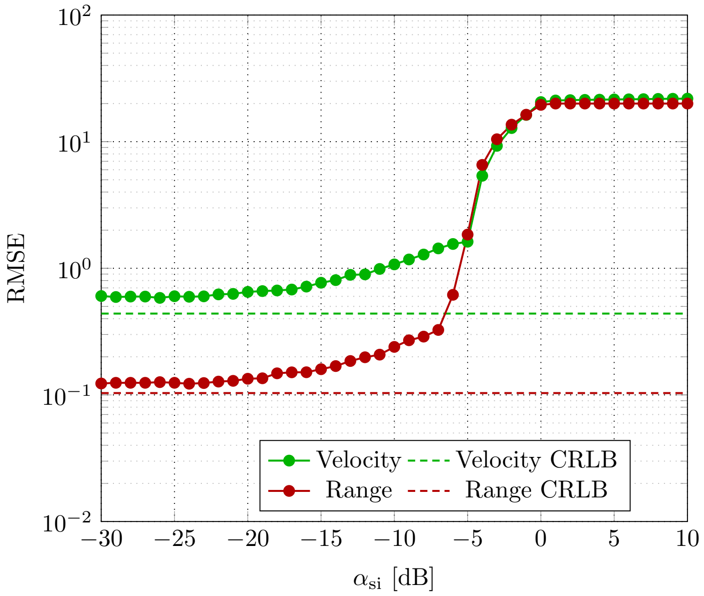

Figure 2.4: RMSE vs. Self-Interference power at SNR=10 dB.

RMSE for fixed SNR = 0 [dB], by varying the self-interference power. Note that when $\alpha_{\mathrm{si}} = 0$ [dB] the radar SNR and the self-interference power are equal. Starting from (2.58), we can equivalently write

$$\mathbf{y} = \boldsymbol{\Psi}\mathbf{x} + \mathbf{w} + \sqrt{\alpha_{\mathrm{si}}}\mathbf{x}e^{j2\pi\phi} = \left(\boldsymbol{\Psi} + \sqrt{\alpha_{\mathrm{si}}}e^{j2\pi\phi}\right)\mathbf{x} + \mathbf{w}\,. \tag{2.59}$$

The channel matrix $\boldsymbol{\Psi}$ describes the channel behavior, which is almost sparse and depends on the Dirichlet functions. The self-interference acts by filling the holes of the matrix, i.e., adding a dependency between $\mathbf{y}$ and symbols $\mathbf{x}$, independently of the channel effect. It is straightforward to understand that the filling of matrix $\boldsymbol{\Psi}$ does not act as additional noise, but has a strong destructive effect on the received samples. Note that this behavior is mostly related to the magnitude of the coefficient α_{si} rather than the random phase factor.

On the other hand, if the self-interference is modeled as the addition of random Gaussian symbols with a certain phase and power, the received samples expression becomes

$$\mathbf{y} = \boldsymbol{\Psi}\mathbf{x} + \mathbf{w} + \sqrt{\alpha_{\text{si}}}\boldsymbol{n}e^{j2\pi\phi} = \boldsymbol{\Psi}\mathbf{x} + \mathbf{w} + \sqrt{\alpha_{\text{si}}}\boldsymbol{n}\,, \tag{2.60}$$

with $\mathbf{n} \sim \mathcal{CN}\left(0, 1\right)$. In this case there is just the addition of more white noise, moving the estimation performance, together with the waterfall effect, back left on the CRLB w.r.t. Fig. 2.2. However, this model is not reliable to describe the self-interference effect.

Chapter 3

ML Radar Methods in MIMO Configurations

3.1 Introduction

The concept of MIMO radar has been extensively studied in literature in recent years and has been shown to improve the resolution, i.e., the ability to distinguish multiple targets, thanks to the additional spatial dimension (see, e.g., [49, 52]). With the possibility of boosting the transmitted power towards a chosen direction through a careful design of beamforming (BF), multiple-antenna systems are able to enhance the performance of classical single-antenna schemes, allowing the coverage of a wide spectrum of frequencies. This is particularly relevant in automotive radar systems [20] operating over millimeter wave (mmWave) frequency bands, as the high propagation loss is compensated through the antenna BF gain [68, 69]. Moreover, the radar Tx might change in time, or adapt, its BF, depending on different operating phases (see e.g., [51, 52] and references therein). Namely, the transmitted power shall be allocated to wide angular sectors during a target detection/acquisition/search phase, while narrow and distinct beams focused on a detected target, maximizing the BF gain and the received SNR, shall be used to minimize "multi-target" interference during a possible tracking and communication phase [49, 13, 70]. Clearly, within the target detection phase, a non-trivial tradeoff appears. On one hand, wider angular sectors coverage enable the detection of multiple targets if the received backscattered power is high enough. On the other hand, a more directional BF grants a higher received SNR, and thus longer detectable target distance, at the cost of a time-consuming search over narrower angular sectors (as classical radar successively swapping adjacent regions, see, e.g., [13]). Different solutions to the aforementioned problem can be found in literature (see, e.g., [52, 53, 15, 54]).

As an extension of [71] and of the concepts introduced in the previous parts, this chapter studies the joint target detection and parameter estimation problem with a mono-static MIMO radar adopting OTFS, and extends the literature results on MIMO configurations (see, e.g., [44, 72]). The use of communication waveforms for MIMO radar has been motivated by the joint radar and communication paradigm (as showed in Sec. 2.1), where two functions are implemented by sharing the same resources and the same waveform (see e.g. [24, 27, 25] and references therein). Contrary to the existing works on radar sensing using OTFS [46, 71, 28], this use case considers a MIMO radar under a practical mmWave system architecture, such that the number of radio frequency (RF) chains (N_{rf}) is much smaller than the number of antennas (N_{a}). In fact, the difficulties related to the implementation of a fully digital BF, or, equivalently, associate one RF chain per antenna (including A/D conversion, modulation, and amplification) in a small form factor and highly integrated technology over a large signal bandwidth, are well known. Therefore, focusing on mmWave automotive applications, we consider hybrid digital-analog (HDA) BF schemes as typically considered in literature (see, e.g., [55, 56] and references therein). We will study two different scenarios, exploring the aforementioned BF tradeoff. The first scenario considers a Tx BF design with beam covering a wide angular sector, to jointly perform target detection, parameter estimation, and multicasting of a common message to all possible active users (see Fig. 3.1a). A possible application of this model is, for instance, a base station mounted near a highway able to collect traffic information through radar capabilities while communicating its knowledge to active Rx.[1] Assuming the communication phase established, i.e., detection already performed, the second scenario considers a Tx BF with directed narrow beams, such that individual information streams are sent to the detected users, or groups of users, as depicted in Fig. 3.1b. It is important to stress the fact that the radar Rx uses a wide beam pattern consisting of N_{rf} beams, as illustrated in Fig. 3.2, in order to obtain a meaningful vector observation, necessary for AoA estimation, regardless of the operating phase. This is in a sharp contrast to the hybrid beam alignment considered in a typical communication system, where the Rx also applies BF and obtains a scalar observation precluding the estimation of the AoA (see, e.g., [55, 50] and references therein).

Under this setup, we propose an efficient ML-based scheme combined with HDA BF to jointly perform target detection and parameter estimation. More precisely, our scheme first performs target detection and super-resolution estimation of delay, Doppler shift, and AoA using a wide angular beam along which a single data stream is sent. Then, once the targets are detected, the subsequent tracking phase performs the parameter estimation using multiple narrow beams along which multiple data streams can be sent. Our numerical results demonstrate that the proposed scheme is able to reliably detect multiple targets while essentially achieving the CRLB for radar parameter estimation. Furthermore we investigate various scenarios of near-far effects of targets, showing that a successive interference cancellation (SIC) mechanism is able to efficiently remove the masking effect between targets located at different ranges from the radar, and we provide an in-depth analysis of the two scenarios of interest, showing their limits and advantages.

---

[1] It is clear that, getting rid of the message sent, radar tasks can be performed by using any well known radar waveform [13], and the use of a digital communication format is pointless (the transmission of information could start in a second communication phase, e.g., within a time division protocol).

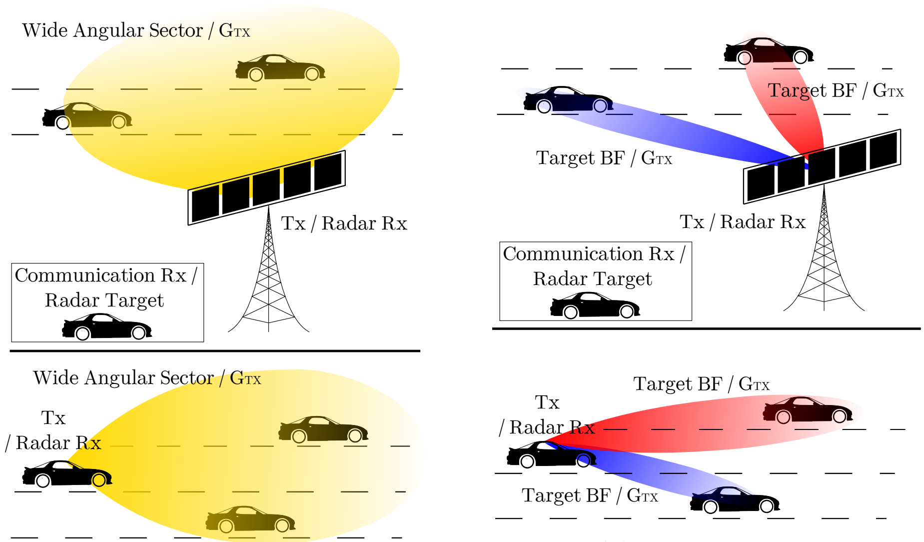

(a) Detection phase

(b) Tracking phase

Figure 3.1: Two scenarios with two different Tx beam patterns. In (a), a Tx (a base station or a car) broadcasts a common message exploring a wide angular sector. In (b), we consider directional BF towards the detected targets. The Rx always makes use of a wide beam within the angular sector of interest.

We remark here the used notation. $(\cdot)^{\mathsf{T}}$ denotes the transpose operation. $(\cdot)^{\mathsf{H}}$ denotes the Hermitian (conjugate and transpose) operation. Operator $|\cdot|$ denotes the absolute value $|x|$ if $x \in \mathbb{R}$, or the cardinality (number of elements) of a discrete set, i.e., $|\mathcal{F}|$, if $\mathcal{F}$ is a discrete set.

3.2 Physical model

We consider a joint radar detection and parameter estimation system operating over a channel bandwidth B and at the carrier frequency f_c. The Tx is equipped with a mono-static MIMO radar with N_{a} antennas and N_{rf} RF

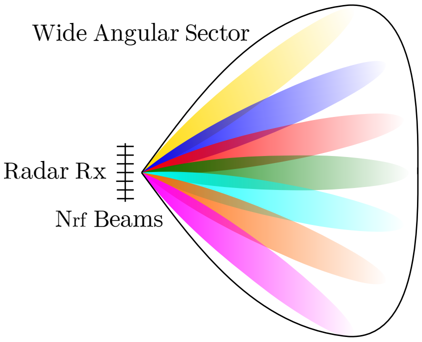

Figure 3.2: Beam configuration at the radar Rx for the two scenarios depicted in Fig. 3.1. N_{rf} beams cover a wide angular sector.

chains, operating in full-duplex mode.[2] The radar Rx (colocated with the Tx, i.e., mono-static assumption) processes the backscattered signal to identify the presence of targets within the beam, while estimating parameters of interest such as range, velocity, and AoA. A point target model is taken into account, such that each target can be represented through its LoS path only [17, 21, 15]. By letting the steering angle $\phi \in [-\frac{\pi}{2}, \frac{\pi}{2}]$, by considering an antenna array with $\lambda/2$ spacing (where λ is the wavelength), the Tx and Rx arrays are given by $\mathbf{a}(\phi)$ and $\mathbf{b}(\phi)$ respectively, where $\mathbf{a}(\phi) = (a_1(\phi), \dots, a_{N_a}(\phi))^{\intercal} \in \mathbb{C}^{N_a}$, denotes the uniform linear array response vector of the radar Rx with

$$a_n(\phi) = e^{j(n-1)\pi \sin(\phi)}, \quad n = 1, \dots, N_a, \tag{3.1}$$

and $b_n(\phi) = a_n(\phi)$. In fact, given the mono-static radar, the same steering angle ϕ is both at radar Tx and Rx, thus, vectors $\mathbf{a}$ and $\mathbf{b}$ result to be equal. The channel is modeled as an extension of the P-tap time-frequency selective

---

[2] Full-duplex operations can be achieved with sufficient isolation between the Tx and the (radar) detector and possibly interference analog pre-cancellation in order to prevent the (radar) detector saturation [31, 73, 32].

channel in (1.1) including the addition spatial dimension, which is given by [7]

$$\mathbf{H}(t,\tau) = \sum_{p=0}^{P-1} h_p \mathbf{b}(\phi_p)\mathbf{a}^{\mathsf{H}}(\phi_p)\delta(\tau-\tau_p)e^{j2\pi\nu_p t}\,, \tag{3.2}$$

whose dimension is $N_\mathrm{a} \times N_\mathrm{a}$, where P is the number of targets, h_p is a complex channel gain including the pathloss, $\nu_p = \frac{2v_p f_c}{c}$ and $\tau_p = \frac{2r_p}{c}$ are the round-trip Doppler shift and delay, while ϕ_p denotes the AoA, each corresponding to the p-th target, respectively.

3.2.1 OTFS Input Output Relation

We consider OTFS with M subcarriers of bandwidth Δf each, such that the total frequency band is given by $B = M\Delta f$. As already written in many previous chapters, T denotes the symbol time, and the OTFS frame duration is NT. The Doppler-delay dimensions, according to (1.13), are N and M, while the equation $T\Delta f = 1$ is always valid (see Chapter 1 and Sec. 1.3 for more details). In order to consider the aforementioned different operational modes, i.e., detection and tracking phases, we let N_s denote the number of data streams to be sent in each time-frequency slot, such that $N_\mathrm{s} = 1$ corresponds to the multicasting of a single data stream (in a possible detection phase where a base station wants to share a common information while detecting active targets) and $N_\mathrm{s} \leq N_\mathrm{rf}$ corresponds to the broadcasting of individual data streams (towards the active targets already detected in the previous phase).

Following the standard derivation of the input-output relation of OTFS (see Sec. 1.3), here we extend the equations to also consider the additional spatial dimension. Let us deal with N_s-dimensional data symbols $\{\mathbf{x}_{k,l}\}$, for $k = 0,\dots,N-1$, $l = 0,\dots,M-1$, belonging to any constellation, and arranged in the $N \times M$ two-dimensional Doppler-delay grid $\Gamma = \{(k/NT, l/M\Delta f)\}$ in (1.13). The Tx first applies the ISFFT to convert data symbols $\{\mathbf{x}_{k,l}\}$ into a $N_\mathrm{s} \times 1$ block $\{\mathbf{X}[n,m]\}$ in the time-frequency domain

$$\mathbf{X}[n,m] = \sum_{k=0}^{N-1}\sum_{l=0}^{M-1} \mathbf{x}_{k,l} e^{j2\pi\left(\frac{nk}{N}-\frac{ml}{M}\right)}, \tag{3.3}$$

for $n = 0, \ldots, N-1$, $m = 0, \ldots, M-1$, satisfying the average power constraint $\mathbb{E}[\mathbf{X}[n,m]^{\mathsf{H}}\mathbf{X}[n,m]] = P_{\text{avg}}/(NMN_{\text{a}})\mathbf{I}_{N_{\text{a}}}$, where $\mathbf{I}_{N_{\text{s}}}$ denotes an identity matrix of dimension N_{s} and P_{avg} some total maximum power allowed by the system. After assigning N_{s} streams to N_{rf} RF chains through a mapping matrix $\mathbf{V} \in \mathbb{C}^{N_{\text{rf}} \times N_{\text{s}}}$ (since generally $N_{\text{s}} \leq N_{\text{rf}}$, thus a mapping is necessary), the Tx generates the N_{rf}-dimensional continuous-time signal

$$\mathbf{s}(t) = \mathbf{V} \sum_{n=0}^{N-1} \sum_{m=0}^{M-1} \mathbf{X}[n,m] g_{\text{tx}}(t - nT) e^{j2\pi m \Delta f (t-nT)}, \tag{3.4}$$

in which $g_{\text{tx}}(t)$ is the shaping pulse applied in transmission (see Chapter 1 for more details and Sec. 1.3.8). Since the number of RF chains is typically much smaller than the number of antennas, different types of HDA architectures between RF chains and antennas have been considered in the literature (see e.g. [55]). In this paper, we focus on the fully-connected HDA scheme of [55]. For any HDA architecture, the Tx applies the hybrid BF matrix denoted by $\mathbf{F} \in \mathbb{C}^{N_{\text{a}} \times N_{\text{rf}}}$ that captures both baseband and RF analog BF (see [51, 54]), while the Rx sees the received signal of a reduced dimension through a projection matrix denoted by $\mathbf{U} \in \mathbb{C}^{N_{\text{rf}} \times N_{\text{a}}}$. By imposing $\text{tr}(\mathbf{F}\mathbf{V}\mathbf{V}^{\mathsf{H}}\mathbf{F}^{\mathsf{H}}) = N_{\text{a}}$, the total power constraint P_{avg} is satisfied. In other words, the Rx cannot access to each antenna element, but obtains only a projection of the received signal.

By transmitting the signal (3.4) over the channel (3.2), the N_{rf}-dimensional continuous-time received signal is given by

$$\mathbf{r}(t) = \sum_{p=0}^{P-1} h_p \mathbf{U}\mathbf{b}(\phi_p)\mathbf{a}^{\mathsf{H}}(\phi_p)\mathbf{F}\mathbf{s}(t - \tau_p) e^{j2\pi \nu_p t}, \tag{3.5}$$

where we omitted the noise for simplicity. It is interesting here to compare these equations with the single spatial dimensional ones presented in Sec. 1.3. The output of the Rx filter-bank adopting a generic receive shaping pulse

$g_{\mathrm{rx}}(t)$ is

$$\begin{aligned}\mathbf{y}(t,f) &= \int \mathbf{r}(t')g^*_{\mathrm{rx}}(t'-t)e^{-j2\pi f t'}dt' \\ &= \int_{t'} g^*_{\mathrm{rx}}(t'-t)\sum_{p=0}^{P-1} h_p\mathbf{U}\mathbf{b}(\phi_p)\mathbf{a}^{\mathsf{H}}(\phi_p)\mathbf{F}\mathbf{s}(t'-\tau_p)e^{j2\pi\nu_p t'}e^{-j2\pi f t'}dt' \\ &= \sum_{p,n',m'} h_p\mathbf{U}\mathbf{b}(\phi_p)\mathbf{a}^{\mathsf{H}}(\phi_p)\mathbf{F}\mathbf{V}\mathbf{X}[n',m']\int_{t'} g^*_{\mathrm{rx}}(t'-t)g_{\mathrm{tx}}(t'-\tau_p-n'T) \\ &\quad e^{j2\pi m'\Delta f(t'-\tau_p-n'T)}e^{j2\pi(\nu_p-f)t'}dt' \,. \end{aligned} \tag{3.6}$$

By sampling at $t = nT$ and $f = m\Delta f$, we obtain

$$\mathbf{y}[n,m] = \mathbf{y}(t,f)|_{t=nT, f=m\Delta f} = \sum_{n'=0}^{N-1}\sum_{m'=0}^{M-1}\mathbf{h}_{n,m}[n',m'] \,, \tag{3.7}$$

where the time-frequency domain input-output relation $\mathbf{h}_{n,m}[n',m']$ is

$$\begin{aligned}\mathbf{h}_{n,m}[n',m'] = &\sum_{p=0}^{P-1} h'_p\mathbf{U}\mathbf{b}(\phi_p)\mathbf{a}^{\mathsf{H}}(\phi_p)\mathbf{F}\mathbf{V}\mathbf{X}[n',m']e^{j2\pi n'T\nu_p} \\ &C_{g_{\mathrm{tx}},g_{\mathrm{rx}}}((n-n')T-\tau_p,(m-m')\Delta f-\nu_p)e^{-j2\pi m\Delta f\tau_p} \,, \end{aligned} \tag{3.8}$$

where $C_{u,v}(\tau,\nu)$ denotes the CAF, we let $h'_p = h_p e^{j2\pi\nu_p\tau_p}$, and imposed the term $e^{-j2\pi mn'\Delta fT} = 1$, $\forall n', m$, under the hypothesis $T\Delta f = 1$. Since each $X_i[n,m]$ is generated via ISFFT, the received signal in the delay-Doppler domain is obtained by the application of the SFFT

$$\mathbf{y}[k,l] = \sum_{n,m}\frac{\mathbf{y}[n,m]}{NM}e^{j2\pi(\frac{ml}{M}-\frac{nk}{N})} = \sum_{k',l'}\mathbf{g}_{k,k'}\left[l,l'\right] \,, \tag{3.9}$$

where the ISI coefficient of the Doppler-delay pair $[k',l']$ seen by sample $[k,l]$ is given by

$$\mathbf{g}_{k,k'}\left[l,l'\right] = \sum_p h'_p\mathbf{U}\mathbf{b}(\phi_p)\mathbf{a}^{\mathsf{H}}(\phi_p)\mathbf{F}\mathbf{V}\mathbf{x}_{k',l'}\Psi^p_{k,k'}[l,l'] \,, \tag{3.10}$$

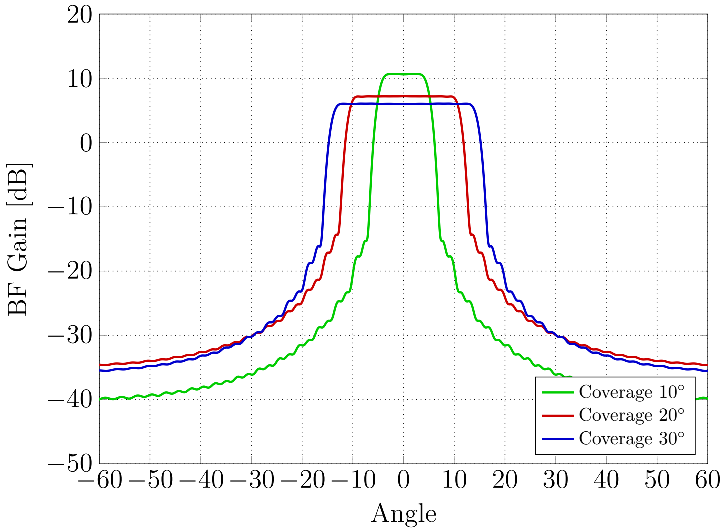

Figure 3.3: BF design for different angular coverage. Clearly, wider the beam, less the BF gain.

with $\Psi^{p}_{k,k'}[l,l']$ defined as

$$\Psi^{p}_{k,k'}[l,l'] = \sum_{n,n',m,m'} \frac{C_{g_{\mathrm{rx}},g_{\mathrm{tx}}}((n-n')T-\tau_p,(m-m')\Delta f-\nu_p)}{NM} e^{j2\pi n'T\nu_p}$$
$$e^{-j2\pi m\Delta f\tau_p} e^{j2\pi\left(\frac{n'k'}{N}-\frac{m'l'}{M}\right)} e^{-j2\pi\left(\frac{nk}{N}-\frac{ml}{M}\right)}, \tag{3.11}$$

while simplified version of $\Psi^{p}_{k,k'}[l,l']$ obtained by approximating the CAF can be found in Sec. 1.3.

3.2.2 Beamforming matrices

The design of the BF matrix $\mathbf{F}$ at the radar Tx depends on the operating phase, and anyway $\mathbf{F}$ is chosen such that Tx and Rx are aligned towards the same wide angular sector. Following [51, Section III.C], we construct $\mathbf{F} \in \mathbb{C}^{N_{\mathrm{a}}\times N_{\mathrm{rf}}}$ to cover a wide angular sector $[-\theta,\theta]$ as follows. By representing this angular sector by a discrete set of N_{rf} angles, denoted by $\Theta = \{\pm\left(\theta/(2N_{\mathrm{rf}}) + k\theta/N_{\mathrm{rf}}\right)\}$, for $k = 0, \dots, N_{\mathrm{rf}}/2 - 1$, each column of $\mathbf{F} = [\mathbf{f}_1, \dots, \mathbf{f}_{N_{\mathrm{rf}}}]$ takes the form

$$\mathbf{f}_i = \frac{\mathbf{a}(\theta_i)}{|\mathbf{a}(\theta_i)|}, \quad i = 1, \dots, N_{\mathrm{rf}}\,, \tag{3.12}$$

where $\mathbf{a}(\theta_i)$ is defined in (3.1) and taking into account a suitable normalization. An example on how the BF beams, w.r.t. the associated gain, look like is shown in Fig. 3.3, for different angular coverage.

During the target tracking phase, we form multiple narrow beams corresponding to the estimated AoA of the detected targets. This is illustrated with red and blue beams, corresponding to two different AoA, in Fig. 3.1b. Assuming that P targets are detected and their respective AoA are estimated, we construct $\mathbf{F}$ by replacing θ_i by $\hat{\phi}_p$ for the first P columns in (3.12) [51, Section III.B]. In such a case, the BF gain towards a single target is approximately $\simeq N_{\mathrm{a}}$, while decreases for each other considered target, i.e., $\simeq N_{\mathrm{a}}/P$.

Contrary to the transmit beamforming matrix, the reduction matrix $\mathbf{U}$ at the radar Rx remains the same for both detection and tracking phases. Namely, we set $\mathbf{U} = \mathbf{F}^{\mathsf{H}}$, where each column is given in (3.12). This is illustrated in Fig. 3.2. This choice of an isotropic receive beam enables to obtain a multi-dimensional signal for AoA estimation in both detection and tracking phases.

3.3 Joint Detection and Parameters Estimation

We wish to estimate the set of four parameters $\boldsymbol{\theta} = \{h'_p, \phi_p, \tau_p, \nu_p\} \in \mathcal{T}^P$, with $\mathcal{T} = \mathbb{C} \times \mathbb{R} \times \mathbb{R} \times \mathbb{R}$. By defining

$$\mathbf{G}_p(\tau_p, \nu_p, \phi_p) \triangleq \left(\mathbf{U}\mathbf{b}\left(\phi_p\right)\mathbf{a}^{\mathsf{H}}(\phi_p)\mathbf{F}\mathbf{V}\right) \otimes \boldsymbol{\Psi}^p\,, \tag{3.13}$$

where $\otimes$ is the Kronecker product,[3] as the $N_{\mathrm{rf}}NM \times N_{\mathrm{s}}NM$ matrix obtained by multiplying $\boldsymbol{\Psi}^p$ by a different coefficient of $\left(\mathbf{U}\mathbf{b}\left(\phi_p\right)\mathbf{a}^{\mathsf{H}}(\phi_p)\mathbf{F}\mathbf{V}\right)$. Thus, by stacking $\mathbf{X}$ into a $N_{\mathrm{s}}NM$-dimensional vector $\mathbf{x}$ and defining an output vector

---

[3] Note that $\mathbf{A}^{X\times Y} \otimes \mathbf{B}^{Z\times K} = \mathbf{C}^{XZ\times YK}$.

$\mathbf{y}$ of dimension $NMN_{\mathrm{rf}} \times 1$, the received signal in the presence of noise is

$$\mathbf{y} = \sum_{p=0}^{P-1} \left[h'_p \mathbf{G}_p(\tau_p, \nu_p, \phi_p)\right] \mathbf{x} + \mathbf{w}\,, \tag{3.14}$$

where $\mathbf{w}$ denotes the AWGN vector with independent and identically distributed entries of zero mean and variance σ_w^2. The problem consists, first, of the detection of the P targets (in case of a first acquisition phase), together with the estimation of the associated $4P$ parameters (complex channel coefficient, Doppler, delay, and angle) from the $N_{\mathrm{rf}}MN$-dimensional received signal. To this end, we define the ML function as

$$\begin{aligned} l(\mathbf{y}|\boldsymbol{\theta}, \mathbf{x}) &= \left|\mathbf{y} - \sum_p h'_p \mathbf{G}_p \mathbf{x}\right|^2, \\ &= \mathbf{y}^{\mathsf{H}}\mathbf{y} - \mathbf{y}^{\mathsf{H}} \sum_p h'_p \mathbf{G}\mathbf{x} - \sum_p h'^{*}_p \mathbf{x}^{\mathsf{H}} \mathbf{G}^{\mathsf{H}} \mathbf{y} \\ &\quad + \mathbf{x}^{\mathsf{H}} \left(\sum_p h'_p \mathbf{G}\right)^{\mathsf{H}} \left(\sum_q h'_q \mathbf{G}_q\right) \mathbf{x}\,, \end{aligned} \tag{3.15}$$

where we use the short hand notation $\mathbf{G}_p \triangleq \mathbf{G}(\tau_p, \nu_p, \phi_p)$. Note the similarities and differences w.r.t. (2.27). The ML solution is given by

$$\hat{\boldsymbol{\theta}} = \arg \min_{\boldsymbol{\theta} \in \mathcal{T}^P} l(\mathbf{y}|\boldsymbol{\theta}, \mathbf{x}). \tag{3.16}$$

For a fixed set of $\{\phi_p, \tau_p, \nu_p\}$, the ML estimator of $\{h'_p\}$ is given by solving the following set of equations

$$\mathbf{x}^{\mathsf{H}} \mathbf{G}_p^{\mathsf{H}} \left(\sum_{q=0}^{P-1} h'_q \mathbf{G}_q\right) \mathbf{x} = \mathbf{x}^{\mathsf{H}} \mathbf{G}_p^{\mathsf{H}} \mathbf{y}, \quad p = 0, \dots, P-1. \tag{3.17}$$

By plugging (5.34) into (5.32), it readily follows that minimizing $l(\mathbf{y}|\boldsymbol{\theta}, \mathbf{x})$ reduces to maximize the following function

$$l_2(\mathbf{y}|\boldsymbol{\theta}, \mathbf{x}) = \sum_p h'_p \mathbf{y}^{\mathsf{H}} \mathbf{G}_p \mathbf{x} = \sum_p S_p(\tau_p, \nu_p, \phi_p) - I_p(\{h'_q\}_{q \neq p}, \boldsymbol{\theta})\,, \tag{3.18}$$

where $S_p(\tau_p, \nu_p, \phi_p)$ and $I_p(\{h'_q\}_{q\neq p}, \boldsymbol{\theta})$ (S_p and I_p in short hand notation) denote the useful signal and the interference term for target p, given respectively by

$$S_p = \frac{|\mathbf{y}^{\mathsf{H}}\mathbf{G}_p\mathbf{x}|^2}{|\mathbf{G}_p\mathbf{x}|^2}\,, \tag{3.19}$$

$$I_p = \frac{(\mathbf{y}^{\mathsf{H}}\mathbf{G}_p\mathbf{x})\,\mathbf{x}^{\mathsf{H}}\left(\mathbf{G}_p^{\mathsf{H}}\sum_{q\neq p} h'_q\mathbf{G}_q\right)\mathbf{x}}{|\mathbf{G}_p\mathbf{x}|^2}\,. \tag{3.20}$$

Notice that we have $I_p = 0$ if there is only one target.

3.3.1 Successive Interference Cancellation (SIC) and Joint Target Detection and Parameters Estimation Algorithm

The use of OTFS for radar tasks introduces some limitations. In particular, by looking at the assumption $T\Delta f = 1$, the CAF $C_{\mathrm{gtx},\mathrm{grx}}(\tau, \nu)$ incurs significant side-lobes in the Doppler-delay domain. As a result, our simulations show that the magnitude of the useful signal, i.e., $\max_{(\tau,\nu)} S_p(\tau, \nu, \phi)$, has a main lobe around the (true) angle ϕ_p of target p and non-negligible side-lobes in the angular domain. Since the signal magnitude strictly depends on the received backscattered power, the sidelobes of a strong target, closer to the radar, may completely mask (having greater magnitude) the main lobe of weaker targets, far from the radar. Therefore, situations of near-far effect among the targets, causing large power imbalance in the backscattered waves, must be handled explicitly by some additional signal processing. This motivates us to incorporate a SIC mechanism our ML-based target detection.

Given the received signal in (3.14), once a strong target is detected and its radar parameters are estimated, its contribution, and thus the masking effect, can be removed from the received signal (see (3.24) in Algorithm 2). This process can be run iteratively to cancel the contributions of new detected targets, until a given condition or stopping criteria is satisfied (e.g., a target is found in an angular sector already explored, or the magnitude of the useful signal goes below a certain value). Algorithm 2 describes the steps to perform joint detection and radar parameters estimation. Some remarks on Algorithm 2 are in order:

Remark: Equation (3.21)
In (3.21), T_r is the detection threshold, to be properly optimized, Γ is the Doppler-delay grid described in Section 3.2.1 and Ω is defined as a discretized set of angles. The p-th target is associated to a coarse estimation $(\hat{\phi}_p, \hat{\tau}_p, \hat{\nu}_p)$, such that $S_p(\hat{\phi}_p, \hat{\tau}_p, \hat{\nu}_p)$ is above the threshold and is a local maximum.

Remark: Target Detection
Equation (3.21) presents a threshold test requiring the search over a three dimensional grids composed of $|\Omega|$ slices of the $N \times M$ Doppler-delay grid. In order to keep the complexity low, we consider the Doppler-delay grid Γ defined in Section 3.2.1 and a coarse Ω.[4] Even if this assumption is rather restrictive, it provides a computationally feasible and fast coarse estimation (step 1 of Algorithm 2), to be used as a baseline for the successive super-resolution ML-based parameter estimation (step 2 of Algorithm 2).

Remark: Fine AoA Estimation
Since S_p is a convex function in ϕ for a fixed pair (τ_p, ν_p), the result of (3.22) can be exactly computed using common convex solvers. Therefore, the angle can be estimated with super-resolution far beyond the discrete grid Ω.

Remark: The magnitude of S_p strictly depends on the target range (and pathloss). Thus, in order to keep a fixed threshold T_r for all iterations, the argument $\max_{(\tau,\nu)} S_p(\tau, \nu, \phi)$ has to be normalized at each iteration, for instance, w.r.t. its mean computed over all possible angles.

---

[4] For instance, with an angular sector covering of 60 degrees divided in 4 equally spaced parts, the set of angles results to be (supposing the center of the beam to be at 0 degree) $\Omega = \{[-30, -15], [-15, 0], [0, 15], [15, 30]\}$.

Algorithm 2: *Joint Detection and Radar Parameters Estimation*

```
Result: Target detection and radar parameter estimation.
Initialization: Set $\mathbf{y}' = \mathbf{y}$; Detected targets $N_{\mathrm{dt}} = 0$;
Repeat
    1) Detection / (AOA, Doppler, Delay) Coarse Estimation:
    Given $\mathbf{y}'$, search a possible set of targets
        $\mathcal{P} = \left\{ \max_{(\tau,\nu)} S_p(\tau, \nu, \phi) > T_r \right\}, \text{ s.t. } \left\{ \forall\, (\tau, \nu, \phi) \in \Gamma \times \Omega \right\}.$   (3.21)
    2) Super-Resolution Parameter Estimation:
    2.1) Fine AOA:
        $\hat{\phi}_p = \arg\max_{\phi} S_p(\hat{\tau}_p, \hat{\nu}_p, \phi), \quad p = 1, \ldots, |\mathcal{P}|.$   (3.22)
    2.2) Fine Doppler-delay Estimation:
    Initialization: Iteration $i = 0$, initialize $\hat{h}'_p[0] = 0$.
    For Iteration $i = 1, 2, \ldots$ do
        • Delay and Doppler update: Find the estimates $\hat{\tau}_p[i], \hat{\nu}_p[i]$ by solving the two-dimensional maximization
            $(\hat{\tau}_p[i], \hat{\nu}_p[i]) = \arg\max_{(\tau,\nu)} \left\{ S_p - I_p \right\},$   (3.23)
        with $S_p$ and $I_p$ computed for $(\hat{h}'_p[i], \tau, \nu, \hat{\phi}_p[i])$;
        • Complex channel coefficients update: Solve the linear system (5.34) using channel matrices $\mathbf{G}_p$ with parameters $(\hat{h}'_p[i], \hat{\tau}_p[i], \hat{\nu}_p[i], \hat{\phi}_p)$, and let the solution be denoted by $\hat{h}'_p[i]$;
    End
    3) Re-Fine AOA: Compute (3.22) using $(\hat{\tau}_p, \hat{\nu}_p)$ obtained in (3.23);
    4) SIC: Compute
        $y' = y - \sum_{p=0}^{|\mathcal{P}|} \left[ \hat{h}'_p \mathbf{G}_p(\hat{\tau}_p, \hat{\nu}_p, \hat{\phi}_p) \right] \mathbf{x},$   (3.24)
    increase targets counter $N_{\mathrm{dt}} = N_{\mathrm{dt}} + |\mathcal{P}|$;
Until Stopping Criterion;
```

3.3.2 Reduced-Complexity Parameter Estimation

In the target tracking phase, the matrix $\mathbf{G}_p$ in (3.13) shall be updated dynamically as the BF matrix $\mathbf{F}$ of dimension $N_{\mathrm{a}} \times N_{\mathrm{rf}}$ and the channel matrix $\mathbf{\Psi}^p$ of $NM \times NM$ change in time. The following solution can be adopted in order to reduce the computational complexity related to the dynamically changing matrices. Namely, we compute $\mathbf{G}_p$ for target p by selecting only the column of $\mathbf{F}$ corresponding to target p, already detected in Step 1 of Algorithm 2. Assuming that targets are located with different ranges from the radar, this low-complexity method does not affect the parameter estimation performance. If there are few targets located with similar ranges from the radar, they can be grouped together within the same narrow beam.

3.3.3 Cramér-Rao Lower Bound (CRLB)

We consider the CRLB as a theoretical benchmark. In order to estimate a complex channel coefficient, we let $A_p = |h'_p|$ and $\psi_p = \angle(h'_p)$ denote the amplitude and the phase of h'_p, respectively. Thus, $5P$ real variables have to be estimated, i.e., $\boldsymbol{\theta} = \{A_p, \psi_p, \tau_p, \nu_p, \phi_p\}$. We form the $5P \times 5P$ Fisher information matrix whose (i, j) element is

$$[\mathbf{I}(\boldsymbol{\theta})]_{i,j} = \frac{2}{N_0}\mathrm{Re}\left\{\sum_{n,m,t}\left[\frac{\partial s_p^{[n,m,t]}}{\partial \theta_i}\right]^*\left[\frac{\partial s_q^{[n,m,t]}}{\partial \theta_j}\right]\right\}, \tag{3.25}$$

where $p = [i]_P$, $q = [j]_P$, and

$$s_p^{[n,m,t]} = A_p e^{j\psi_p} b_t(\phi_p) a_t^*(\phi_p) f_t \sum_{k,l} \Psi_{n,k}^p[m,l] x_{k,l}\,, \tag{3.26}$$

where (n, m, t) denote time, subcarrier, and antenna, respectively, while f_t is the t-th entry of the BF vector of any RF chain.[5] Note that, even if not explicitly indicated for the sake of simplicity, the summations w.r.t. k and l

---

[5] Here we assume that, given a proper BF design, the beam patterns directed to different targets do not interfere. Hence, we completely neglect beam interference, and only a BF vector entry f_t appears at a time.

Table 3.1: System parameters

$N = 6$	$M = 512$
$f_c = 24.25$ [GHz]	$B = 150$ [MHz]
$v_{\text{res}} \simeq 440$ [km/h]	$r_{\text{res}} \simeq 1$ [m]
$v_{\max} = N \cdot v_{\text{res}}$	$r_{\max} = M \cdot r_{\text{res}}$
$P_{\text{avg}} = 40$ [mW]	$\sigma_{\text{rcs}} = 1$ [m^2]
Noise Figure = 3 [dB]	Noise PSD = $2 \cdot 10^{-21}$ [W/Hz]
$N_{\text{a}} = 16, 32, 64, 128$	$N_{\text{rf}} = 8$

extend from 0 to $N-1$ and $M-1$, respectively, as in all previous analysis. The desired CRLB is obtained taking the diagonal elements of the inverse Fisher information matrix, filled with the corresponding derivatives.

3.4 Numerical Results

We set the number of RF chains to $N_{\text{rf}} = 8$, such that a single equipment is able to jointly track and communicate to N_{rf} distinct targets (or groups of targets), while $N_{\text{rf}} \ll N_{\text{a}}$. Table 3.1 provides all system parameters.

In our simulations, we rely on the following assumptions:

- Given the choice of a mmWave communication, we assume a single LoS path between the Tx and the radar target [17, 21, 15]. This is motivated by the fact that any possible scattering component different from the LoS generally brings much lower power, given the additional reflections of the echo signal.

- Any backscattered power to the radar Rx is considered as a possible target. The objective is to sense the surrounding environment, and the differentiation between active targets and obstacles is a post-processing decision. Clearly, in a second phase, communication is established only towards active targets.

- We consider the complete blockage of the signal propagation to the first object hit. This assumption is completely fulfilled in mmWave communication scenarios.[6]

Note that the aforementioned assumption are shared by many works in literature (see, e.g., [15] and references therein).

The radar two-way pathloss is defined as [13, Chapter 2]

$$\mathrm{PL} = \frac{(4\pi)^3 r^4}{\lambda^2}\,, \tag{3.27}$$

and the definition of the radar SNR becomes

$$\mathrm{SNR} = \frac{\lambda^2 \sigma_{\mathrm{rcs}} G_{\mathrm{Tx}} G_{\mathrm{Rx}}}{(4\pi)^3\, r^4} \frac{P_{\mathrm{avg}}}{\sigma_w^2}\,, \tag{3.28}$$

where $\lambda = c/f_c$ is the wavelength, c is the speed of light, σ_{rcs} is the radar cross-section of the target in m^2, G_{Tx} and G_{Rx} are the antenna gains at the Tx and Rx respectively, r is the distance between Tx and Rx, and σ_w^2 is the variance of the AWGN noise with noise power spectral density (PSD) of $2 \cdot 10^{-21}$ [W/Hz]. We choose $\sigma_{\mathrm{rcs}} = 1$ [m^2], while different choices can be found in literature [74, 75]. Note that, while G_{Tx} can change with the operational mode, G_{Rx} is kept constant (within the angular sector of interest) in order to allow isotropic reception, as already explained. Information about antenna gains, beam patterns, two-way (Tx and Rx) beamwidth, and more antenna basics (also for mono-static radars) can be found, for instance, in [76, 51]. The detection threshold T_r in Algorithm 2 has been numerical evaluated in order to have a fixed false alarm probability of 10^{-4} (as done, e.g., in [15]).

---

[6] Note that the proposed algorithm could be able to correctly distinguish more targets sharing the same angular direction, if separated in at least one other domain (Doppler or delay) [71].

While two distinct targets in the angle domain can be identified if the angular resolution meets some conditions (depending on the number of antennas, the angular distance between the two targets, and the antenna array properties) [13]. The velocity and the range resolution is determined by the system parameters in Table 3.1 and given by

$$v_{\text{res}} = \frac{Bc}{2NMf_c} \text{ [m/s]}\,, \quad r_{\text{res}} = \frac{c}{2B} \text{ [m]}\,. \tag{3.29}$$

In order to get a reasonable range resolution, e.g., < 1 [m], a large bandwidth has to be considered.[7] Since the velocity resolution is directly proportional to B, for a fixed f_c, the only way to obtain lower values is to increase the block size NM, leading to a remarkable increase in computational complexity, which could be not affordable. For this reason, we set the system parameters by focusing on a reasonable range resolution (and theoretical maximum range) under a feasible computational complexity. Note that the maximum range could not be achieved if the backscattered power is below the noise floor. However, the chosen system setup leads to an unavoidable very large velocity resolution. Under the aforementioned assumptions, taken at the beginning of Section 5.4, the problem of targets identifiability appears only in the angular domain. However, this only happens at mmWave, thus, range and velocity resolutions are reported here for completeness, since the proposed scheme could target lower frequencies, where the aforementioned assumption might not be satisfied.

Remark: The parameter estimation performance of the proposed ML-based algorithm, in particular range and velocity estimation, strictly depends on the dimension of the block of data sent, i.e., the product $N \cdot M$. Thus, the system parameters of Tab. 3.1 can be easily tuned to achieve the desired levels of radar resolutions (modifying the bandwidth), acquisition time (based on the length of the OTFS frame in time), maximum range, etc. Clearly, the CRLB changes accordingly. Moreover, note that this is also possible thanks to

---

[7] Note that a tradeoff appears. Larger bandwidths mean more precise resolution, but lower theoretical maximum range (with the same $N \times M$ grid). We remark that our algorithm is completely independent of these choices.

OTFS modulation, which is not sensitive to Doppler and delay effects.

Remark: The (radar) range and velocity resolution in (3.29) indicates the minimum necessary targets spacing, in one of the two domains, such that both of them are distinguishable at the radar Rx. This is not linked to the performance of our ML-based detector, which is able to accurately estimate the parameters far beyond the resolution in (3.29). Thus, there is a huge difference between targets identifiability and estimation performance.

3.4.1 Simulation Results

Fig. 3.4 shows the radar performance in terms of probability of detection (PD), range/velocity/AoA estimation during the detection phase (Fig. 3.1a). When more than one target is considered within the simulation scenario, the PD P_{d} is averaged w.r.t. all P targets, i.e.,

$$P_{\mathrm{d}} = \frac{\sum_{p=0}^{P-1} P_{\mathrm{d}}(p)}{P}\,, \tag{3.30}$$

where $P_{\mathrm{d}}(p)$ denoted the PD of the p-th target.

First, note that, by considering an angular coverage of 10 degrees (blue line), the maximum range to correctly identify a target, limited by the pathloss and thus different from the theoretical limit indicated in Table 3.1, is about 110 m. For any distance between Tx and target, the estimation performance of radar parameters of interest (range, velocity, and AoA) follows the corresponding CRLB. More in details, note that at the limit range of 110 m, the RMSE for range, velocity, and angle are respectively, $\simeq 4 \cdot 10^{-2}$ [m], $\simeq 1.6 \cdot 10^{1}$ [m/s], $\simeq 4 \cdot 10^{-2}$ [degree]. As expected, given the system parameters, the velocity RMSE is quite poor, while the other estimation performances are satisfactory. However, a proper BF design towards targets, in a subsequent tracking phase, could improve the estimation performance maximizing the received SNR, as showed in next results. As seen from Fig. 3.4, by increasing the angle sector from 10° to 30°, the backscattered power gets smaller (less BF gain), hence the maximum range significantly decreases. There exists a non-trivial tradeoff

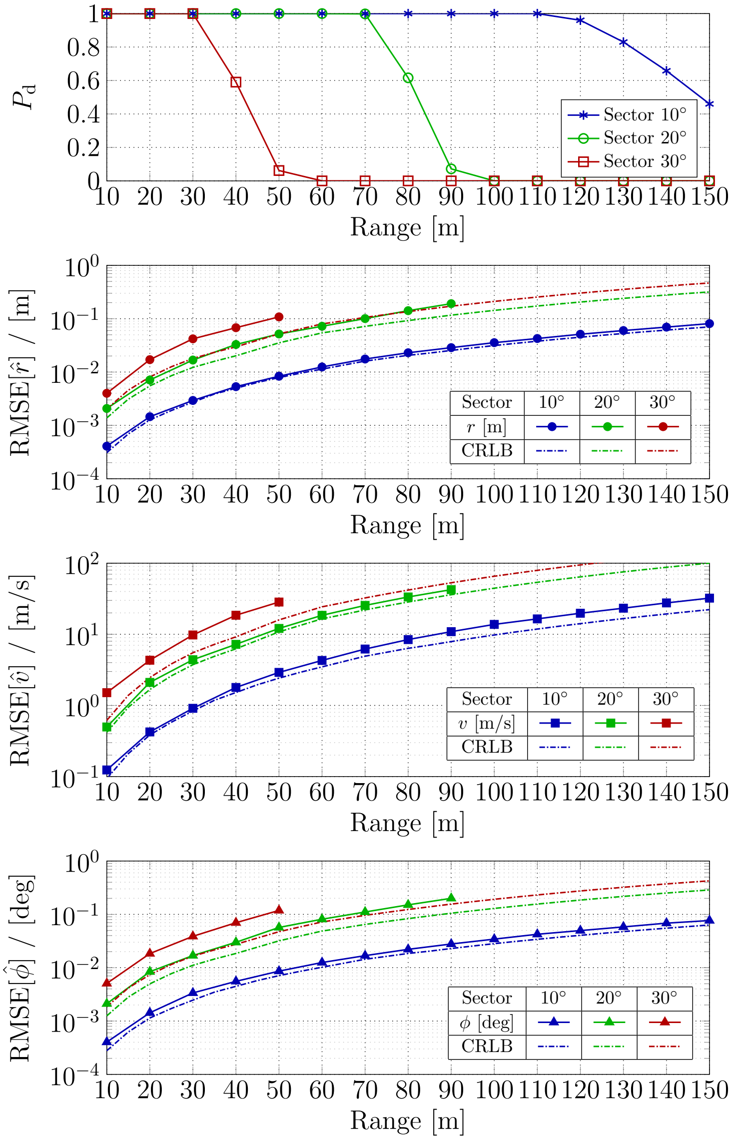

Figure 3.4: Detection phase. Single target at a different distance within the illuminated angular sector of specified coverage. RMSE performance with associated CRLB and detection performance. $N_a = 128$.

between the width of beams and radar performance. Wider angular sectors allow to explore the environment in less time, but with limited maximum range, while narrower sectors maximize the received power and the maximum target range, at the cost of a time consuming beam sweeping search. Clearly, RMSE performance can not be computed if the PD is equal to 0, i.e., the target is not detected, thus RMSE curves may stop at certain ranges, as visible in Fig. 3.4.

Fig. 3.5 shows the performance of the SIC technique presented in Algorithm 2 during the detection phase in the scenario depicted in Fig. 3.6. Namely, the Tx wishes to detect two targets, one at fixed distance of 10 [m], the other moving w.r.t. the x-axis, i.e., from 20 to 150 [m] (see Fig. 3.6). SIC is necessary because the closer target (black car) will mask the further target (blue car) so that the latter cannot be detected. First, the first plot of Fig. 3.5, referred to the PD, shows that, when the moving target is located at ranges greater than 90 [m], corresponding to the relative range beyond 80 [m], the masking effect is not removed efficiently by the SIC technique (the residual interference is remarkable), and the target at longer distance is not detected correctly. In fact, at the extreme point, the curve flats to $P_d = 0.5$, because only one target out of two (clearly, the closest to the radar Rx, i.e., the one fixed at 10 [m]) is correctly detected. As clearly visible, the performance in terms of RMSE, which considers in this case the estimation performance averaged w.r.t. the detected targets (note that the target located at 10 [m] is always detected correctly), slightly changes while considering one or two targets, as a confirmation of the effectiveness of the proposed algorithm. Note that the blue curves of Fig. 3.5 correspond to the blue ones of Fig. 3.4.

Now we consider the tracking phase corresponding to Fig. 3.1b. The scenario takes into account one Tx and three targets within an angular sector of 10°, as shown in Fig. 3.7. Fig. 3.8 shows the RMSE performance of the reference target (black car), in the presence of other two targets (blue cars), Note that distance, velocity, and angular position of all three targets are randomly chosen at every Monte Carlo iteration, in such a way the complete masking

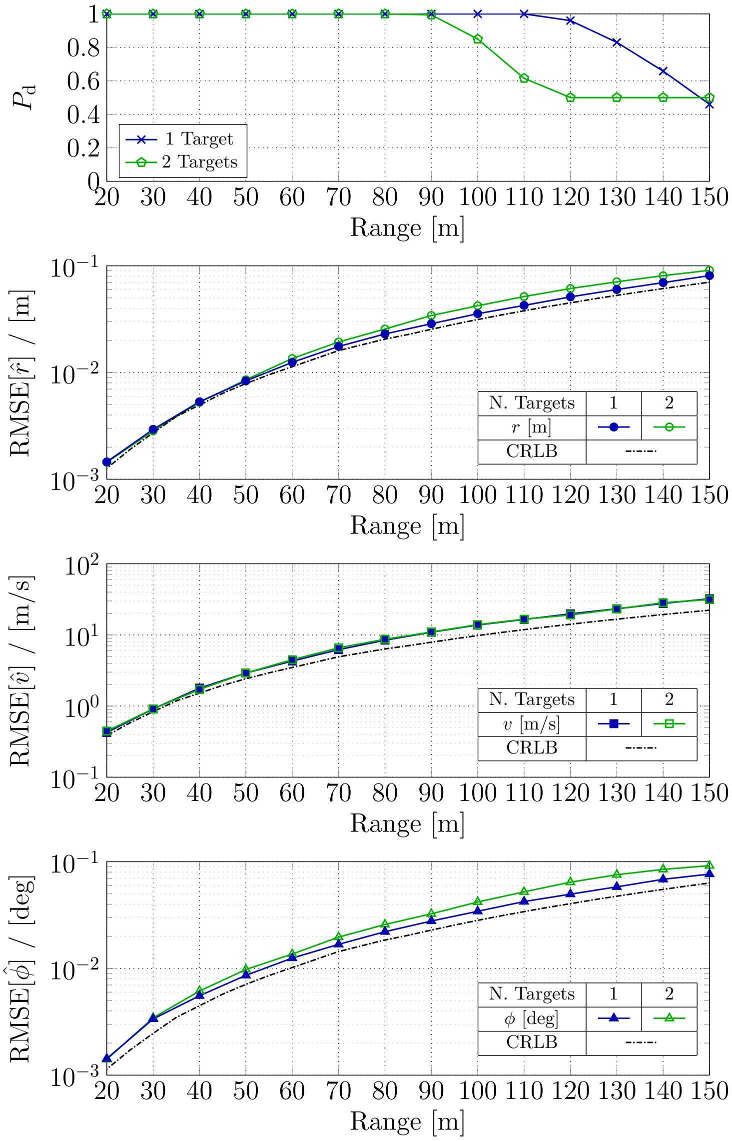

Figure 3.5: Detection phase. Two target, one located at 10 [m] and the other moving at a different distance (x-axis) within the illuminated 10° angular sector as shown in Fig. 3.6. RMSE performance with associated CRLB. Detection performance. $N_a = 128$.

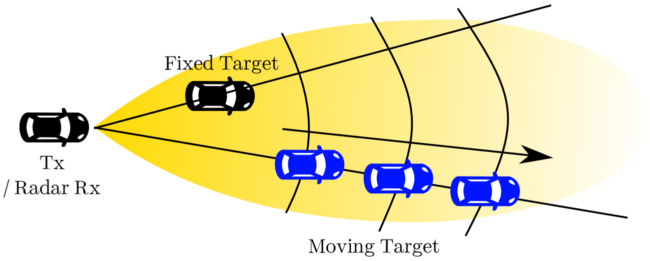

Figure 3.6: Example of scenario depicted in Fig. 3.5. The fixed target (in black) masks the moving target, in blue, which changes its location within the illuminated angular sector.

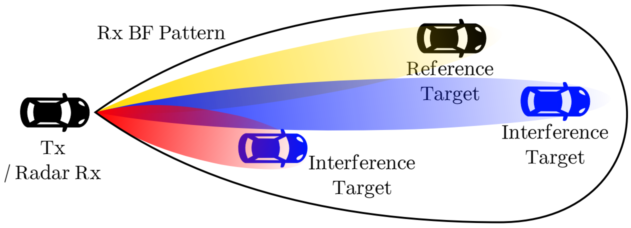

Figure 3.7: Example of scenario depicted in Fig. 3.8. The goal is to correctly estimate the parameters of the reference target (in black), while interference targets (in blue) lay within the same Rx BF pattern (depicted in Fig. 3.2 and with the black shape in this figure).

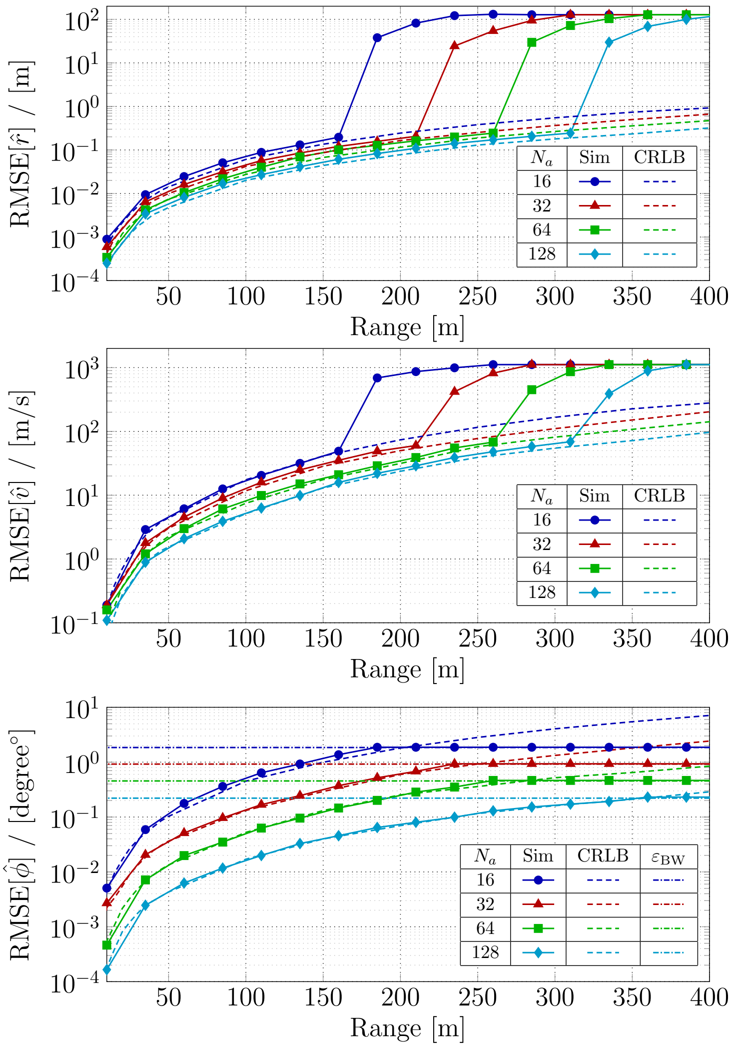

Figure 3.8: Tracking scenario. Tx BF distinct beams towards three different targets.

effect presented in Fig. 3.5 does not occur, and an average of RMSE results is finally computed. From Fig. 3.8, we observe that the RMSE critically depends on the number of antennas. This is because the BF gain grows proportionally with the number of antennas and increases the backscattered signal power. Moreover, note that a (reversed) “waterfall” behavior is shown for range and velocity estimation. This is because, even if the presence of the target is given for granted, low SNR values might still lead to a large error during the Doppler-delay ML maximization (see Algorithm 2). The waterfall behavior is typical of ML estimators and has been extensively analyzed in Sec. 2.1.2.3. Also note that the AoA RMSE performance is upper limited by the 3-dB beamwidth of the beam pattern (see, e.g., [51, 76]). In fact, supposing that the target position lies within the 3-dB beamwidth, also the initial AoA estimation (the upper and lower limit of matrix Ω in (3.21)) is limited to that width. As a consequence, the RMSE does not exceed a systematic error, indicated as $\varepsilon_{\mathrm{BW}}$, calculated by averaging over random AoA estimation realizations within the range of possibilities, i.e., between the upper and lower limit set by the 3-dB beamwidth of the beam pattern, equivalently of the analysis related to (2.44), which can be also applied to range and velocity estimations.

Chapter 4

OTFS Detection

4.1 Introduction

We will now focus on the OTFS data detection at the Rx side. By considering the communication-oriented channel model in (1.1), i.e., taking into account one-way Doppler and delay shift (modeling a forward communication channel, against the radar two-way scenario), in line with most of the current literature on OTFS detection (e.g., [62, 4]) we assume perfect CSI at the Rx, i.e., the knowledge of channel matrix $\mathbf{\Psi}$. The acquisition of such CSI is a distinct problem of independent interest, that will be analyzed in 5 and has been studied in literature in recent years (see, e.g., [37, 44, 45]).

In this chapter, we consider separate detection and decoding, where the Rx consists of the concatenation of a soft-output symbol detector, producing soft-estimates of the coded symbols $\mathbf{x}$, and a (separate) decoder that takes such estimates as the output of a virtual channel that incorporates also the detector. Thus, we do not consider "turbo equalization" schemes, in which detection and decoding are jointly performed through successive iterations involving feedback loops (as, e.g., in [77]). This choice is justified by the fact that the presence of a forward error correction scheme, together with the specific definition of the channel model, could obscure the real performance of the detection scheme, which could result optimal in a turbo equalization paradigm, but not when detection and decoding are separated (scheme motivated by practical complexity considerations). It follows that the relevant performance measure is the pragmatic capacity, i.e., the mutual information computed between the input constellation symbols, used with uniform probability, and the corresponding detector soft-output [78, 79]. In our opinion, for the aforementioned discussion, this kind of performance metric is more meaningful w.r.t., e.g., bit error rate (BER) analysis, generally used in the current literature [62, 4, 5].

We build an efficient low-complexity message passing (MP)-based soft-output detector, obtained by constructing a factor graph (FG) (see [80]) for the joint posterior probability of the transmitted symbols $\mathbf{x}$ given the received samples $\mathbf{y}$ in (2.17), while applying the standard sum-product algorithm (SPA) computation rules to compute its marginals probabilities (see [80]). The FG is constructed according to the general approach of [81] (applicable to any linear-Gaussian model such as (2.17)), for which the graph girth, i.e., minimum length of cycles, (see, e.g., [82]) is guaranteed to be at least 6, thus eliminating destructive length-4 loops (see, e.g., [77, 81, 80]), and the degree of the function nodes is at most 2. This allows the application of the exact SPA computation at the nodes and a high degree of parallelization (nodes operations can be performed independently), such that the resulting MP-based detector is very computationally efficient.[1] Furthermore, the absence of cycles of length less than 6 yields good convergence properties of the SPA iterations.

For numerical results, the low-complexity MP-based detector is compared to three other soft-output detectors proposed in the literature, namely: i) a different MP-based detector recently proposed in [62], based on an alternative way to construct the FG, but under some simplifying assumptions (see Section 4.2.2); ii) a standard linear minimum mean square error (MMSE) block

---

[1] Note that this is what is generally done in low-density parity check (LDPC) decoding, for which check nodes operations are performed in parallel by independent signal processing entities, drastically reducing the computational time [83].

equalizer, which offers very good performance at the impractical cost of a very large-dimensional matrix inversion (see [4, 5]); iii) a low-complexity MMSE block equalizer recently proposed in [47] that uses drastic simplifying assumptions (in particular, the bi-orthogonality of OTFS $g_{\rm tx}(t)$ and $g_{\rm rx}(t)$ pulses and the assumption that the delay and Doppler shifts are integer multiples of the Doppler-delay grid) such that the resulting *nominal* channel matrices $\boldsymbol{\Psi}_p$ are block-circulant with circulant blocks and the matrix inversion in linear MMSE estimation can be efficiently implemented. As we shall see, since these simplifying assumptions are not verified in practice (shifts are not on a quantized grid and bi-orthogonal pulses with unit time-frequency product cannot exist [84]), the performance of this low-complexity linear detector is quite poor, when applied to a realistic channel and pulse scenario.

4.2 The Detectors

4.2.1 Proposed MP-based detector (“Matrix G algorithm” — MP$_{\mathbf{G}}$)

From (2.17), recalled here for convenience

$$\mathbf{y} = \sum_{p=0}^{P-1} h_p \boldsymbol{\Psi}^p(\tau_p, \nu_p)\mathbf{x} + \mathbf{w}\,, \tag{4.1}$$

when $\boldsymbol{\Psi}$ is known (perfect CSI) and $\boldsymbol{w}$ is composed of complex Gaussian i.i.d. samples with variance σ_w^2, the conditional probability density function (pdf) of the received samples $\mathbf{y}$ given the modulation symbols $\mathbf{x}$ is given by

$$p\left(\mathbf{y}|\mathbf{x}\right) = \frac{1}{\left(2\pi\sigma_w^2\right)^{-NM}} \exp\left(-\frac{\|\mathbf{y}-\boldsymbol{\Psi}\boldsymbol{x}\|^2}{2\sigma_w^2}\right) \propto \exp\left(-\frac{\|\mathbf{y}-\boldsymbol{\Psi}\boldsymbol{x}\|^2}{2\sigma_w^2}\right), \tag{4.2}$$

where the proportionality operator removes an irrelevant constant factor independent of symbols $\mathbf{x}$. By following the FG construction approach of [81], we expand the ℓ_2-norm inside the exponential as

$$\|\mathbf{y}-\boldsymbol{\Psi}\boldsymbol{x}\|^2 = \mathbf{y}^{\mathsf{H}}\mathbf{y} - 2\mathrm{Re}\left\{\mathbf{x}^{\mathsf{H}}\boldsymbol{\Psi}^{\mathsf{H}}\mathbf{y}\right\} + \mathbf{x}^{\mathsf{H}}\boldsymbol{\Psi}^{\mathsf{H}}\boldsymbol{\Psi}\mathbf{x}. \tag{4.3}$$

Defining $\boldsymbol{z} \triangleq \mathbf{\Psi}^{\mathsf{H}}\mathbf{y}$ and $\mathbf{G} \triangleq \mathbf{\Psi}^{\mathsf{H}}\mathbf{\Psi}$, the conditional pdf can be written as

$$p\left(\mathbf{y}|\mathbf{x}\right) \propto \exp\left(\frac{2\mathrm{Re}\left\{\mathbf{x}^{\mathsf{H}}\boldsymbol{z}\right\} - \mathbf{x}^{\mathsf{H}}\mathbf{G}\boldsymbol{z}}{2\sigma_w^2}\right) . \tag{4.4}$$

Note that the sequence $\boldsymbol{z}$ is a sufficient statistic for symbol detection. By expressing the matrix operations explicitly in terms of their components, we define the functions

$$F_i\left(x_i\right) \triangleq \exp\left[\frac{1}{\sigma_w^2}\mathrm{Re}\left\{z_i x_i^* - \frac{G_{i,i}}{2}\left|x_i\right|^2\right\}\right] , \tag{4.5}$$

$$I_{i,j}\left(x_i, x_j\right) \triangleq \exp\left[-\frac{1}{\sigma_w^2}\mathrm{Re}\left\{G_{i,j}x_j x_i^*\right\}\right] , \tag{4.6}$$

and we use the Bayes rule in order to express the a-posteriori probability of $\mathbf{x}$ given $\mathbf{y}$ in the following factored form

$$P\left(\mathbf{x}|\mathbf{y}\right) \propto P\left(\mathbf{x}\right) p\left(\mathbf{y}|\mathbf{x}\right) \propto \prod_{i=1}^{NM}\left[P\left(x_i\right) F_i\left(x_i\right) \prod_{j<i} I_{i,j}\left(x_i, x_j\right)\right] , \tag{4.7}$$

where we used the fact that the modulation symbols x_i take on values in some signal constellation $\mathcal{C}$ and are treated by the detector as i.i.d. with given (typically uniform) a-priori probability mass function $\{P(x) : x \in \mathcal{C}\}$.

In the proposed approach, the FG corresponds to the factorization in (4.7) (see the example shown in Fig. 4.1). At this point, the resulting MP-based soft-output detector follows immediately by applying the standard SPA computation rules [80]. The detailed derivation of the message computation at the function and variable nodes of the FG is given in [81], and applies directly to our setting. Here, for the sake of completeness, we just summarize the resulting algorithm. First, define $V_i\left(x_i\right)$ as the product of all messages incoming to the variable node x_i, namely

$$V_i\left(x_i\right) \triangleq P_i\left(x_i\right) F_i\left(x_i\right) \prod_{j \neq i} \nu_{i,j}\left(x_j\right) , \tag{4.8}$$

which is proportional to the (estimated) a-posteriori probability $P\left(x_i|\mathbf{y}\right)$ and thus provides the soft-output of this detector. Then, the application of the SPA leads to the following rules for message exchange and update:

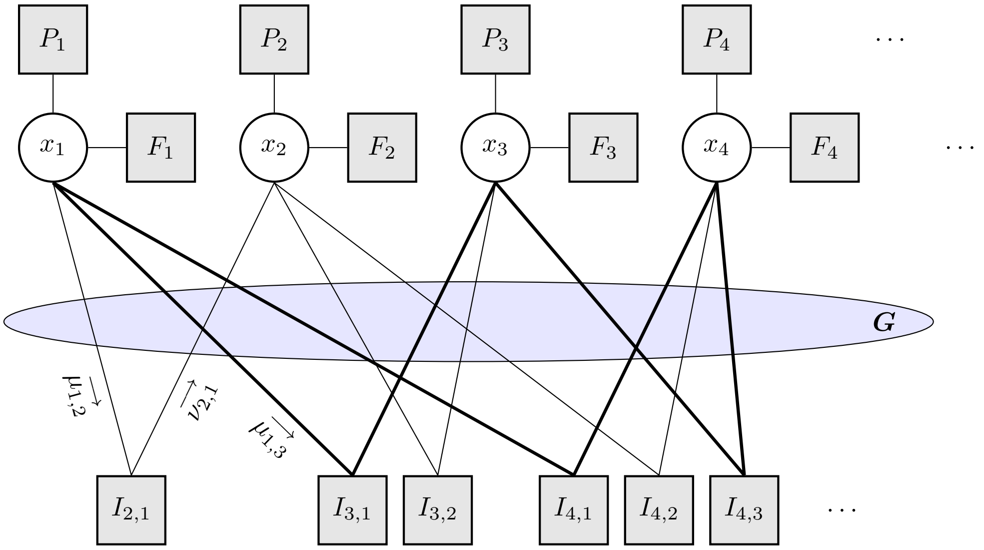

Figure 4.1: Partial structure of the FG for the $\mathrm{MP}_{\mathbf{G}}$ algorithm.

1. Computation at the variable nodes: each node x_i sends to each adjacent function node $I_{i,j}$ the message
$$\mu_{i,j}\left(x_i\right) = V_i\left(x_i\right)/\nu_{i,j}\left(x_i\right). \tag{4.9}$$
2. Computation at the function nodes: each function node $I_{i,j}$ sends to each adjacent variable node x_i the message
$$\nu_{i,j}\left(x_i\right) = \sum_{x_j \in \mathcal{C}} I_{i,j}\left(x_i, x_j\right)\mu_{i,j}\left(x_j\right)\ . \tag{4.10}$$

Notice that all the variable nodes and the function nodes can be activated in alternative rounds and, in each round, all the nodes of the same type can be activated independently and in parallel, e.g., adopting the same flooding schedule used for LDPC decoding [83]. Moreover, messages can be implemented in the logarithmic domain [80].

With the help of Fig. 4.1, we can illustrate some important features of the proposed approach:

i) FG of girth 6: the FG constructed as above is guaranteed to have girth equal to 6 (highlighted in bold in Fig. 4.1). It is well-known that the SPA yields exact posterior marginalization for cycle-free FGs, and the rationale behind the use of the SPA paradigm on loopy graphs is that if the FG has large girth, the local neighborhood of each node is "tree-like" [80, 82]. In particular, cycles of length 4 should be avoided. Hence, the proposed construction following the general method of [81] yields indeed a FG better suited to the application of the iterative SPA.

ii) Computational complexity: notice that the computation in (4.6) involves the summation w.r.t. only a single discrete variable over the constellation $\mathcal{C}$. Therefore, this computation has always linear complexity in the constellation size, irrespectively on the sparsity of the channel matrix $\mathbf{\Psi}$. This allows the use of the exact SPA at fixed complexity per node, unlike the approach in [62] (see comments in Section 4.2.2).

iii) High degree of parallelization: the number of nodes of type $I_{i,j}$ depends on the number of non-zero elements in the rows of the upper triangular part of the matrix $\mathbf{G}$ (the existence of edges is evidenced by the shadowed elliptic area in Fig. 4.1). Nevertheless, as said before, these degree-2 nodes $I_{i,j}$ can be all activated in parallel. Hence, for a sufficiently large degree of parallelization, the computational *time complexity* is independent of the sparsity of the multipath channel. Notice that in modern LDPC decoding is not unlikely to find implementations with degree of parallelization of the order of 1000, which is much larger than what needed in our detector [83]. Hence, we claim that the proposed detector is very attractive from a practical implementation viewpoint.

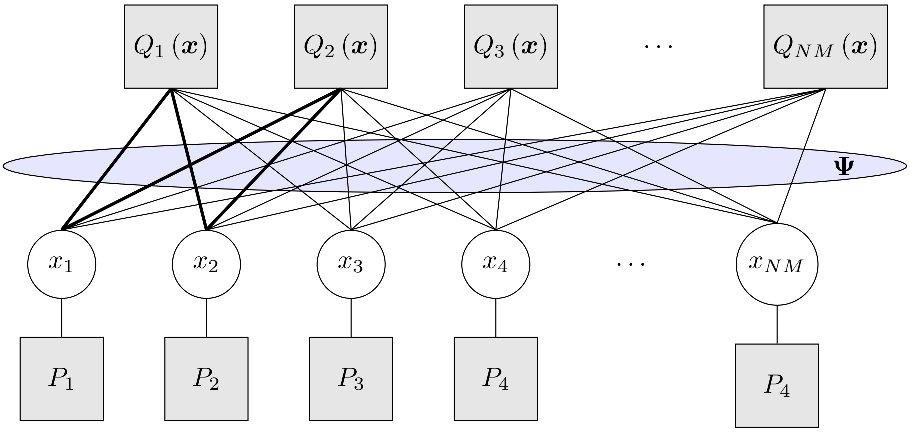

Figure 4.2: Structure of the FG for the MP$_{\boldsymbol{\Psi}}$ algorithm.

4.2.2 Another MP-based algorithm ("Matrix $\boldsymbol{\Psi}$ algorithm" — MP$_{\boldsymbol{\Psi}}$)

The MP-based algorithm of [62] builds its FG from the more "direct" factorization of the a-posteriori probability

$$P(\mathbf{x}|\mathbf{y}) \propto P(\mathbf{x})\, p(\mathbf{y}|\mathbf{x}) = \prod_{i=1}^{N\times M} p(y_i|\mathbf{x}) \prod_{i=1}^{N\times M} P(x_i)\,. \tag{4.11}$$

Defining the function nodes

$$Q_i(\mathbf{x}) \triangleq p(y_i|\mathbf{x}) = \exp\left(\frac{\|y_i - \boldsymbol{\Psi}_i\mathbf{x}\|^2}{2\sigma_w^2}\right), \tag{4.12}$$

where $\boldsymbol{\Psi}_i$ is the i-th row of $\boldsymbol{\Psi}$, the resulting FG is shown in Fig. 4.2. Since any received sample y_i depends on the entire vector of symbols $\mathbf{x}$, the FG has necessarily length-4 cycles (highlighted in bold in Fig. 4.2). The edges evidenced by the shadowed elliptic area in the figure correspond to the non-zero elements of the matrix $\boldsymbol{\Psi}$. In particular, the degree d_i of the function node $Q_i(\mathbf{x})$ is equal to the number of non-zero elements in the i-th row $\boldsymbol{\Psi}_i$. The exact SPA computation at such function nodes requires summing over $d_i - 1$

discrete variables taking values in $\mathcal{C}$. Therefore, it has a complexity equal to $|\mathcal{C}|^{d_i-1}$, where $|\cdot|$ indicates the cardinality of the set, which may be prohibitively large for large constellations and, above all, it depends on the sparsity of the channel. Therefore, the exact application of the SPA computation rules to the FG obtained directly from the matrix $\mathbf{\Psi}$ is highly impractical. For this reason, the authors of [62] propose to use a Gaussian approximation of the interfering symbols in the computation at nodes $Q_i\left(\mathbf{x}\right)$, which effectively relies to a soft interference cancellation approach, as already widely used in turbo equalization and in the context of multiuser detection in [39, 85]. The details of the resulting MP algorithm can be found in [62].

It should be also mentioned that, for the sake of simplicity and in order to increase the sparsity of the FG in Fig. 4.2, the detector proposed in [62] constructs the *nominal* matrix $\mathbf{\Psi}$ by rounding the delay shifts to integers on receiver sampling grid. Under this condition, the channel matrix is very sparse since many coefficients corresponding to sampling at non-integer delay shifts are identically to zero, and the number of connections for each node is reduced, while preserving the length-4 cycles problem, unavoidable with this approach. Nevertheless, since the assumption is generally not satisfied by real-world channels, such approximation of the channel matrix results in neglecting a significant component of the ISI. We shall verify that when such integer delay shift rounding is applied to the construction of the nominal matrix $\mathbf{\Psi}$ used by the detector but the actual delay shifts have a fractional component (as it is always the case in practice), the *mismatch* yields a significant performance degradation. This shows that neglecting the fractional part of delays and Doppler shifts, as routinely done in the literature of OTFS, may be indeed quite misleading.

4.2.3 Linear block-wise MMSE equalization

As a further term of comparison we consider also the standard linear MMSE block equalizer, applied to the channel model (2.17). In this case, the soft-output is simply the linear MMSE estimate of symbols $\mathbf{x}$ from the observation

$\mathbf{y}$, given by

$$\hat{\mathbf{x}}_{\mathrm{LMMSE}} = \mathbf{\Psi}^{\mathsf{H}} \left(\mathbf{\Psi}\mathbf{\Psi}^{\mathsf{H}} + \sigma_w^2 \boldsymbol{I}\right)^{-1} \mathbf{y} \,. \tag{4.13}$$

The complexity of this approach is proportional to $\mathcal{O}\big(\,(NM)^3\,\big)$, so it becomes quickly unfeasible for typical values of N and M. A low-complexity (mismatched) linear minimum mean square error (LMMSE) approach was recently proposed in [47], relying on the cyclic properties of channel matrix $\mathbf{\Psi}$ under perfect bi-orthogonality of shaping pulses $g_{\mathrm{tx}}(t)$ and $g_{\mathrm{rx}}(t)$, together with the assumption of on-grid Doppler and delay shifts (with Doppler-delay grid Γ). In real channel conditions, i.e., in the presence of practical rectangular pulses and non-integer delay and Doppler shifts, the performance of this approach visibly degrades.

4.3 Performance of Separated Detection and Decoding

As already mentioned, we characterize the performance of separated detection and decoding schemes in terms of pragmatic capacity, i.e., the mutual information of the virtual channel with input the constellation symbols, assumed with uniform probability, and output provided by the soft-output of the detector. This mutual information provides an achievable rate for separated detection and decoding, for any given detection scheme [78, 79].

Let us consider a sequence of symbols $\{x_k\}$ belonging to the signal constellation $\mathcal{C}$, and let $V_k(x_k)$ denotes the detector soft-output. In the case of MP-based detectors, $V_k(x_k)$ is given in the form of a posterior probability distribution on $x_k \in \mathcal{C}$, while in the case of linear equalizers (e.g., the linear MMSE estimator in (4.13)), this is given as the noisy estimate $\hat{x}_k$ which is treated as the output of a (virtual) AWGN channel. In any case, the pragmatic capacity is simply defined as the symbol-by-symbol mutual information $I_{\mathrm{PC}}\left(x_k; V(x_k)\right)$. When $V(x_k)$ takes on the form of a posterior probability distribution, this can be easily calculated as

$$\begin{aligned} I_{\mathrm{PC}}(x_k; V(x_k)) &\triangleq H(x_k) - H(x_k | V(x_k)) \\ &= \log_2 \mathcal{C} - \sum_{x_k \in \mathcal{C}} V(x_k) \log_2 \frac{1}{V(x_k)}, \end{aligned} \tag{4.14}$$

and, by considering a Monte Carlo simulation over K different realizations

$$\begin{aligned} I_{\mathrm{PC}} &= \sum_{k=0}^{K-1} H(x_k) - H(x_k | V(x_k)) \\ &= \log_2 \mathcal{C} - \frac{1}{K} \sum_{k=0}^{K-1} \left\{ \sum_{x_k \in \mathcal{C}} V(x_k) \log_2 \frac{1}{V(x_k)} \right\} . \end{aligned} \tag{4.15}$$

In the case of linear equalization (i.e., $V(x_k) = \hat{x}_k$), the pragmatic capacity is simply given by the *symmetric capacity* (i.e., with symbols used with uniform probability) of the signal constellation $\mathcal{C}$, for an AWGN channel with SNR equal to the output signal-to-interference noise ratio (SINR) of the equalizer [67]. For the sake of comparison, we also show the symmetric capacity of the signal constellation in an AWGN channel with SNR equal to $\mathrm{SNR}_{\mathrm{com}}$ (i.e., the SNR of the LoS path), denoted by $C_{\mathrm{AWGN}}^{\mathrm{sym}}$, and the mutual information with Gaussian inputs $C_{\mathrm{Gauss}}^{\mathrm{OTFS}}$, for the case $P = 1$.

Fig. 4.3 and Fig. 4.4 show the performance of the various methods for OTFS soft-output detection for a 16-quadrature amplitude modulation (QAM) and system parameters listed in Tab. 2.1. Fig. 4.3 shows the results for the (unrealistic) case where the channel Doppler shifts and delays are exactly on the discrete Doppler-delay grid Γ used by the receiver sampling. In contrast, Fig. 4.4 shows the results when the actual channel has arbitrary Doppler and delay shifts (with a random uniformly distributed fractional part), while certain algorithms still *assume* such integer grid when constructing the nominal channel matrix $\boldsymbol{\Psi}$ used by the detector (as advocated for example in [62, 47]).

We notice that the proposed MP-based approach based on the definition of matrix $\mathbf{G}$ outperforms the one in [62] in both scenarios. In particular, it

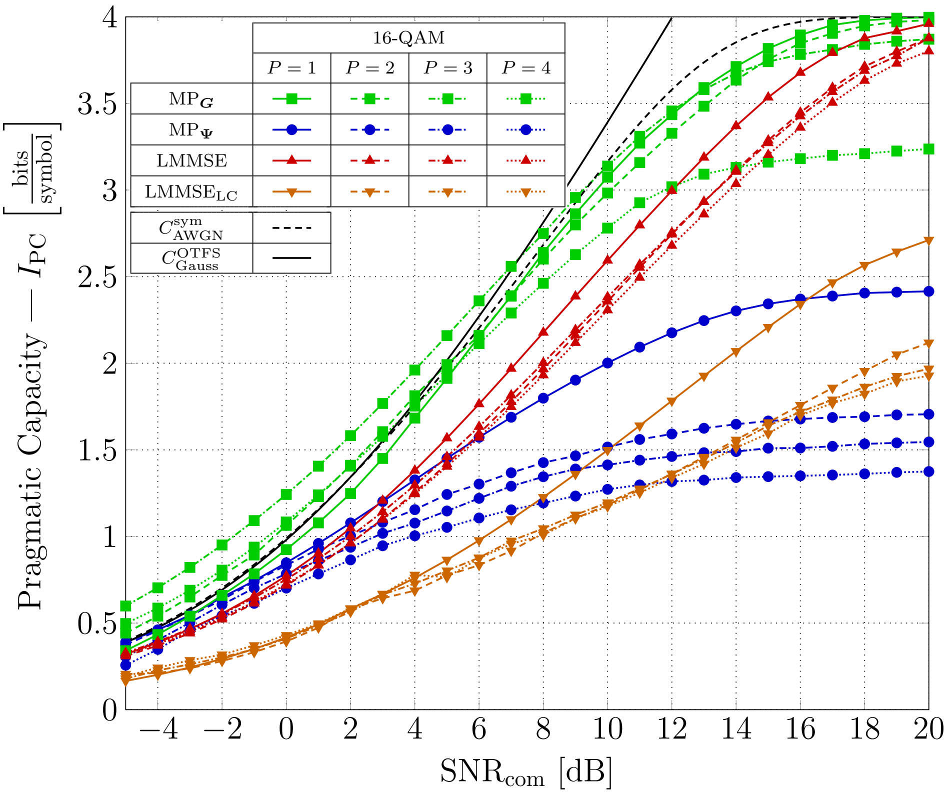

Figure 4.3: Symbols detection performance in terms of pragmatic capacity for 16-QAM modulation. The curves show the behavior of matrix **G** based MP algorithm and MP algorithm of [62] under approximated channel conditions, i.e., with delay and Doppler shifts on the Doppler-delay grid, for a multipath channel with different number of components P.

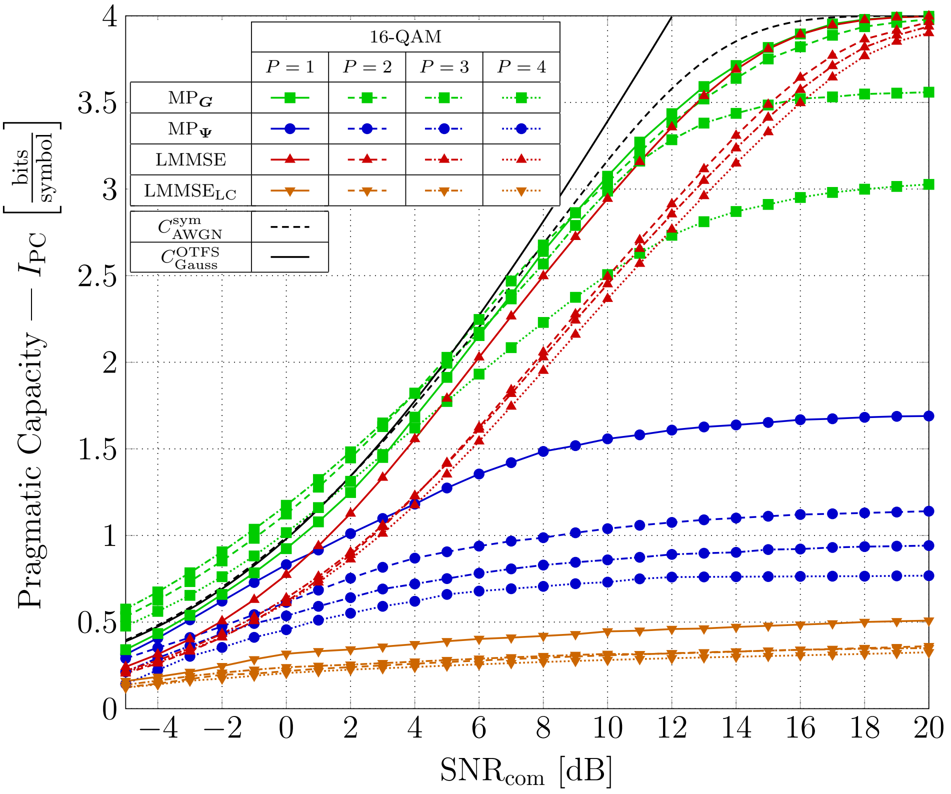

Figure 4.4: Symbols detection performance in terms of pragmatic capacity for 16-QAM modulation. The curves show the behavior of matrix $\mathbf{G}$ based MP algorithm and MP algorithm of [62] under real channel conditions, i.e., with delay and Doppler shifts not on the Doppler-delay grid, for a multipath channel with different number of components P.

suffers from almost no degradation due to the non-integer Doppler and delay shifts, unlike the method of [62], which has been derived based on these strong assumptions. The LMMSE equalizer (4.13) with full complexity yields very good performance, paying only a small SNR penalty w.r.t. the proposed MP-based scheme for $P = 1, 2$, and outperforming the MP-based scheme for richer scattering $P = 3, 4$. However, as said before, its complexity is cubic in the frame dimension NM, which is unaffordable in practical implementations. Unfortunately, the low-complexity LMMSE estimator (curves indicated by $\mathrm{LMMSE}_{\mathrm{LC}}$ in the figures), proposed in [47] and exploiting a specific structure of the channel matrix $\boldsymbol{\Psi}$, which requires doubly block circulant feature of the OTFS channel matrix, is satisfied only when $g_{\mathrm{tx}}(t)$ and $g_{\mathrm{rx}}(t)$ are bi-orthogonal. Under such condition, as demonstrated in [47], this scheme coincides with the MMSE block equalizer, but without the need of a large matrix inversion. However, by adopting physically realizable and realistic rectangular pulses, which clearly do not satisfy the bi-orthogonal condition the doubly block circulant feature is lost. Thus, our simulations show that the approach [47] is not competitive when applied to a channel model using rectangular pulses, as intuitively expected. It should be noticed that bi-orthogonality for pulses with time-frequency product equal to 1 is mathematically impossible [84], and relaying on such assumption may be very misleading.

Note that we only treat a 16-QAM modulation. However, the results are very clear and plots with different modulation formats would have only been a confirmation of what we stated above.

Chapter 5

Channel Estimation

5.1 Introduction

In a given communication scenario, the CSI, i.e., the knowledge of the communication channel, is required at the Rx to perform coherent detection [34], i.e., to correctly demodulate the transmitted symbols based on the (known) channel transformation. The most common approach to acquire the CSI is through the transmission of known symbols, usually called pilots [34]. Generally, these pilots are arranged within the block of information symbols, following a chosen fixed pattern known to both Tx and Rx (see e.g, [35, 36, 86]), in such a way when a complete block is received, the Rx is able to instantly perform coherent detection, for instance, without waiting for some other side information from another source.[1] It is also well-known that, subject to the meaningful and widely used assumption of *block fading* (i.e., the propagation channel remains constant over blocks of consecutive time-domain symbols, while it may change

---

[1] In some communication scenarios (or standard) the Tx could send an entire block of pilot symbols, i.e., without information data, followed by blocks with no pilots. Under the assumption of slowly varying channel statistics, the symbol detection is based on the estimation made from the first block. This case has not bee considered, by focusing on a *per block* channel estimation, with associated benefits and losses.

independently from block to block), pilot-aided schemes are indeed nearly information-theoretically optimal in terms of the capacity scaling in the high spectral efficiency / high SNR regime (see, e.g., [87, 88, 89, 90]). Clearly, depending on the particular application and communication scenario, both the pilot pattern and the channel estimation algorithm should be optimized. As typical electronic systems are affected by thermal noise, the estimated CSI is not perfect but afflicted by an estimation error, whose magnitude depends on different parameters, e.g., the channel SNR, the number of pilots per block, the estimation algorithm (with related convergence speed, complexity, accuracy). The estimated communication channel expression is thus used to perform coherent detection at the Rx side. By taking the achievable communication rate as the most relevant and meaningful performance metric, which is a measure of the amount of useful information sent in a block of symbols, a tradeoff appears between the number of pilots per block, dedicated to the CSI estimation, and the number of information-bearing symbols. The optimization of this tradeoff is generally not trivial, depending on the modulation format and on the channel propagation characteristics, and its optimization is usually performed by trials, given the difficulty to find closed-form optimization criteria, as done in our successive analysis.

Given the aforementioned system setup and related problems and challenges, we analyse the symbol detection performance in terms of pragmatic capacity, i.e., the achievable rate of the channel induced by the signal constellation and the detector soft-output [78, 79], of OTFS and OFDM, both designed to handle time-frequency selective channels as (1.1). This is equivalent to what is done in Chapter 4, recalled here for the sake of completeness. In general, a soft-output detector at the Rx side produces an estimate of the posterior probability of the transmitted symbols given the received signal block (pilots and data). This estimated posterior probability (e.g., in the form of log-likelihood ratios) is then passed to a decoder, that treats the sequence of soft-output symbols as the output of a *virtual channel.* The pragmatic capacity is the capacity of such virtual channel, with discrete input represented by the modulation symbols, and soft-output generated by the detector. Hence, the pragmatic capacity is representative of the achievable rate under the assumption of *separated detection and decoding*, i.e., without "turbo" reprocessing of the channel output once the decoder output is available (see, e.g., [91, 92] and references therein). In practice, iterative "turbo" detection is very hard to implement since often the detector is implemented in hardware (e.g., in an integrated circuit) and the decoder is implemented in software, and maybe even in a different location (as for example in the so-called 7.2 split between hardware and software, enabling cloud-based processing of the signals from remote radio heads [93]). For this reason, we believe that pragmatic capacity for separated detection and decoding is a very meaningful performance metric to compare different modulation formats and the associated pilot schemes and soft-output detectors.

In order to make a fair comparison between the two modulation formats in terms of achievable communication rate, the pilot overhead necessary to achieve a satisfactory estimation of the CSI has been taken into account. Since the loss (no useful information is transmitted) associated to the presence of pilots cannot be neglected, the achievable communication rate inevitably deviates from the corresponding upper bound, depicted by the AWGN symmetric capacity. Moreover, together with the pilot overhead, we also consider the (likely) presence of a guard interval (GI) or CP, which additionally reduces the achievable rate. A per-block GI is used in OTFS to avoid inter-block interference (IBI) [61], while a CP is used for every OFDM symbol to avoid ISI and to make symbols orthogonal, thanks to the diagonalization of the channel matrix, under the assumption of low ICI, condition which is not hard to be satisfied. Here a first significant difference between the two modulation formats evidently appears. In fact, especially when the channel delay is significant, the CP length tends to be a large fraction (e.g., 25%) of the symbol time, leading to a remarkable loss in terms of capacity. On the other hand, OTFS does not need a per symbol separation, but this comes at the cost of a non-negligible increase in signal processing complexity caused by the remarkable Doppler-delay

ISI, as depicted in Chapter 1 and [46].[2]

Based on the different modulation formats, distinct estimation algorithms have been adopted. For OTFS, the pilot scheme follows a similar configuration to the one proposed in [86], which considers, within the transmitted two-dimensional (Doppler-delay domain) block of symbols, a high energy center pilot (or a cluster of pilots [44], to contrast eventual destructive non-linear amplification effects over the single pilot) surrounded by pilots with magnitude sets equal to zero. This configuration of pilots and information symbols is a natural consequence of the input-output relation of OTFS, since the channel effect is a cyclic shift of the transmitted symbols of a quantity proportional to the delay and Doppler associated to each channel path. The proposed channel estimation algorithm is an extension of the ML approach of [46], also described in Chapter 1, with some improvements to reach the desired level of estimation accuracy. The idea of exploiting the channel sparsity is shared by other estimation techniques in the current literature, which generally applies concepts from compressed sensing (CS), e.g., [44, 45], but deviates from the scenario adopted in this dissertation and widely described in previous chapters. On the other hand, for OFDM we adopt a CS-based estimation algorithm. The idea of applying CS for channel estimation in multi-carrier systems is by now well established and appeared in a large number of previous work (e.g., see [38, 94, 40, 41, 42]). Here we adopt the least-absolute shrinkage and selection operator (LASSO) problem setting [95], or, equivalently, the l_1-norm regularized least squares minimization. We define a novel sensing matrix exploiting the channel sparsity, while making use of a soft-thresholding iterative algorithm [96], optimized to efficiently work in our system setup [97, 98, 99]. Because the aim of this work is the comparison between the two digital modulation formats, we are not interested in comparing the performance of the adopted estimation algorithms w.r.t. the related literature. Since every CS

---

[2] There exist OFDM-based OTFS systems, e.g., [44], which consider "OTFS-like" operations as precoding and equalization of an inner OFDM system. We will not consider such a type of systems, which deviate from the scope of this work.

problem has its own definition in terms of cost function, sensing matrix, algorithm adopted, and involved parameters, the comparison between different algorithms in literature could be not straightforward. Moreover, applied to our scenario, we do not have the certainty that algorithms in literature produce correct results, which could lead to a waste of time for a not necessary work.

It is now clear that the concept of channel sparsity is fundamental for the entire analysis. Since the properties of the communication channel represented in the Doppler-delay domain depend on the physical geometry of the environment, the scattering components are sparse in the Doppler-delay plane. Estimation algorithms built over this concept exhibit very good tradeoffs between pilot overhead, complexity, and estimation error. The cases of interest consider time-frequency varying channels, mainly targeting outdoor scenarios where the Doppler spreads are remarkable and where there are few reflectors (or group of reflectors with similar properties), and thus a small number of multipath components [4].

5.2 OFDM Modulation and the CS Algorithm

We consider OFDM modulation with CP, as described in Chapter 1, transmitted over a time-frequency selective channel, assuming perfect orthogonality and absence of ICI. The CIR in time-frequency domain, derived in Sec. 1.1 and given here for the sake of convenience, is

$$H(t,f) = \sum_{p=0}^{P-1} h_p e^{j2\pi\nu_p t} e^{-j2\pi\tau_p f} , \tag{5.1}$$

where P is the number of multipath scattering components and h_p, ν_p, and τ_p are the complex channel gain including the pathloss, the Doppler shift, and the delay, associated to the p-th scattering component, respectively. Note that, also in this configuration, we set the maximum channel delay and Doppler shift to be

$$\tau_{\max} < T , \quad \nu_{\max} < \Delta f , \tag{5.2}$$

where T is the symbol time and Δf is the subcarrier spacing. By discretizing the time axis at steps nT, for $n = 0, \ldots, N-1$, and the frequency axis at steps $m\Delta f$, for $m = 0, \ldots, M-1$, i.e., emulating standard sampling operations (see Sec. 1.2), the discrete channel representation becomes

$$\mathbf{H} = \sum_{p=0}^{P-1} h_p \mathbf{a}\left(\tau_p\right) \mathbf{b}^{\mathsf{H}}\left(\nu_p\right) , \tag{5.3}$$

in which

$$\mathbf{a}\left(\tau_p\right) = \left[1, e^{j2\pi\tau_p\Delta f}, \ldots, e^{j2\pi\tau_p(M-1)\Delta f}\right]^{\mathsf{T}} , \tag{5.4}$$

$$\mathbf{b}\left(\nu_p\right) = \left[1, e^{j2\pi\nu_p T}, \ldots, e^{j2\pi\nu_p(N-1)T}\right]^{\mathsf{T}} , \tag{5.5}$$

where $(\cdot)^{\mathsf{T}}$ and $(\cdot)^{\mathsf{H}}$ denote the transpose and the conjugate transpose (Hermitian) operation, respectively. By representing the information symbols $\{x_{n,m}\}$, belonging to any complex modulation alphabet, arranged in a $N \times M$ grid, i.e., in matrix form $\mathbf{X}$, the expression of the received samples after transmission over the discrete channel in (5.3) is

$$\mathbf{Y} = \mathbf{X} \odot \mathbf{H} + \mathbf{Z} , \tag{5.6}$$

where $\odot$ is the element-wise multiplication and $\mathbf{Z}$ is the AWGN with zero mean and covariance matrix $\sigma^2 \mathbf{I}_{NM}$.

At this point, let us represent the channel in a different form. Suppose to define a Doppler-delay grid Γ,[3] with some grid steps (both in the Doppler and delay domain) and total dimension G, given by the product between Doppler and delay axis dimensions. For each grid point $\gamma_i \in \Gamma$, for $i = 0, \ldots, G-1$, by neglecting the complex gain and the multipath components, which will be inserted later in another form, the channel can be expressed, similarly to (5.3), as

$$\tilde{\mathbf{H}}\left(\gamma_i\right) = \mathbf{a}\left(\tau\left(\gamma_i\right)\right) \mathbf{b}^{\mathsf{H}}\left(\nu\left(\gamma_i\right)\right) , \tag{5.7}$$

---

[3] Here, the Doppler-delay grid Γ corresponds to the one defined in (1.13), for the sake of simplicity of treatment, but that definition is not mandatory.

in which $\tau(\gamma_i)$ and $\nu(\gamma_i)$ are two fixed values of delay and Doppler depending on the discretization point γ_i. By stacking the $N \times M$ matrices $\tilde{\mathbf{H}}(\gamma_i)$ to column vectors for all points $\gamma_i \in \Gamma$ (vec$(\cdot)$ operator) and concatenating the obtained vectors, we create

$$\mathbf{D} = \left[\operatorname{vec}\left(\tilde{\mathbf{H}}(\gamma_0)\right), \ldots, \operatorname{vec}\left(\tilde{\mathbf{H}}(\gamma_{G-1})\right)\right], \tag{5.8}$$

of dimension $NM \times G$. Now, the complex gain and the multipath components omitted in (5.7) should be somehow inserted. For this purpose, we make use of a vector, namely $\mathbf{h}_{\text{sp}}$ (read: "*h-sparse*"), representing the channel gains spread over the dimension G. Thus, the approximated channel matrix in vector form $\bar{\mathbf{h}}$ takes the form

$$\bar{\mathbf{h}} \simeq \mathbf{D}\mathbf{h}_{\text{sp}}, \tag{5.9}$$

in which $\mathbf{h}_{\text{sp}}$ is a sparse vector of the form

$$\mathbf{h}_{\text{sp}} = \left[0, \ldots, 0, \bar{h}_0, 0, \ldots, 0, \bar{h}_1, 0, \ldots, 0, \bar{h}_2, 0, \ldots\right]^{\mathsf{T}}, \tag{5.10}$$

where the positions of the approximated (to the nearest grid step of grid Γ) channel coefficients $\bar{h}_i$ select the columns of $\mathbf{D}$ with the channel coefficients pair $(\tau(\gamma_i), \nu(\gamma_i))$, to overall represent the triplet $\left(\tau(\gamma_i), \nu(\gamma_i), \bar{h}_p\right)$ emulating the true channel parameters (τ_p, ν_p, h_p). Thus, the approximated received samples expression, by stacking the $N \times M$ matrices to column vectors of length NM, can be written as

$$\bar{\mathbf{y}} = \mathbf{x} \odot \mathbf{D}\mathbf{h}_{\text{sp}} + \mathbf{z}, \tag{5.11}$$

where $\mathbf{x} = \operatorname{vec}(\mathbf{X})$ and $\mathbf{z} = \operatorname{vec}(\mathbf{Z})$. Moreover, by defining a selection matrix $\mathbf{S}$, of dimension $|\mathcal{P}| \times NM$, to choose $|\mathcal{P}|$ symbols (pilots) among the total NM ($\mathcal{P}$ is the set of pilots and $|\cdot|$ indicates its cardinality), the transmitted vector of pilots $\mathbf{x}_{\text{pl,OFDM}}$ (read: "*x-pilot*") takes the form

$$\mathbf{x}_{\text{pl,OFDM}} = \mathbf{S}\mathbf{x}, \tag{5.12}$$

and

$$\bar{\mathbf{y}}_{\text{pl}} = \mathbf{x}_{\text{pl,OFDM}} \odot \mathbf{S}\mathbf{D}\mathbf{h}_{\text{sp}} + \mathbf{z}. \tag{5.13}$$

The estimation of the channel coefficients can be carried on by solving the problem known as LASSO [95], i.e.,

$$\hat{\mathbf{h}} = \arg\min_{\mathbf{h}} \left\|\mathbf{y}_{\mathrm{pl}} - \mathbf{x}_{\mathrm{pl,OFDM}} \odot \mathbf{SDh}\right\|_2^2 + \lambda \left\|\mathbf{h}\right\|_1 \,, \tag{5.14}$$

where $\mathbf{SD}$, under this configuration, takes the role of the sensing matrix of the CS configuration, and λ is the LASSO regularizer (see Sec. 5.2.1 for more details). Notice that $\mathbf{y}_{\mathrm{pl}}$ is obtained through the transmission over the *actual* channel, as pointed out afterwords, and thus differs from $\bar{\mathbf{y}}_{\mathrm{pl}}$ of (5.13), obtained through the process of approximation of the channel matrix described before. The goal is to keep the incurred estimation (and approximation) error between $\hat{\mathbf{h}}$ and $\mathbf{h}_{\mathrm{sp}}$ as small as possible, by choosing appropriately the grid Γ with sufficiently fine discretization. However, on the other hand, increasing the granularity of the grid Γ could lead to a remarkable increase of computational complexity. As a preview of things to come, this problem will be solved through an iterative discretization refinement, which keep the computational cost limited. In any case, the residual approximation error between $\mathbf{y}_{\mathrm{pl}}$ and $\bar{\mathbf{y}}_{\mathrm{pl}}$ is automatically included in the minimization or the overall quadratic error term $\left\|\mathbf{y}_{\mathrm{pl}} - \mathbf{x}_{\mathrm{pl,OFDM}} \odot \mathbf{SDh}\right\|_2^2$ in (5.14).

The LASSO minimization problem has been extensively studied in literature. It can be solved using many different algorithms and strategies [99, 96, 97], also adopted for the specific case of channel estimation [38]. As a final outcome, the estimated channel matrix resulting from the minimization of (5.14), used to perform coherent detection, is

$$\hat{\mathbf{H}} = \mathbf{D}\hat{\mathbf{h}} \,. \tag{5.15}$$

For completeness and for the sake of results reproducibility, the details of the used LASSO solver, together with an analysis on its complexity, are described in Sec. 5.2.1.

5.2.1 The LASSO Solver

We here give the details of the algorithm used to solve the LASSO minimization problem in (5.14).

0) *Initialization*: By defining the known support matrix $\mathbf{A} \triangleq \mathbf{X}_{\mathrm{pl}} \odot \mathbf{SD}$, in which $\mathbf{X}_{\mathrm{pl}}$ is a matrix of dimension $|\mathcal{P}| \times G$ composed of G equal vectors $\mathbf{x}_{\mathrm{pl}}$, i.e., $\mathbf{X}_{\mathrm{pl}} \triangleq [\mathbf{x}_{\mathrm{pl}}, \ldots, \mathbf{x}_{\mathrm{pl}}]$, let $\mathbf{\Lambda} \triangleq \mathbf{A}^{\mathsf{H}}\mathbf{A}$ and initialize the step size ε as [96]
$$\varepsilon \triangleq \frac{1}{\|\mathbf{\Lambda}^{\mathsf{H}}\mathbf{\Lambda}\|_{\mathrm{F}}} = \frac{1}{\sqrt{\mathrm{trace}\left(\mathbf{\Lambda}^{\mathsf{H}}\mathbf{\Lambda}\right)}} , \tag{5.16}$$
in which $\|\cdot\|_{\mathrm{F}}$ indicates the Frobenius norm and the trace$(\cdot)$ operation takes the sum of the matrix main diagonal elements. The threshold t is set as $t = \lambda\varepsilon$, where λ is the LASSO regularizer appearing in (5.14). The vector of estimated values $\hat{\mathbf{h}}$ is initialized to all zeros.

1) *Iterations* $i = 1, 2, \ldots$

    (a) *Soft Thresholding*: with $\psi_{\mathrm{st}}(\cdot, t)$ soft thresholding operator with threshold t (see [96] and Appendix 5.2.1.2), computes
    $$\boldsymbol{\beta}^{i+1} = \psi_{\mathrm{st}}\left(\hat{\mathbf{h}}^{i} + \varepsilon\mathbf{A}^{\mathsf{H}}\left(\mathbf{y} - \mathbf{A}\hat{\mathbf{h}}\right), t\right) . \tag{5.17}$$

    (b) *Nesterov's Acceleration Factor (Optional)* [96]: Introduce a tuning coefficient $\alpha_i \in [0, 1]$, which can be fixed or variable in t, and computes
    $$\hat{\mathbf{h}}^{i+1} = \boldsymbol{\beta}^{i+1} + \alpha_i\left(\boldsymbol{\beta}^{i+1} - \hat{\mathbf{h}}^{i}\right) , \tag{5.18}$$
    with α_i defined, e.g., in [96, 97, 98].

    (c) *Shrink*: Remove the entries of $\mathbf{y}$ and $\boldsymbol{\beta}$, the columns of $\mathbf{A}$, and the entries of $\hat{\mathbf{h}}$, corresponding to the zero entries of $\hat{\mathbf{h}}$.

2) *Restoring*: Restore the estimated vector $\hat{\mathbf{h}}$ to its full dimension (this operation is necessary after the shrink of the vectors during the iterations).

We used as stopping criterion the maximum number of iterations. Note that the shrinking operation is allowed because zero entries of vector $\hat{\mathbf{h}}$ at iteration i cannot assume a value $\neq 0$ at iteration $i' > i$ [99]. From a complexity point of view, the first iterations are the most costly, while the algorithm can run $> 10^6$ times keeping the complexity almost constant and the computational time linear (when the number of iterations is large enough, i.e., far away from starting costly ones).

5.2.1.1 Complexity of the LASSO Solver and Step Size Refinement

The sensing matrix $\mathbf{D}$ is composed of G columns of length NM. While the dimensions N and M depends on system settings and can be somehow controlled or tuned, the dimension G takes into account the estimation precision, or granularity, of the searching grid Γ. Hence, the larger the dimension G, the more reliable the result. Using some examples:

- If Γ is equivalent to the Doppler-delay grid (delay and Doppler shifts integer multiple of the grid), $G = NM$ and $\mathbf{D}$ is a $NM \times NM$ matrix. Blockwise operations adopted by any LASSO solver are feasible in this framework.
- If the step size for both Doppler and delay axis is a fraction $1/\rho$ of the Doppler-delay grid step, $G \simeq O\left(NM \cdot \rho^2\right)$ and $\mathbf{D}$ is approximately a $NM \times \left(NM \cdot \rho^2\right)$ matrix. Clearly, increasing the granularity of the grid quickly increases the complexity.

In order to overcome the complexity induced by searching grid with fine granularity, it is possible to refine the step size in successive phases, rather than directly defining a low fractional value for the entire grid. The proposed refinement scheme is illustrated in Algorithm 3. During the *Peak Selection* step, if the number of multipath components P is not available at the receiver, instead select all local maxima or peaks (of the groups of estimates) whose magnitude is above a certain threshold (to be defined).

```
Algorithm 3: Refinement of the Granularity
Result: Fine estimation $\hat{\mathbf{h}}$ for LASSO problem (5.14).
Coarse Estimation: For any LASSO solver, get a first coarse
  estimation $\hat{\mathbf{h}}$ such that the searching grid $\Gamma$ is equivalent to the
  Doppler-delay grid (i.e., delay and Doppler shifts integer multiple of the
  grid). In this case $G = NM$ and $\mathbf{D}$ is a $NM \times NM$ matrix;
For Iteration $i = 1, 2, \dots$ do
    • Peak Selection: Select the first $P$ local maxima of $\hat{\mathbf{h}}$;
    • Step Refinement Around Maxima: Build a new sensing matrix
      based on an extension of matrix $\mathbf{D}$ such that the step size around
      the peaks is decreased (i.e., the granularity and the precision are
      increased);
    • Finer Estimation: For any LASSO solver, get a finer estimation
      $\hat{\mathbf{h}}$.
End
```

Note that during the *Coarse Estimation* step, i.e., when $\mathbf{D}$ is an $NM \times NM$ matrix, it is possible to adopt the approach proposed in [100] to solve the LASSO minimization in (5.14). The algorithm of [100], benefiting of the hierarchical structure of vector $\mathbf{h}$, is able to provide a first coarse and reliable estimation optimizing the computational complexity. However, if $\mathbf{h}$ takes off-grid values, the approach of [100] becomes inappropriate, as confirmed by the presented simulation results. For this reason, after a *Coarse Estimation*, i.e., within the *Iteration* step, another LASSO solver must be chosen to obtain the best performance in terms of channel estimation.

5.2.1.2 Soft-Thresholding Operator

In order to solve the LASSO minimization problem, a soft thresholding operator is used in (5.17). The choice of this function is justified in the following.

By starting from the input-output relation in matrix form

$$\mathbf{y} = \mathbf{x} \odot \mathbf{SDh} + \mathbf{z} \triangleq \mathbf{Ah} + \mathbf{z} \,, \tag{5.19}$$

the residual sum of squares (RSS) for the LASSO solver is given by

$$\mathrm{RSS}\left(\mathbf{h}\right) = \frac{1}{2} \sum_{i=0}^{NM-1} \left[y_i - \sum_{j=0}^{G-1} h_j A_{i,j} \right]^2 + \lambda \sum_{j=0}^{G-1} \left| h_j \right| \,. \tag{5.20}$$

By taking the derivative of the first and second terms of the RSS w.r.t. θ_k we get

$$\begin{aligned} &\frac{\partial}{\partial h_k} \left\{ \frac{1}{2} \sum_{i=0}^{NM-1} \left[y_i - \sum_{j=0}^{G-1} h_j A_{i,j} \right]^2 \right\} \\ &= - \sum_{i=0}^{NM-1} A_{i,k} \left[y_i - \sum_{\substack{j=0 \\ j \neq k}}^{G-1} h_j A_{i,j} \right] + h_k \sum_{i=0}^{NM-1} A_{i,k} \\ &\triangleq -\rho_k + h_k \eta_k \,, \end{aligned} \tag{5.21}$$

$$\frac{\partial}{\partial h_k} \left\{ \lambda \sum_{j=0}^{G-1} \left| h_j \right| \right\} = \begin{cases} -\lambda & \text{if } h_k < 0 \\ [-\lambda,\, \lambda] & \text{if } h_k = 0 \\ \lambda & \text{if } h_k > 0 \end{cases} \,, \tag{5.22}$$

in which the derivative at $h_k = 0$ can assume two different values. By putting things together

$$\frac{\partial \mathrm{RSS}\left(\mathbf{h}\right)}{\partial h_k} = -\rho_k + h_k \eta_k + \frac{\partial}{\partial h_k} \lambda \left| h_k \right| \,, \tag{5.23}$$

and, by setting the derivative equal to zero (since we are trying to minimize the LASSO cost function)

$$\frac{\partial \mathrm{RSS}\left(\mathbf{h}\right)}{\partial h_k} = 0 = \begin{cases} -\rho_k + h_k \eta_k - \lambda & \text{if } h_k < 0 \\ [-\rho_k - \lambda,\, -\rho_k + \lambda] & \text{if } h_k = 0 \\ -\rho_k + h_k \eta_k - \lambda & \text{if } h_k > 0 \end{cases} \,. \tag{5.24}$$

We must ensure that the closed interval $[-\rho_k - \lambda,\, -\rho_k + \lambda]$ contains the zero such that h_k is a global minimum, i.e.,

$$0 \in [-\rho_k - \lambda,\, -\rho_k + \lambda] \Rightarrow -\lambda \leq \rho_k \leq \lambda\,. \tag{5.25}$$

Thus, finally

$$\psi_{\mathrm{st}}\left(h_k, \lambda\right) = \begin{cases} (\rho_k + \lambda)/\eta_k & \text{if } \rho_k < -\lambda \\ 0 & \text{if } -\lambda \leq \rho_k \leq \lambda \\ (\rho_k - \lambda)/\eta_k & \text{if } \rho_k > \lambda \end{cases}\,, \tag{5.26}$$

which is the soft thresholding operator $\psi_{\mathrm{st}}\left(h_k, \lambda\right)$ with normalization constant $1/\eta_k$.

5.2.1.3 Nesterov's Acceleration Factor

The Nesterov's acceleration factor governs the dependency between two successive estimations, while remarkably reducing the convergence time of the algorithm [97]. The choice of the optimization coefficient α_i is not mandatory. By following the pioneering work [98], which inspired many other works, e.g., [96], α_i can be recursively defined as

$$\xi_{i+i} = \frac{1 + \sqrt{4\xi_i^2 + 1}}{2}\,, \tag{5.27}$$

$$\alpha_i = \frac{\xi_i - 1}{\xi_{i+i}}\,, \tag{5.28}$$

with $\xi_0 = 1$. Another choice simply based on the iteration index i is $\alpha_i = (i-1)/(i+2)$ [97, 98]. Both solutions describe a curve growing from an initial value ("far" from 1) up to 1. The associated plots, with their similar behaviors, can be seen in Fig. 5.1. The most conservative choice is $\alpha_i = 1$, for which the dependency from the previous estimated values is maximized, while the less conservative choice is $\alpha_i = 0$, completely forgetting the previous estimated values. Intuitively, a small value of α_i is preferable for the first noisy iterations,

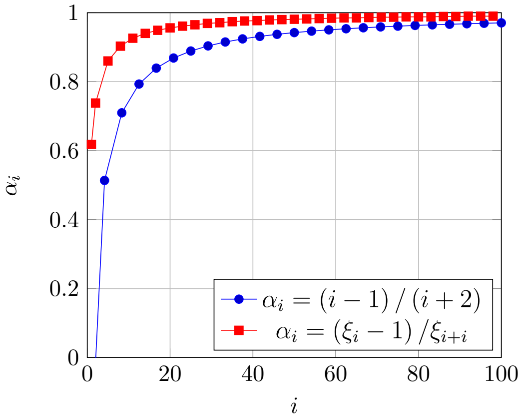

Figure 5.1: The evolution of α_i over iterations i for different approaches.

while a parameter α_i near to one should be chosen when the reliability of the estimation increases.

5.2.2 Pilot Scheme

The optimization of a deterministic sensing matrix for CS configurations, such as LASSO, is up to now one of the most studied open problems in CS theory. In fact, the typical performance guarantees of CS require properties such as the restricted isometry property [101, 38], for which explicit constructions are not available and even checking the property for a given randomly generated matrix is exponentially complex [102]. On the other hand, ensembles of randomly generated matrices have the property of satisfying these properties with high probability [38]. Hence, here we resort to a pseudo-random pilot placement on the 2-dimensional time-frequency grid of transmitted symbols. Simulation results have shown that such random placement achieves with high probability the best performance w.r.t. regular “lattice” placements (e.g., equally spaced combinations of subcarriers or time slots), as usually specified in wireless standards [36]. An example of a random pilot scheme is depicted in Fig. 5.2. Moreover, generally, distinct configurations of a fixed number of

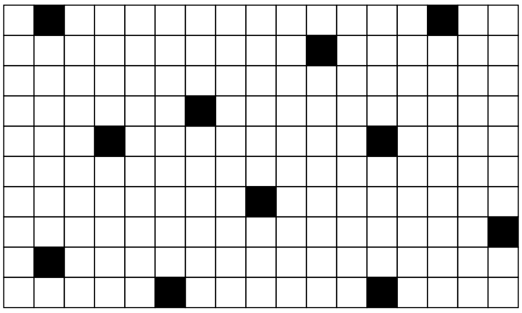

Figure 5.2: Example of a random pilot scheme for OFDM modulation.

pilots, randomly placed within the 2-dimensional grid, provides similar performance in terms of channel estimation. If pilots are not placed randomly but follow some periodic pattern, the algorithm for solving the LASSO produces far inferior results. This behavior is caused by the periodic sampling of a random Fourier matrix (i.e., $\mathbf{H}$ or $\mathbf{D}\mathbf{h}_{\mathrm{sp}}$). This is the reason why commonly used pilot schemes (see, e.g., [36] and references therein), generally structured or periodic, are not suitable for the CS-based estimation of OFDM systems (assuming that the OFDM channel is represented by a Fourier matrix). Overall, the aim it to maximize the overall achievable rate under random pilot placement. Hence, we can optimize the number of pilots per block to seek the optimal tradeoff between CSI estimation quality and pilot overhead (see (5.41) in the following and numerical results in Sec. 5.4).

5.2.3 Received Samples Expression — Real and Approximated Channel Conditions

Without entering into details of the complete input-output derivation of a CP OFDM system which can be found in Section 1.2, we only provide the received sample expression, which is

$$y\left[n,m\right]=\frac{1}{M}\sum_{p=0}^{P-1}h_{p}e^{j2\pi\nu_{p}nT}\sum_{m'=0}^{M-1}x\left[n,m'\right]e^{-j2\pi m'\Delta f\tau_{p}}\sum_{i=0}^{M-1}e^{j2\pi\frac{i}{M}\frac{\nu_{p}}{\Delta f}}e^{j2\pi\frac{i(m'-m)}{M}} \tag{5.29}$$

$$\approx\frac{1}{M}\sum_{p=0}^{P-1}h_{p}e^{j2\pi\nu_{p}nT}\sum_{m'=0}^{M-1}x\left[n,m'\right]e^{-j2\pi m'\Delta f\tau_{p}}\sum_{i=0}^{M-1}e^{j2\pi\frac{i(m'-m)}{M}}$$

$$=\sum_{p=0}^{P-1}h_{p}e^{j2\pi\nu_{p}nT}e^{-j2\pi\tau_{p}m\Delta f}x\left[n,m\right]\ . \tag{5.30}$$

By considering real and approximated channel conditions, the received samples at time instant n and subcarrier m are respectively given by (5.29) and (5.30), in which the ICI-free approximation follows the assumption $\nu_{\max}/\Delta f \ll 1$, and the last equality follows by using the orthogonality property. Note that the expression (5.30) is equivalent to (5.6), meaning that the ICI-free assumption has been taken into account for the algorithmic design. When comparing OTFS and OFDM, the channel model in (5.30) is considered, such that the absence of ICI assumption holds. However, by focusing the attention on OFDM only, the performance comparison is extended to the case of real channel conditions, i.e., with input-output relation (5.29), showing the performance degradation when the ICI-free assumption is far to be satisfied. Clearly, a similar analysis for OTFS is meaningless, being the waveform not sensitive to the magnitude of delay and Doppler shifts.

5.3 OTFS Modulation and the Proposed Estimation Algorithm

By neglecting, but keeping in mind, the complete derivation of the OTFS input-output relation, which can be found in Chapter 1, we can proceed further describing the channel estimation procedure, which is inspired by [86]. The input-output relation expressed in matrix, shown the first time in (1.44), is reported here for convenience

$$\mathbf{y} = \left(\sum_{p=0}^{P-1} h_p \mathbf{\Psi}_p \right) \mathbf{x} + \mathbf{z} \,, \tag{5.31}$$

where $\mathbf{z}$ denotes the AWGN with zero mean and covariance matrix $\sigma^2 \mathbf{I}_{NM}$. Note that $\mathbf{\Psi}_p$ implicitly takes into account a Doppler-delay pair (τ_p, ν_p), i.e., $\mathbf{\Psi}_p \triangleq \mathbf{\Psi}_p(\tau_p, \nu_p)$. Without entering into mathematical details which can be found in Sec. 1.3, the effect of the channel to symbols arranged in blocks is shortly described in the following.

Consider a block composed by all zero magnitude symbols but one non-zero, having enough energy to be well distinguishable, w.r.t. to the noise floor, and positioned anywhere within the block. Note that the position of the symbol does not influence the result, since the channel shift effect is circular within the block, as proved by the results of Sec. 1.3. This block is thus transmitted over the time-frequency selective channel in (5.3). At the Rx, most of the energy concentrates in a point of the block (or, more precisely, a point per multipath component), while dissipating to the surrounding positions, according to Fig. 1.4, where and example of blocks of transmitted symbols and received samples blocks are depicted. The intuitive estimation of the pairs (τ_p, ν_p), for each multipath component, follows by searching the peaks within the received samples grid, successively associated to an estimate $(\hat{\tau}_p, \hat{\nu}_p)$ (as suggested in [86]). However, this intuitive estimation procedure is only able to provide the integer parts of the Doppler and delay shifts, associated to the Doppler-delay grid point, where a peak is detected, collecting enough energy. The fractional parts of delay and Doppler shifts are, instead, associated to the dissipation of the energy around the peak points (see Fig. 1.4), and have to be treated and analyzed separately.

The approximation of the channel behavior to integer Doppler and delay shifts, as done in [86], allows this intuitive estimation procedure to work correctly, but only under such non-realistic channel conditions. Thus, based on the ML estimator proposed in Sec. 1.3, the idea of [86] is extended, and a

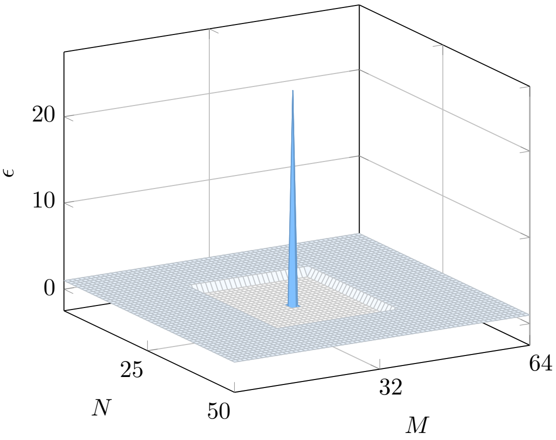

Figure 5.3: Example of a pilot scheme for OTFS modulation. Within the block of dimension $N \times M$ the centered pilot with high energy ε is well distinguishable, and surrounded first by zero pilots (the hollow zone) and after by information symbols (here, for convenience, with unit energy).

reliable estimation algorithm working under realistic channels is provided.

5.3.1 Pilot Scheme

A block of $N \times M$ transmitted symbols contains both information bearing symbols and pilots. The arrangement of pilots consists of a rectangular region placed within the block (not necessarily in the middle, since the channel effect is circular) containing two types of symbols (see Fig. 5.3):

- *Zero Pilots*: Placed between information symbols and non-zero pilots to guarantee as less interference as possible between them. The Dirichlet kernel functions appearing in the OTFS input-output relation (see Sec. 1.3 and in particular (1.44)) are rapidly decreasing non-negative functions (see Fig. 1.3 and 1.5), hence, perfect orthogonality between information symbols and pilots cannot be achieved, but, at least, the Doppler-delay ISI can be reduced.

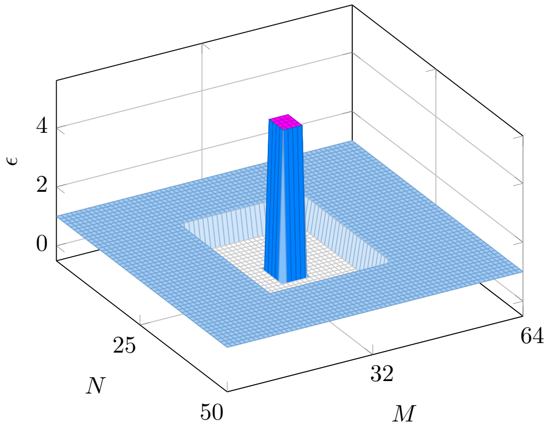

Figure 5.4: Example of a pilot scheme for OTFS modulation. Within the block of dimension $N \times M$ the plateau of pilots with high energy ε is well distinguishable, and surrounded first by zero pilots (the hollow zone) and after by information symbols (here, for convenience, with unit energy).

- *Peak Pilot*: A single pilot symbol with high energy, collecting the energy of all zero pilots, is placed at the grid center. Its shifts in the Doppler-delay grid are used to provide the initial coarse estimation of the Doppler-delay pairs, which results to be fast and simple.

Given this pilot arrangement, the number of pilot symbols has to be optimized to match the optimal performance-overhead tradeoff, while keeping constant the total block energy.

Given some particular system setups, such as communication including non-linear amplifier not constant channel behaviours over block symbols in time, basing the estimation algorithm on just one symbol (the peak pilot) could not be a safe approach. In such cases, the pilot scheme can be extended, for instance, by considering a rectangular region composed of zero pilots and a plateau on non-zero pilots (see Fig. 5.4), instead of just the peak pilot. We would like to stress the fact that the successive algorithm design is not only suitable for the aforementioned pilot configuration, but is able to provide reliable and remarkable performance under any other pilot configuration. Clearly, this necessitates test scenarios and simulation results, which are omitted in this work.

Note that in OFDM, symbols are independent, i.e., ISI and ICI free for modulation definition, and the pilot vector $\mathbf{x}_{\text{pl,OFDM}}$, defined in (5.12) through a selection matrix $\mathbf{S}$, results to be a subset of symbols $\mathbf{x}$. Differently, in OTFS, since the channel, as depicted in Fig. 1.4, behaves *per block* and not *per symbol* as in OFDM, the processing at the Rx could not be based on a subset of samples but must take into account the entire block. As a results, the vector of pilots $\mathbf{x}_{\text{pl,OTFS}}$ has dimension $NM \times 1$ and is composed of all zero entries (the positions of unknown data symbols are set to zero) but one, i.e., the peak pilot (Fig. 5.3).

5.3.2 Channel Estimation

The proposed channel estimation scheme is based on the ML approach of Sec. 2.1.2 and presented in [46],[4] providing a parameter estimation of Doppler, delay, and complex channel gain associated to each multipath component.

The following ML derivation is basically what has been already derived in Sec. 2.1.2, but with some new details and modifications. The objective is to estimate the set of parameters $\boldsymbol{\theta} = \{h'_p, \tau_p, \nu_p\} \in \mathcal{T}^P$, with $\mathcal{T} = \mathbb{C} \times \mathbb{R} \times \mathbb{R}$. By defining the ML function as

$$l(\mathbf{y}|\boldsymbol{\theta}, \mathbf{x}_{\text{pl,OTFS}}) = \left| \mathbf{y} - \sum_p h'_p \boldsymbol{\Psi}_p \mathbf{x}_{\text{pl,OTFS}} \right|^2 , \tag{5.32}$$

---

[4] In [46] a ML method to estimate the Doppler shift and delay of the main path has been proposed, by assuming LoS in the backscattered wave for a joint radar and communication application with OTFS modulation format. Since in [46] the estimation of the radar parameters is performed at the Tx side (colocated with the Rx), all modulation symbols in the block are known (see Sec. 2.1.2). Therefore, they can be all treated as pilot symbols. Here we use the same ML approach, but applied to a specific pilot pattern.

the ML solution becomes

$$\hat{\boldsymbol{\theta}} = \arg \min_{\boldsymbol{\theta} \in \mathcal{T}^P} l(\mathbf{y}|\boldsymbol{\theta}, \mathbf{x}_{\text{pl,OTFS}}). \tag{5.33}$$

For a fixed set of $\{\tau_p, \nu_p\}$, the ML estimator of $\{h'_p\}$ is given by solving the following set of equations

$$\mathbf{x}_{\text{pl,OTFS}}^{\mathsf{H}} \boldsymbol{\Psi}_p^{\mathsf{H}} \left(\sum_{q=0}^{P-1} h'_q \boldsymbol{\Psi}_q \right) \mathbf{x}_{\text{pl,OTFS}} = \mathbf{x}_{\text{pl,OTFS}}^{\mathsf{H}} \boldsymbol{\Psi}_p^{\mathsf{H}} \mathbf{y} \,. \tag{5.34}$$

By plugging (5.34) into (5.32), it readily follows that minimizing $l(\mathbf{y}|\boldsymbol{\theta}, \mathbf{x}_{\text{pl,OTFS}})$ reduces to maximize

$$\begin{aligned} l_2(\mathbf{y}|\boldsymbol{\theta}, \mathbf{x}_{\text{pl,OTFS}}) &= \sum_p h'_p \mathbf{y}^{\mathsf{H}} \boldsymbol{\Psi}_p \mathbf{x}_{\text{pl,OTFS}} \\ &= \sum_p S(\tau_p, \nu_p) - I_p(\{h'_q\}_{q \neq p}, \boldsymbol{\theta}) \,, \end{aligned} \tag{5.35}$$

where $S(\tau_p, \nu_p, \phi_p)$ and $I_p(\{h'_q\}_{q \neq p}, \boldsymbol{\theta})$ (S_p and I_p in short hand notation) denote the useful signal and the interference term for the multipath component p, given respectively by

$$S_p = \frac{|\mathbf{y}^{\mathsf{H}} \boldsymbol{\Psi}_p \mathbf{x}_{\text{pl,OTFS}}|^2}{|\boldsymbol{\Psi}_p \mathbf{x}_{\text{pl,OTFS}}|^2} \,, \tag{5.36}$$

$$I_p = \frac{(\mathbf{y}^{\mathsf{H}} \boldsymbol{\Psi}_p \mathbf{x}_{\text{pl,OTFS}}) \, \mathbf{x}_{\text{pl,OTFS}}^{\mathsf{H}} \left(\boldsymbol{\Psi}_p^{\mathsf{H}} \sum_{q \neq p} h'_q \boldsymbol{\Psi}_q \right) \mathbf{x}_{\text{pl,OTFS}}}{|\boldsymbol{\Psi}_p \mathbf{x}_{\text{pl,OTFS}}|^2} \,. \tag{5.37}$$

Alg. 4 is used to obtain the estimation of Doppler, delay, and complex channel coefficient of each multipath component, i.e., the complete CSI, and it is described in the following. Note that, as for OFDM, if the number of multipath components P is not available at the receiver, we instead select all local maxima or peaks (of the groups of estimates) whose magnitude is above a certain threshold (to be defined).

Algorithm 4: *CSI Estimation*

```
Result: The set $(\hat{h}'_p, \hat{\tau}_p, \hat{\nu}_p)$, for $p = 0, \dots, P-1$.
Coarse Estimation: By analyzing on-grid Doppler and delay shifts, get
  the first coarse estimation of the pairs $(\hat{\tau}_p, \hat{\nu}_p)$ through the shifts of the
  peak pilot w.r.t. the Doppler-delay grid, by selecting the first $P$ local
  maxima;
It: Let $i = 0, 1, 2, \dots$ be the iteration number;
For $i = 1, 2, \dots$ do
    • Grid step and interval refinement: Refine the granularity of
      the step around the estimated values within a refinement interval.
      The finer the step size and the larger the interval, the greater the
      computational complexity;
    • Use the ML approach described in Alg. 1 to get a finer estimation
      of the unknown parameters;
    • Select the first $P$ local maxima.
End
```

The iterative process allows to refine the estimation through iterations, while keeping the computational cost limited and speeding-up the minimization of the estimation error. The definition of the refinement interval and grid step is not mandatory and depends on the signal processing capabilities of the system.

Note that, by considering the pilot scheme of Fig. 5.3 (and also the definition of $\mathbf{x}_{\mathrm{pl,OTFS}}$), the multiplication between the channel matrix $\boldsymbol{\Psi}_p$ and the pilot vector $\mathbf{x}_{\mathrm{pl,OTFS}}$ is just a column selection of matrix $\boldsymbol{\Psi}_p$, which significantly simplifies all the equations involved. We did not explicitly take advantage of this aspect, by keeping the treatment as general as possible, but note that the reduction in terms of computational complexity could be remarkable. In fact, under the pilot configuration depicted in Fig. 5.4, the aforementioned assumption does not hold. However, also in that case, it is possible to reduce the computational complexity, taking into account that only a limited number of non-zero elements constitute the pilot vector $\mathbf{x}_{\mathrm{pl,OTFS}}$. Once a pilot pattern has been defined or standardized, all these considerations are useful to improve the overall computational complexity, also by specifying ad hoc (hardware) signal processing.

5.4 Comparison in Terms of Pragramatic Capacity

Before proceeding further to numerical results, note that for both OFDM and OTFS, during the channel estimation process, a “peak selection” has to be performed. In a genie-aided scenario where the number of propagation paths P is a-priori known, this results in the search of the P local maxima of the objective, i.e., $\hat{\mathbf{h}}$. However, this information may not be available at the Rx and, in such a case, the algorithms should select all local maxima above a certain threshold (to be defined). By considering scattering components with decreasing power, which is generally the case, once the pathloss brings the power below the threshold, the corresponding component is neglected in the construction of the (estimated) channel matrix. Clearly, this results in a less accurate CSI, but, at the same time, the contribution of low- or very-low-energy paths has minor incidence in the estimated channel. In our simulation results we consider the genie-aided case where P is known, while the threshold-based analysis is a straightforward extension.

In this section, we characterize the performance in terms of pragmatic capacity, i.e., the mutual information between the constellation symbols transmitted and the soft-output estimates of the detector, for the case of separated detection and decoding [78, 79]. By considering a sequence of NM symbols $\{x_k\}$ belonging to any constellation $\mathcal{C}$ (for the sake of consistency, being NM the dimension of the transmitted block), let $\{\hat{x}_k\}$ be the noisy (soft) estimates of the transmitted symbol. The pragmatic capacity is simply defined as the symbol-by-symbol mutual information (see [79, 78, 46] for more details), which can be easily calculated by Monte Carlo simulations via the formula

$$I_{\mathrm{PC}} = \log_2 |\mathcal{C}| - \frac{1}{NM} \sum_{k \in \mathcal{D}} \sum_{x_k \in \mathcal{C}} P(x_k|\hat{x}_k) \log_2 \frac{1}{P(x_k|\hat{x}_k)} \,, \tag{5.38}$$

where $P(x_k|\hat{x}_k)$ is the *a posteriori* probability mass function of symbols $x_k \in \mathcal{C}$ given the detector soft-output $\hat{x}_k$, while $\mathcal{D}$ is the set of information symbols, i.e., excluding the pilots. Note that, since the numerator sums $|\mathcal{D}| \leq NM$ terms (being $|\cdot|$ the cardinality of the set), while the denominator takes into account the block size NM, the pilot overhead emerges naturally. An indication of the minimum length of the sequence to obtain reliable pragmatic capacity results is given in [103].

We adopt the LMMSE detector for both modulations, whose soft-output under non-perfect CSI, i.e., employing the estimated channel matrix $\hat{\mathbf{H}}$,[5] is given by

$$\hat{\mathbf{x}} = \hat{\mathbf{H}}^{\mathsf{H}} \left(\hat{\mathbf{H}} \hat{\mathbf{H}}^{\mathsf{H}} + \sigma^2 \mathbf{I} \right)^{-1} \mathbf{y} \,. \tag{5.39}$$

Note that for OFDM, whose (estimated) channel matrix is diagonal, the

---

[5] Note that, always for fairness, both modulations use the same estimation grid granularity.

LMMSE detector reduces to the symbol-by-symbol detection given by

$$\hat{x}_k = \frac{H^*_{k,k}}{\left|H_{k,k}\right|^2 + \sigma^2} y_k \,, \tag{5.40}$$

which significantly simplify the detection computational complexity of OFDM. On the other hand, in order to avoid the costly matrix inversion in (5.39) for OTFS modulation, different solutions have been proposed in literature [46, 62, 104, 47]. However, some of these approaches rely on non-realistic model or channel assumptions (e.g., Doppler shifts and delays integer multiples of the symbol grid) and therefore their performance degrades significantly when applied to realistic channel conditions, as shown in Chapter 4 ([46]). For this reason, beyond the very high complexity block-based LMMSE detector (5.39) for OTFS, we also consider the low-complexity MP soft-output algorithm proposed in [46] and analyzed in Chapter 4, which achieves linear complexity per block (i.e., constant complexity per symbol, comparable with the symbol-by-symbol MMSE detector for OFDM).

Note that the LMMSE detector is almost capacity achieving. For this reason, the gap between pragmatic capacity curves and AWGN capacity, taken as benchmark, at high SNR, where the estimation error is supposed to be small, is only due to the presence of the overhead of pilot symbols within the transmitted block. Asymptotically, the achievable rate loss ($\mathcal{R}^\ell$) is given by

$$\mathcal{R}^\ell = \frac{\mathcal{P}}{NM} \times 100 \; [\%] \,. \tag{5.41}$$

and the rate simply becomes the AWGN capacity multiplied by the fraction of data symbols per block, i.e., $\left|\mathcal{D}\right| / NM = 1 - \left|\mathcal{P}\right| / NM$. Moreover, as already said, in order to make a fair comparison, the overhead introduced by a CP for OFDM and by a generic GI (between blocks) for OTFS must be taken into account. While a GI interposed between two OTFS blocks, to avoid IBI, introduces a small-to-negligible overhead (especially when the dimension of the block increases), the CP overhead of OFDM is kept constant within the entire block (whatever its dimension), introducing a considerable loss in terms of pragmatic capacity. For instance, by considering a CP of length $T/4$, being T the symbol time, the loss is

$$\frac{T}{T+T/4} = \frac{T}{5T/4} = \frac{4}{5} = 0.8 = 20\% \,. \tag{5.42}$$

This means that, with a modulation of cardinality $\mathcal{C}$, while the maximum achievable rate is $\log_2 \mathcal{C}$ bits/symbol, OFDM saturates at $0.8{\cdot}\log_2 \mathcal{C}$ bits/symbol. The overall loss takes into account both the pilot overhead and the presence of a CP and/or GI (also of length $T/4$, for consistency).

Another important aspect is the definition of the number of pilots $|\mathcal{P}|$ w.r.t. the ambient dimension G. Many features are influenced by this choice. Consider first OFDM modulation. It is well known in the CS literature that the minimum number of pilots (or measurements, from CS literature) to recover a sparse signal is given by the logarithmic scaling factor [105]

$$|\mathcal{P}| \geq P \log \frac{G}{P} \,, \tag{5.43}$$

where P here represent the number of non-zero components of the vector to be estimated. Thus, given a multipath channel with P paths and a sensing matrix of dimension G (defined in (5.7)), the (asymptotically) minimum number of pilot symbols necessary to solve the minimization problem in (5.14) is given by (5.43). Due to the logarithmic scaling, the function is slowly increasing, even if the granularity of the sensing matrix and its dimension grows (see Section 5.2.1.1). However, while (5.43) provides a lower bound on the dimension, the optimal performance might be achieved for a number of pilots different from the minimum. For this reason, if the number of pilots used for a given setup (i.e., for fixed P and G) is well above the lower limit, we can state that while increasing the dimension G, the optimal number of pilots slightly changes. Hence, the pilot loss in (5.41) tends to zero, while increasing the ambient dimension G, which is directly linked to the block size NM (assuming, for simplicity, on-grid paths shifts and neglecting the refinement solution depicted in Alg. 3), and OFDM benefits from large blocks. Note that this is not a precise quantitative analysis but it just gives a qualitative idea or intuition on how large the number of pilots per block should be, knowing that the aforementioned CS-based conditions are always given up to constant factors that depend on the specific problem, SNR, shape of the sensing matrix, and other variables.

For OTFS modulation, the pilot scheme presented in Sec. 5.3.1 and its estimation algorithm are independent of the block dimension, since the shift of the peak pilot, and so the rough estimation, is only associated to the maximum Doppler and delay of the channel defined in (5.2). Hence, it follows that the pilot overhead tends to zero while increasing the block dimension, hence, as for OFDM, also OTFS benefits from large blocks. Moreover, if the dimension of the block increases, one can set more pilots to zero to raise the power of the peak pilot, allowing the detection of low power scattering components in the threshold-based approach (as explained at the beginning of Sec. 5.4). However, limits on the block dimension comes, first, from important restrictions on OTFS detection computational complexity (as seen in Chapter 4 and [46]), and then from the block fading assumption, which breaks down if the block becomes too large (see Chapter 1). Thus, realistic block sizes have to be considered in both directions.

Moreover, as anticipated in Sec. 5.2, in order to restrict to the classical low-complexity symbol-by-symbol MMSE estimation for OFDM we have neglected the ICI. As already seen in (5.29), the ICI depends on the ratio between the subcarrier spacing Δf and the maximum Doppler shift introduced by the channel. In order to have negligible ICI the necessary condition is $\Delta f \gg \nu_{\max}$, or, equivalently, $\nu_{\max}/\Delta f \ll 1$. Since $\Delta f = B/M$, with B total bandwidth, the condition may not be satisfied when the number of subcarriers M becomes too large, even for moderate Doppler. Here, we insist on neglecting ICI and consider the range of system parameters for which this assumption is indeed virtually exact. Furthermore, we notice that while OFDM incurs in this additional limitation, OTFS remains not sensitive to the Doppler shift.

Table 5.1: System parameters

$f_c = 5.89$ [GHz]	$M = 64$
$B = 10$ [MHz]	$N = 50$
$\Delta f = B/M = 156.25$ [kHz]	$T = 1/\Delta f = 6.4$ [μs]

5.4.1 Simulation Results

In the following figures, we plot the pragmatic capacity vs. SNR for OTFS and OFDM modulations with quadrature phase-shift keying (QPSK) modulated symbols, for a time-frequency multipath channel with P components affected by AWGN, and under non-perfect CSI. The channel estimation has been performed with the pilot schemes and the algorithms of Sec. 5.2 for OFDM and Sec. 5.3 for OTFS. As a reference benchmark, we plot the AWGN (symmetric) capacity $C_{\text{AWGN}}^{\text{sym}}$ for QPSK modulation, which results to be not achievable due to the pilot overhead. The system parameters are listed in Table 5.1.

Fig. 5.5 shows the performance of OFDM for a different number of pilot symbols. For the case $P = 1$, it easy to note that the performance slightly changes for different pilot overheads, whose percentage is indicated in the legend. On the other hand, as suggested by (5.43) and associated discussion, if the number of non-zero components to be estimated increases, i.e., with $P > 1$, the channel estimation algorithm needs more pilots to work efficiently. Given these results, from now on, we will consider a pilot overhead of 3.125%, achieving, in our setup, the best tradeoff between estimation accuracy and achievable pragmatic capacity (for any number of scattering components).

Fig. 5.6 shows the performance of OTFS with different detection algorithms. The MP soft-output detection approach of [46] is able to almost achieve the AWGN capacity under non-perfect CSI for a low number of scattering components, together with a remarkable reduction of the computational complexity [46]. However, in line with the results of [46] and Chapter 4, the detec-

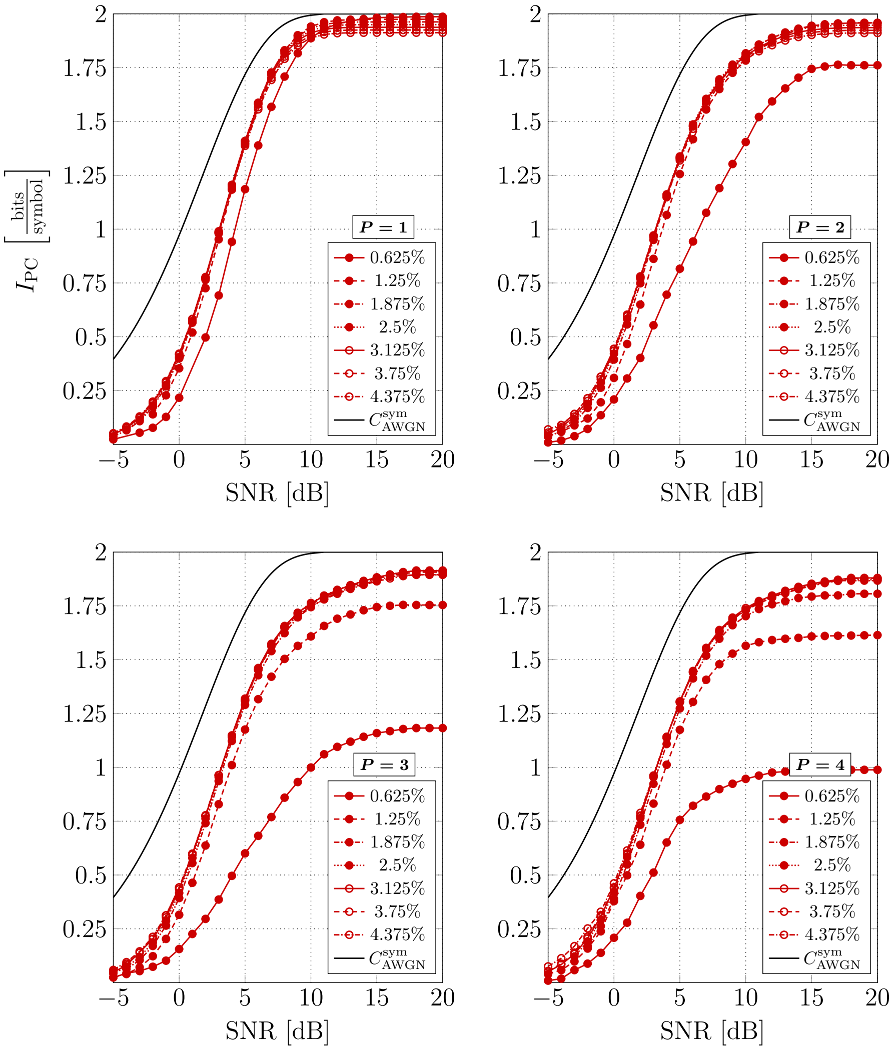

Figure 5.5: Pragmatic Capacity vs. SNR for OFDM modulation with multipath components P and different pilot overhead (whose percentage is indicated in the legend).

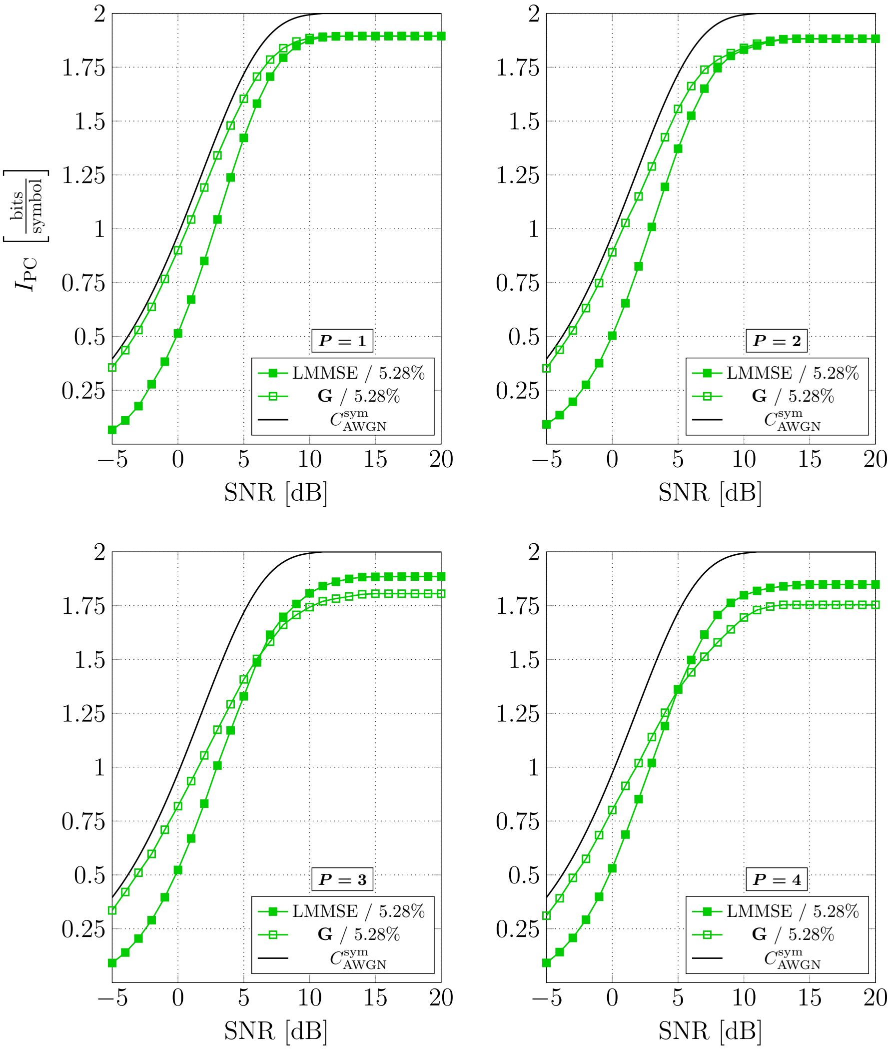

Figure 5.6: Pragmatic Capacity vs. SNR for OTFS modulation with multipath components P, different detection algorithms, i.e., LMMSE and MP approach of [46], for a fixed pilot overhead, in percentage 5.28%.

tor performance decreases with increasing multipath. Note that the small loss w.r.t. $C_{\mathrm{AWGN}}^{\mathrm{sym}}$ under non-perfect CSI is an indicator of the performance of the channel estimation algorithm, which results to be very accurate (otherwise the curve would have deviated from the benchmark). In light of these results, we see that there is no reason to adopt the LMMSE estimator for OTFS, which results in higher complexity and worse performance (see Chapter 4 and [46] for a more detailed analysis). Hence, from now on, for the comparison with OFDM modulation, we consider the MP "Matrix-**G**" approach of Chapter 4.

In Fig. 5.7, we plot the pragmatic capacity vs. SNR for OFDM and OTFS under the configurations mentioned above. First of all, it is possible to note that performance slightly decrease while increasing the number of multipath components, proving the robustness of the pilot schemes and the algorithms proposed. The pilot overhead has been chosen *ad hoc* for both modulations. For OTFS, as said in Sec. 5.3.1, the peak centered pilot collects all the energy of surrounding zero pilots, and the percentage of overhead (indicated in the figures) is also an indicator of the peak pilot energy. For OFDM, as pointed out before, the optimal tradeoff between estimation performance and pilot overhead has been found by brute-force search over a suitable set of possibilities (some of them are visible in Fig. 5.5). While the performance of the two modulations is similar, the presence of a *per symbol* CP for OFDM remarkably deteriorates the pragmatic capacity, while a *per block* GI for OTFS introduces a negligible loss.

In Fig. 5.8, we plot the pragmatic capacity of OFDM for a fixed value of SNR, i.e., 18 dB, while changing the ratio between the maximum Doppler shift and the subcarrier spacing, i.e., $\nu_{\max}/\Delta f$, taking into account a different number of subcarriers M ($N = 50$ for all cases). In this case, the received samples are obtained by considering a real channel taking into account the ICI, i.e., (5.29), while the channel estimation works under the hypothesis of an ideal interference-free channel. Intuitively, the performance degrades when the ICI becomes significant. Note that the estimation performance of the LASSO solver is independent of the number of subcarrier M and, for this reason,

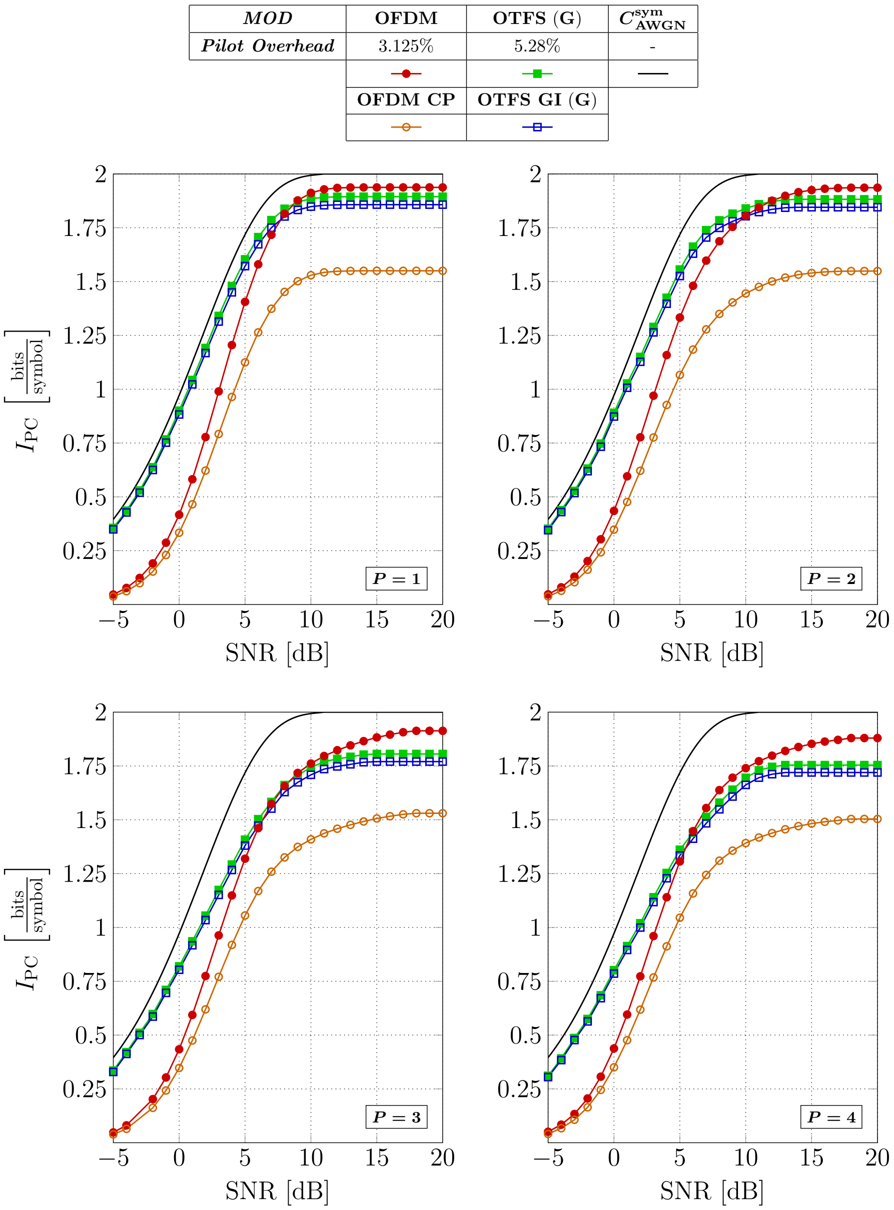

Figure 5.7: The curves take into account the loss related to the presence of pilots in the block of $N \times M$ symbols. The OFDM CP curve includes the CP overhead which is 0.25 of the symbol time, while the OTFS GI curve includes a GI for the entire block. A QPSK modulation is used. The legend indicates the percentage of pilot symbols.

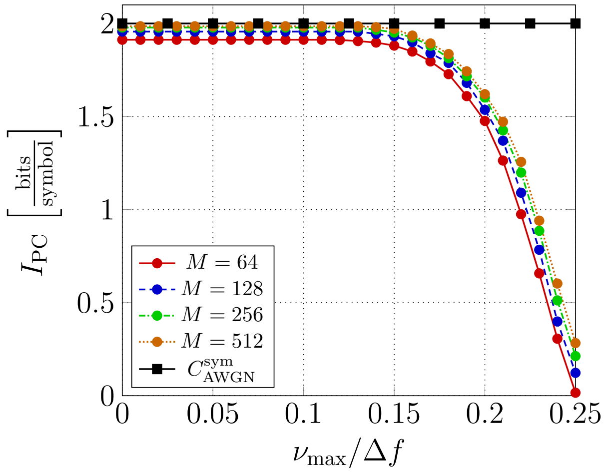

Figure 5.8: Pragmatic Capacity vs. $\nu_{\max}/\Delta f$ ratio for OFDM modulation with $P = 1$, at SNR = 18 dB.

whatever the choice of $\nu_{\max}$ and M, the performance of OFDM depends only on their ratio. Fig. 5.8 shows that the pragmatic capacity performance starts decreasing significantly for $\nu_{\max}/\Delta f \simeq 0.15$. Almost the same behavior is shown for different number of subcarriers M (not reported here for the sake of space limitation), except for the percentage of pilot loss due to different block dimensions, supporting what stated above. However, as pointed out in Table 5.2, while the performance is almost constant, the maximum tolerable Doppler (or velocity), inversely proportional to M, is not. For these reasons, as expected, OFDM is not independent of the block dimension and the system has to be defined properly to operate in the range where the ICI is negligible.

5.5 Conclusions

We carried out a fair comparison between OFDM and OTFS modulation formats in terms of maximum achievable rate for practical separated detection and decoding, quantified by the pragmatic capacity measured at the soft-

		$\nu_{\max}/\Delta f$		
		0.1	0.15	0.2
M	64	1431 [km/h]	2147 [km/h]	2863 [km/h]
	128	715 [km/h]	1073 [km/h]	1431 [km/h]
	256	357 [km/h]	536 [km/h]	715 [km/h]
	512	178 [km/h]	268 [km/h]	357 [km/h]

Table 5.2: Maximum supportable velocity w.r.t. the ratio $\nu_{\max}/\Delta f$ for OFDM modulation with subcarrier spacing $\Delta f = B/M$ and carrier frequency $f_c = 5.89$ GHz. The velocity is given by $v = c \cdot \nu_{\max}/\left(2f_c\right)$.

detector output.

We considered two pilot schemes and channel estimation algorithms each one specifically suited for the given modulation scheme. Both pilot and CSI estimation schemes are able to achieve very good performance (near genie-aided) under time-varying communication channel in the sparsity regime of a small number of number of multipath components. This conclusion is fully supported by numerical results, where simulation curves achieve the theoretical benchmark under non-perfect CSI, proving the quality of the proposed approaches.

OTFS achieves a better communication rate mainly because of the presence of a *per block* guard interval rather than a *per symbol* cyclic prefix as in OFDM. This of course comes at the cost of a more complex channel estimation scheme, working on large block-wise operations.

In terms of soft-output data detection, the use of the message passing soft-output detector of Chapter 4 yields constant per symbol complexity for OTFS, which is the same scaling law of symbol-by-symbol MMSE detection for OFDM. Although we do not claim that the complexity of the two detectors is identical, in fact the actual complexity differ for some implementation-based constant.

Finally, we can observe that OTFS is indeed very insensitive to the magnitude of the Doppler shifts, while the performance of OFDM degrades significantly even under small-to-moderate Doppler values if the number of subcarriers increases. Therefore, OTFS is effectively a good candidate for high-mobility systems in rural environments (e.g., high speed trains [106]) or aerial environments (e.g., UAVs [107]), where Doppler shifts may be large, and the propagation channel contains typically the line-of-sight and a few other reflection components (e.g., ground reflection, hills, large buildings), and it is therefore sparse in the Doppler-delay domain.

Conclusions

In this thesis, we studied multi-carrier modulation formats, in particular orthogonal frequency division multiplexing (OFDM) and orthogonal time frequency space modulation (OTFS), in some different communication scenarios exploiting the channel sparsity. In fact, by describing the communication channel in the Doppler-delay domain, the channel impulse response is directly linked to the physical representation of the surrounding environment, showing few and strong multipath components slowly changing in time.

Under this configuration, we explore the joint radar sensing and communication problem, which is of relevant interest in recent literature. In this context, first, we derive, analyze, and compare radar parameter estimation methods based on maximum likelihood functions, exploring the tradeoff between computational complexity and estimation performance. We thus prove that it is not necessary to implement radar and communication tasks with two different equipment, while a single full-duplex enabled radar system based on communication waveforms, such as OFDM or OTFS, is able to provide remarkable radar estimation performance, comparable to typical radar systems nowadays standardized for vehicular applications, while transmitting at its full achievable rate. Thus, the joint definition of the system avoids tradeoff coming from splitting the two functionalities, making this technology very promising for future applications. The aforementioned analysis has been carried out also taking into account the additional spatial dimension when multiple antenna systems are employed. Under these configurations, we extend the basic maximum likelihood algorithms to cope with multiple-input multiple-output systems, also over millimeter wave frequency bands, carrying on additional complications and limits.

Finally, in order to close the circle on the comparison between the two modulation formats, we have considered the channel estimation problem, treating all the related aspects, i.e., the pilot placement, the estimation algorithm (together with a complexity analysis), the overall loss (taking into account possible insertions of guard intervals within the transmitted signal), and the performance. We conclude that, by exploiting the channel sparsity, the performance, both in terms of overall achievable rate taking into account the pilot loss and in terms of computational complexity, of the two modulations is comparable and remarkable with respect to theoretical limits. However, the insertion of a *per symbol* cyclic prefix in OFDM, in order to prevent inter-symbol-interference and allows symbol-by-symbol detection, dramatically reduces the overall achievable rate, while a *per block* guard interval for OTFS has a small-to-negligible effect on communication performance.

The aim of the overall work is not to find or prove the optimality of one waveform against the other, as sometimes done in the current literature, but provides the baseline to properly define a multi-carrier system with the given constraints and target performance.

Acknowledgements

The work presented in this thesis is the outcome of the years of the Ph.D. course. It has been accomplished thanks to the help of several people I had the opportunity to collaborate with. First of all, my gratitude goes to my supervisors, Giuseppe Caire and Giulio Colavolpe, for their constant help and support. Then, I am thankful to Mari Kobayashi, for her patience and constant support, and to my past and present colleagues at the University, for the friendly environment and fruitful collaboration.

Two more technical supports. The work of Lorenzo Gaudio, Giuseppe Caire, and Giulio Colavolpe has been supported by Fondazione Cariparma, under the TeachInParma Project, and this research benefits from the HPC (High Performance Computing) facility of the University of Parma, Italy.

Bibliography

[1] J. G. Andrews, S. Buzzi, W. Choi, S. V. Hanly, A. Lozano, A. C. K. Soong, and J. C. Zhang. What will 5g be? *IEEE J. Sel. Areas Commun.*, 32(6):1065–1082, 2014.

[2] Richard van Nee and Ramjee Prasad. *OFDM for Wireless Multimedia Communications*. Artech House, Inc., USA, 1st edition, 2000.

[3] Andrea Goldsmith. *Wireless communications*. Cambridge university press, 2005.

[4] R. Hadani, S. Rakib, A. F. Molisch, C. Ibars, A. Monk, M. Tsatsanis, J. Delfeld, A. Goldsmith, and R. Calderbank. Orthogonal Time Frequency Space (OTFS) modulation for millimeter-wave communications systems. In *2017 IEEE MTT-S Int. Microw. Symp. (IMS)*, pages 681–683, June 2017.

[5] Ronny Hadani, Shlomo Rakib, Michail Tsatsanis, Anton Monk, Andrea J Goldsmith, Andreas F Molisch, and R Calderbank. Orthogonal time frequency space modulation. In *2017 IEEE Wireless Communications and Networking Conference (WCNC)*, pages 1–6. IEEE, 2017.

[6] K. R. Murali and A. Chockalingam. On OTFS modulation for high-doppler fading channels. In *2018 Information Theory and Applications Workshop (ITA)*, pages 1–10, Feb 2018.

[7] Giorgio A Vitetta, Desmond P Taylor, Giulio Colavolpe, Fabrizio Pancaldi, and Philippa A Martin. *Wireless communications: algorithmic techniques*. John Wiley & Sons, 2013.

[8] Kim Mahler, Wilhelm Keusgen, Fredrik Tufvesson, Thomas Zemen, and Giuseppe Caire. Measurement-based wideband analysis of dynamic multipath propagation in vehicular communication scenarios. *IEEE Trans. Veh. Technol.*, 66(6):4657–4667, 2016.

[9] Kim Mahler, Wilhelm Keusgen, Fredrik Tufvesson, Thomas Zemen, and Giuseppe Caire. Tracking of wideband multipath components in a vehicular communication scenario. *IEEE Trans. Veh. Technol.*, 66(1):15–25, 2016.

[10] Shanzhi Chen, Jinling Hu, Yan Shi, Ying Peng, Jiayi Fang, Rui Zhao, and Li Zhao. Vehicle-to-everything (V2X) services supported by LTE-based systems and 5G. *IEEE Communications Standards Magazine*, 1(2):70–76, 2017.

[11] Dingyou Ma, Nir Shlezinger, Tianyao Huang, Yimin Liu, and Yonina C Eldar. Joint radar-communications strategies for autonomous vehicles. *arXiv preprint arXiv:1909.01729*, 2019.

[12] Gor Hakobyan and Bin Yang. High-performance automotive radar: A review of signal processing algorithms and modulation schemes. *IEEE Signal Process. Mag.*, 36(5):32–44, 2019.

[13] Mark A Richards. *Fundamentals of radar signal processing, Second edition*. McGraw-Hill Education, 2014.

[14] Guillem Reus Muns, Kumar Vijay Mishra, Carlos Bocanegra Guerra, Yonnina C Eldar, and Kaushik R Chowdhury. Beam alignment and tracking for autonomous vehicular communication using IEEE 802.11 ad-based radar. *arXiv preprint arXiv:1712.02453*, 2017.

[15] E. Grossi, M. Lops, L. Venturino, and A. Zappone. Opportunistic radar in IEEE 802.11ad networks. *IEEE Trans. Signal Process.*, 66(9):2441–2454, May 2018.

[16] Emanuele Grossi, Marco Lops, and Luca Venturino. Adaptive detection and localization exploiting the IEEE 802.11 ad standard. *arXiv preprint arXiv:1904.12835*, 2019.

[17] P. Kumari, J. Choi, N. Gonzlez-Prelcic, and R. W. Heath. IEEE 802.11ad-based radar: An approach to joint vehicular communication-radar system. *IEEE Trans. Veh. Technol.*, 67(4):3012–3027, April 2018.

[18] X. Song, S. Haghighatshoar, and G. Caire. Efficient beam alignment for millimeter wave single-carrier systems with hybrid MIMO transceivers. *IEEE Trans. Wireless Commun.*, 18(3):1518–1533, March 2019.

[19] C. Sturm and W. Wiesbeck. Waveform design and signal processing aspects for fusion of wireless communications and radar sensing. *Proc. IEEE*, 99(7):1236–1259, July 2011.

[20] S. M. Patole, M. Torlak, D. Wang, and M. Ali. Automotive radars: A review of signal processing techniques. *IEEE Signal Process. Mag.*, 34(2):22–35, March 2017.

[21] D. H. N. Nguyen and R. W. Heath. Delay and doppler processing for multi-target detection with IEEE 802.11 OFDM signaling. In *Proc. IEEE Int. Conf. Acoustics, Speech, and Signal Processing (ICASSP)*, pages 3414–3418, March 2017.

[22] S Hossein Dokhanchi, MR Bhavani Shankar, M Alaee-Kerahroodi, T Stifter, and Björn Ottersten. Adaptive waveform design for automotive joint radar-communications system. In *Proc. IEEE Int. Conf. Acoustics, Speech, and Signal Processing (ICASSP)*, pages 4280–4284. IEEE, 2019.

[23] K. V. Mishra, M. R. Bhavani Shankar, V. Koivunen, B. Ottersten, and S. A. Vorobyov. Towards millimeter wave joint radar-communications: A signal processing perspective. *IEEE Signal Process. Mag.*, 36(5):100–114, Sep. 2019.

[24] Sayed Hossein Dokhanchi, Bhavani Shankar Mysore, Kumar Vijay Mishra, and Björn Ottersten. A mmWave automotive joint radar-communications system. *IEEE Trans. Aerosp. Electron. Syst.*, 55(3):1241–1260, June 2019.

[25] A. Hassanien, M. G. Amin, E. Aboutanios, and B. Himed. Dual-function radar communication systems: A solution to the spectrum congestion problem. *IEEE Signal Process. Mag.*, 36(5):115–126, Sep. 2019.

[26] Martin Braun. OFDM radar algorithms in mobile communication networks. *Ph.D. Thesis at Karlsruhe Institute of Technology*, 2014.

[27] Le Zheng, Marco Lops, Yonina C Eldar, and Xiaodong Wang. Radar and communication co-existence: an overview: a review of recent methods. *IEEE Signal Process. Mag.*, 36(5):85–99, Sep. 2019.

[28] Patchava Raviteja, Khoa T Phan, Yi Hong, and Emanuele Viterbo. Orthogonal time frequency space (OTFS) modulation based radar system. In *2019 IEEE Radar Conf. (RadarConf)*, pages 1–6. IEEE, 2019.

[29] L. Gaudio, M. Kobayashi, B. Bissinger, and G. Caire. Performance analysis of joint radar and communication using OFDM and OTFS. In *Proc. IEEE Int. Conf. Commun.*, pages 1–6, May 2019.

[30] M. Kobayashi, G. Caire, and G. Kramer. Joint state sensing and communication: Optimal tradeoff for a memoryless case. In *Proc. IEEE Int. Symp. Inf. Theory*, June, 2018.

[31] A. Sabharwal, P. Schniter, D. Guo, D. W. Bliss, S. Rangarajan, and R. Wichman. In-band full-duplex wireless: Challenges and opportunities. *IEEE J. Sel. Areas Commun.*, 32(9):1637–1652, Sep. 2014.

[32] M. Duarte and A. Sabharwal. Full-duplex wireless communications using off-the-shelf radios: Feasibility and first results. In *2010 Conference Record of the Forty Fourth Asilomar Conference on Signals, Systems and Computers*, pages 1558–1562, 2010.

[33] M Bică, V Koivunen, et al. Multicarrier radar-communications waveform design for RF convergence and coexistence. In *Proc. IEEE Int. Conf. Acoustics, Speech, and Signal Processing (ICASSP)*, 2019.

[34] David Tse and Pramod Viswanath. *Fundamentals of Wireless Communication.* Cambridge University Press, 2005.

[35] Ye Li. Pilot-symbol-aided channel estimation for OFDM in wireless systems. *IEEE Trans. Veh. Technol.*, 49(4):1207–1215, July 2000.

[36] Ji-Woong Choi and Yong-Hwan Lee. Optimum pilot pattern for channel estimation in OFDM systems. *IEEE Trans. Wireless Commun.*, 4(5):2083–2088, Sep. 2005.

[37] P. Raviteja, K. T. Phan, and Y. Hong. Embedded Pilot-Aided Channel Estimation for OTFS in Delay-Doppler Channels. *IEEE Trans. Veh. Technol.*, 68(5):4906–4917, May 2019.

[38] W. U. Bajwa, J. Haupt, A. M. Sayeed, and R. Nowak. Compressed Channel Sensing: A New Approach to Estimating Sparse Multipath Channels. *Proc. IEEE*, 98(6):1058–1076, June 2010.

[39] Xiaodong Wang and H. V. Poor. Iterative (turbo) soft interference cancellation and decoding for coded CDMA. *IEEE Trans. Commun.*, 47(7):1046–1061, July 1999.

[40] V. Rajan, A. A. Balakrishnan, and K. E. Nissar. OFDM Channel Estimation Using Compressed Sensing L1-Regularized Least Square Problem Solver. In *2013 Third International Conference on Advances in Computing and Communications*, pages 94–97, Aug 2013.

[41] G. Taubock, F. Hlawatsch, D. Eiwen, and H. Rauhut. Compressive Estimation of Doubly Selective Channels in Multicarrier Systems: Leakage Effects and Sparsity-Enhancing Processing. *IEEE J. Sel. Topics Signal Process.*, 4(2):255–271, April 2010.

[42] Chun-Jung Wu and D. W. Lin. A Group Matching Pursuit Algorithm for Sparse Channel Estimation for OFDM Transmission. In *2006 IEEE Int. Conf. on Acoust. Speech and Signal Process, Proc.*, volume 4, pages IV–IV, May 2006.

[43] Yongjun Liu, Guisheng Liao, Jingwei Xu, Zhiwei Yang, and Yuhong Zhang. Adaptive OFDM integrated radar and communications waveform design based on information theory. *IEEE Commun. Lett.*, 21(10):2174–2177, 2017.

[44] Wenqian Shen, Linglong Dai, Jian-ping An, Pingzhi Fan, and Robert W Heath. Channel Estimation for Orthogonal Time Frequency Space (OTFS) Massive MIMO. *IEEE Trans. Signal Process.*, 67(16):4204–4217, Aug 2019.

[45] M. Zhang, F. Wang, X. Yuan, and L. Chen. 2D structured turbo compressed sensing for channel estimation in OTFS systems. In *2018 IEEE International Conference on Communication Systems (ICCS)*, pages 45–49, Dec 2018.

[46] L. Gaudio, M. Kobayashi, G. Caire, and G. Colavolpe. On the effectiveness of OTFS for joint radar parameter estimation and communication. *IEEE Transactions on Wireless Communications*, 19(9):5951–5965, 2020.

[47] Junqiang Cheng, Hui Gao, Wenjun Xu, Zhisong Bie, and Yueming Lu. Low-Complexity Linear Equalizers for OTFS Exploiting Two-Dimensional Fast Fourier Transform. *arXiv preprint arXiv:1909.00524*, 2019.

[48] Li Li, Hua Wei, Yao Huang, Yao Yao, Weiwei Ling, Gong Chen, Peng Li, and Yunlong Cai. A simple two-stage equalizer with simplified orthogonal time frequency space modulation over rapidly time-varying channels. *arXiv preprint arXiv:1709.02505*, 2017.

[49] Jian Li and Petre Stoica. *MIMO radar signal processing*. John Wiley & Sons, 2008.

[50] Xiaoshen Song, Saeid Haghighatshoar, and Giuseppe Caire. A scalable and statistically robust beam alignment technique for millimeter-wave systems. *IEEE Trans. Wireless Commun.*, 17(7):4792–4805, 2018.

[51] Benjamin Friedlander. On transmit beamforming for MIMO radar. *IEEE Trans. Aerosp. Electron. Syst.*, 48(4):3376–3388, 2012.

[52] Urs Niesen and Jayakrishnan Unnikrishnan. Joint beamforming and association design for MIMO radar. *IEEE Trans. Signal Process.*, 67(14):3663–3675, 2019.

[53] S. Buzzi, C. DAndrea, and M. Lops. Using massive MIMO arrays for joint communication and sensing. In *2019 53rd Asilomar Conference on Signals, Systems, and Computers*, pages 5–9, 2019.

[54] S. Fortunati, L. Sanguinetti, F. Gini, M. S. Greco, and B. Himed. Massive MIMO radar for target detection. *IEEE Trans. Signal Process.*, 68:859–871, 2020.

[55] Xiaoshen Song, Thomas Kühne, and Giuseppe Caire. Fully-/partially-connected hybrid beamforming architectures for mmWave MU-MIMO. *IEEE Trans. Wireless Commun.*, 19(3):1754–1769, 2020.

[56] Zhimin Chen, Zhenxin Cao, Xinyi He, Yi Jin, Jingchao Li, and Peng Chen. DoA and DoD estimation and hybrid beamforming for radar-aided mmWave MIMO vehicular communication systems. *Electronics*, 7(3):40, 2018.

[57] Zhendao Wang and G. B. Giannakis. Wireless multicarrier communications. *IEEE Signal Process. Mag.*, 17(3):29–48, 2000.

[58] B. Saltzberg. Performance of an efficient parallel data transmission system. *IEEE Trans. Commun. Technol.*, 15(6):805–811, 1967.

[59] Carlos Cordeiro, Dmitry Akhmetov, and Minyoung Park. IEEE 802.11 ad: Introduction and performance evaluation of the first multi-gbps WiFi technology. In *Proceedings of the 2010 ACM international workshop on mmWave communications: from circuits to networks*, pages 3–8. ACM, 2010.

[60] Ralf Haas and Jean-Claude Belfiore. A time-frequency well-localized pulse for multiple carrier transmission. *Wireless personal communications*, 5(1):1–18, 1997.

[61] P. Raviteja, Y. Hong, E. Viterbo, and E. Biglieri. Practical Pulse-Shaping Waveforms for Reduced-Cyclic-Prefix OTFS. *IEEE Trans. Veh. Technol.*, 68(1):957–961, Jan 2019.

[62] P. Raviteja, K. T. Phan, Y. Hong, and E. Viterbo. Interference Cancellation and Iterative Detection for Orthogonal Time Frequency Space Modulation. *IEEE Trans. Wireless Commun.*, 17(10):6501–6515, Oct 2018.

[63] Daniel R Fuhrmann, Edward J Kelly, and Ramon Nitzberg. A CFAR adaptive matched filter detector. *IEEE Trans. Aerosp. Electron. Syst.*, 28(1):208–216, 1992.

[64] Fredrik Athley. *Space-time parameter estimation in radar array processing.* Department of Signals and Systems, School of Electrical Engineering, Chalmers University of Technology., 2003.

[65] F. Athley. Threshold region performance of maximum likelihood direction of arrival estimators. *IEEE Trans. Signal Process.*, 53(4):1359–1373, April 2005.

[66] J. Li and P. Stoica. MIMO radar with colocated antennas. *IEEE Signal Process. Mag.*, 24(5):106–114, Sep. 2007.

[67] Emre Telatar. Capacity of multi-antenna gaussian channels. *Europ J. Trans. Telecommun.*, 10(6):585–595, 1999.

[68] A Lee Swindlehurst, Ender Ayanoglu, Payam Heydari, and Filippo Capolino. Millimeter-wave massive MIMO: The next wireless revolution? *IEEE Commun. Mag.*, 52(9):56–62, 2014.

[69] Zhouyue Pi and Farooq Khan. An introduction to millimeter-wave mobile broadband systems. *IEEE Commun. Mag.*, 49(6):101–107, 2011.

[70] Yaakov Bar-Shalom and Xiao-Rong Li. *Multitarget-multisensor tracking: principles and techniques*, volume 19. YBs Storrs, CT, 1995.

[71] Lorenzo Gaudio, Mari Kobayashi, Giuseppe Caire, and Giulio Colavolpe. Joint radar target detection and parameter estimation with MIMO OTFS. *arXiv preprint arXiv:2004.11035*, 2020.

[72] M. Kollengode Ramachandran and A. Chockalingam. MIMO-OTFS in high-doppler fading channels: Signal detection and channel estimation. In *2018 IEEE Global Communications Conference (GLOBECOM)*, pages 206–212, 2018.

[73] Stuart M Wentworth. *Applied electromagnetics: early transmission lines approach.* John Wiley & Sons, 2007.

[74] Hiromu Suzuki. Measurement results of radar cross section of automobiles for millimeter wave band. In *Proceedings of the 7th World Congress on Intelligent Systems*, 2000.

[75] E. Bel Kamel, A. Peden, and P. Pajusco. RCS modeling and measurements for automotive radar applications in the W band. In *2017 11th European Conference on Antennas and Propagation (EUCAP)*, pages 2445–2449, 2017.

[76] Hubregt J Visser. *Array and phased array antenna basics*. John Wiley & Sons, 2006.

[77] G. Colavolpe, A. Barbieri, and G. Caire. Algorithms for iterative decoding in the presence of strong phase noise. *IEEE J. Sel. Areas Commun.*, 23(9):1748–1757, 2005.

[78] A. Kavcic, Xiao Ma, and M. Mitzenmacher. Binary intersymbol interference channels: Gallager codes, density evolution, and code performance bounds. *IEEE Trans. Inf. Theory*, 49(7):1636–1652, July 2003.

[79] J. B. Soriaga, H. D. Pfister, and P. H. Siegel. Determining and Approaching Achievable Rates of Binary Intersymbol Interference Channels Using Multistage Decoding. *IEEE Trans. Inf. Theory*, 53(4):1416–1429, April 2007.

[80] F. R. Kschischang, B. J. Frey, and H. . Loeliger. Factor graphs and the sum-product algorithm. *IEEE Trans. Inf. Theory*, 47(2):498–519, Feb 2001.

[81] G. Colavolpe, D. Fertonani, and A. Piemontese. SISO detection over linear channels with linear complexity in the number of interferers. *IEEE J. Sel. Topics Signal Process.*, 5(8):1475–1485, Dec 2011.

[82] L Sunil Chandran and CR Subramanian. Girth and treewidth. *Journal of combinatorial theory, Series B*, 93(1):23–32, 2005.

[83] T. J. Richardson and R. L. Urbanke. The capacity of low-density parity-check codes under message-passing decoding. *IEEE Trans. Inf. Theory*, 47(2):599–618, Feb 2001.

[84] G. Matz, H. Bolcskei, and F. Hlawatsch. Time-frequency foundations of communications: Concepts and tools. *IEEE Signal Process. Mag.*, 30(6):87–96, Nov 2013.

[85] J. Boutros and G. Caire. Iterative multiuser joint decoding: unified framework and asymptotic analysis. *IEEE Trans. Inf. Theory*, 48(7):1772–1793, July 2002.

[86] P. Raviteja, K. T. Phan, and Y. Hong. Embedded Pilot-Aided Channel Estimation for OTFS in DelayDoppler Channels. *IEEE Trans. Veh. Technol.*, 68(5):4906–4917, May 2019.

[87] A. Lancho, T. Koch, and G. Durisi. On single-antenna Rayleigh block-fading channels at finite blocklength. *IEEE Trans. Inf. Theory*, 66(1):496–519, 2020.

[88] A. Lancho, J. stman, G. Durisi, T. Koch, and G. Vazquez-Vilar. Saddlepoint approximations for noncoherent single-antenna rayleigh block-fading channels. In *Proc. IEEE Int. Symp. Inf. Theory*, pages 612–616, 2019.

[89] D. N. C. Tse, P. Viswanath, and Lizhong Zheng. Diversity-multiplexing tradeoff in multiple-access channels. *IEEE Trans. Inf. Theory*, 50(9):1859–1874, 2004.

[90] Lizhong Zheng and D. N. C. Tse. Diversity and multiplexing: a fundamental tradeoff in multiple-antenna channels. *IEEE Trans. Inf. Theory*, 49(5):1073–1096, 2003.

[91] M. Tuchler, R. Koetter, and A. C. Singer. Turbo equalization: principles and new results. *IEEE Trans. Commun.*, 50(5):754–767, 2002.

[92] Aik Chindapol and James A Ritcey. Design, analysis, and performance evaluation for BICM-ID with square QAM constellations in rayleigh fading channels. *IEEE J. Sel. Areas Commun.*, 19(5):944–957, 2001.

[93] V. Q. Rodriguez, F. Guillemin, A. Ferrieux, and L. Thomas. Cloud-RAN functional split for an efficient fronthaul network. In *2020 International*

Wireless Communications and Mobile Computing (IWCMC), pages 245–250, 2020.

[94] Wang Dongming, Han Bing, Zhao Junhui, Gao Xiqi, and You Xiaohu. Channel estimation algorithms for broadband MIMO-OFDM sparse channel. In *14th IEEE Proc. on Personal, Indoor and Mobile Radio Comm., 2003. PIMRC 2003.*, volume 2, pages 1929–1933 vol.2, Sep. 2003.

[95] Robert Tibshirani. Regression shrinkage and selection via the lasso. *Journal of the Royal Statistical Society: Series B (Methodological)*, 58(1):267–288, 1996.

[96] Amir Beck and Marc Teboulle. A fast iterative shrinkage-thresholding algorithm for linear inverse problems. *SIAM journal on imaging sciences*, 2(1):183–202, 2009.

[97] Yu Nesterov. Gradient methods for minimizing composite functions. *Mathematical Programming*, 140(1):125–161, 2013.

[98] Y. E. Nesterov. A method for solving the convex programming problem with convergence rate $O(1/k^2)$. *Dokl. Akad. Nauk SSSR*, 269:543–547, 1983.

[99] Mark Schmidt. Least squares optimization with L1-norm regularization. *CS542B Project Report*, 504:195–221, 2005.

[100] G. Wunder, S. Stefanatos, A. Flinth, I. Roth, and G. Caire. Low-Overhead Hierarchically-Sparse Channel Estimation for Multiuser Wideband Massive MIMO. *IEEE Trans. Wireless Commun.*, 18(4):2186–2199, April 2019.

[101] Emmanuel J Candes et al. The restricted isometry property and its implications for compressed sensing. *Comptes rendus mathematique*, 346(9-10):589–592, 2008.

[102] Pascal Koiran and Anastasios Zouzias. Hidden cliques and the certification of the restricted isometry property. *IEEE Trans. Inf. Theory*, 60(8):4999–5006, 2014.

[103] D. M. Arnold, H. . Loeliger, P. O. Vontobel, A. Kavcic, and W. Zeng. Simulation-Based Computation of Information Rates for Channels With Memory. *IEEE Trans. Inf. Theory*, 52(8):3498–3508, Aug 2006.

[104] Wenjun Xu, Tingting Zou, Hui Gao, Zhisong Bie, Zhiyong Feng, and Zhiguo Ding. Low-Complexity Linear Equalization for OTFS Systems with Rectangular Waveforms. *arXiv preprint arXiv:1911.08133*, 2019.

[105] Ben Adcock, Simone Brugiapaglia, and Matthew King-Roskamp. Do log factors matter? On optimal wavelet approximation and the foundations of compressed sensing. *arXiv preprint arXiv:1905.10028*, 2019.

[106] B. Ai, X. Cheng, T. Krner, Z. Zhong, K. Guan, R. He, L. Xiong, D. W. Matolak, D. G. Michelson, and C. Briso-Rodriguez. Challenges toward wireless communications for high-speed railway. *IEEE Intell. Transp. Syst. Mag.*, 15(5):2143–2158, 2014.

[107] E. Haas. Aeronautical channel modeling. *IEEE Trans. Veh. Technol.*, 51(2):254–264, 2002.